Contribution to Wind Energy Conversion Systems in Urban and Remote Areas

Ayman Al-Quraan

A Thesis

In the Department

of

Electrical and Computer Engineering

Presented in Partial Fulfillment of the Requirements

for the Degree of

Doctor of Philosophy (Electrical and Computer Engineering) at

Concordia University

Montreal, Quebec, Canada

© Ayman Al-Quraan,2016

CONCORDIA UNIVERSITY

SCHOOL OF GRADUATE STUDIES

This is to certify that the thesis prepared

By: Ayman Al-Quraan

Entitled: Contribution to Wind Energy Conversion Systems in Urban and Remote Areas.

and submitted in partial fulfillment of the requirements for the degree of

Doctor of Philosophy (Electrical and Computer Engineering)

complies with the regulations of the University and meets the accepted standards with respect to originality and quality.

Signed by the final examining committee:

_____ Chair

_____ External Examiner

Dr. A.Bakhshai

_____ External to Program

Dr. R. Zmeureanu

_____ Examiner

Dr. S. H. Zad

_____ Examiner

Dr. L. A. C. Lopes

_____ Thesis Supervisor

Dr. P. Pillay

_____ Thesis Co-Supervisor

Dr. Ted Stathopoulos

Approved by

_____

Dr. Wei-Ping Zhu, Graduate Program Director

August, 2016

_____

Dr. A. Asif, Dean

Faculty of Engineering and Computer Science

ACKNOWLEDGMENTS

I would like to express my deep appreciation to my supervisor Prof. Pragasen Pillay for his invaluable guidance and support throughout my Ph.D studies.

I am deeply grateful to my co-supervisor, Prof. Ted Stathopoulos for his detailed guidance and constructive advices.

Many thanks to all of my colleagues in the Power Electronics and Energy Research (PEER) group and the wind tunnel group – Mohammad Masadeh, Ahmad Malkawi, Khalid, Mohammad Hosein, Akram, Amir, Maged, Natheer, Oliver, lessedi, Abhijit Choudhury, John Wanjiku, Chirag, Mahmud Bijan, Andrew Jensson , Maher, Morteza, Jonathan, Nathan, Sudharshan, Rajendra, Sara, Jemimah , Hatem, Elsharawy and Mauricio- for their help and deep discussions.

I would like to express my deepest gratitude to my parents for their unconditional support throughout my entire life, to my beloved wife Roaa Aldalqamoni, for her emotional support and continuous encouragement, and to my children Abd Alrahman and Sara.

This research work was done as part of the NSERC/Hydro-Québec Industrial Research Chair entitled “Design and Performance of Special Electrical Machines”.

The author is also acknowledge the support by a scholarship from Yarmouk University, Jordan, as well as, the Faculty of Engineering and Computer Science of Concordia University in terms of the Graduate Student Support Program (GSSP).

ABSTRACT

Contribution to Wind Energy Conversion Systems in Urban and Remote Areas.

Ayman Al-Quraan, Ph.D.

Concordia University, 2016

Recently, there is a growing interest in the use of wind energy in buildings environment for distributed generation systems. However, the prediction of the wind speed and energy in such environment is difficult, due to the roughness and the frictional effects which reduce the wind speed close to the ground. Moreover, the adjacent buildings affect the wind regime around a specific building in the urban environment. Therefore, a method for appropriate estimating of the wind speed and energy over the buildings' roofs is required for the initial stages of the wind energy development in the urban environment.

This thesis provides a novel method of estimating the wind speed and energy using a wind tunnel. The method has been validated using two case studies, homogeneous and non-homogeneous terrain.

The Permanent Magnet Generator (PMG) is preferred in small Wind Energy Conversion System (WECS) for stand-alone and remote areas. A new technique to control the flux of the PMG for WECS applications has been developed and used in this thesis for voltage regulation purposes. By selecting a suitable value of d-axis current, the terminal voltage of the PM generator can be regulated for variable wind speed. Consequently, the terminal voltage across the load is also regulated. No special mechanical techniques or additional electromagnetic coils are used for this purpose.

The effect of the PMG flux control on the reactive power compensating capability for a variable inductive load has also been studied for WECS applications.

The case study presented in this thesis shows how the reactive power consumed by the load was compensated using the flux control operation of the system. The controller shows highly effective response during steady state and transient.

A flux controller of a permanent magnet variable flux machine (PM-VFM) has also been designed and presented in the thesis for voltage regulation purposes. The controller is designed based on injecting d-axis current pulses for short periods of time. These pulses have negligible losses which reduces the machine losses and increases the machine efficiency.

TABLE OF CONTENTS

LIST OF FIGURES

LIST OF TABLES

NOMENCLATURE

AC	Alternative Current.
CFD	Computational Fluid Dynamic.
DC	Direct Current.
HAWT	Horizontal Axis Wind Turbine.
HCC	Hysteresis Current Controller.
LPF	Low Pass Filter.
MPPT	Maximum Power Point Tracking.
TFI	Turbulent Flow Instrumentation.
PCC	Point of Common Coupling.
PMG	Permanent Magnet Generator.
PMSG	Permanent Magnet Synchronous Generator.
PMSM	Permanent Magnet Synchronous Motor.
UWE	Urban Wind Energy.
UWT	Urban Wind Turbines.
VAWT	Vertical Axis Wind Turbine.
WECS	Wind Energy Conversion System.
WT	Wind Turbine.

LIST OF SYMBOLS

A	Cross-sectional area of the wind.
B	Viscous coefficient.
c_1 - c_6	Coefficients dependent on the rotor type.
E_3	Wind energy above the roof of building X produced in T hours.
i_q, i_d	q and d axes current.
J	Moment of inertia.
L_q, L_d	q and d axes inductance of the machine.
N	Number of data included in the study.
p	Differential operator.
P_w	Wind power.
Q_L	Reactive power consumed by the load.
Q_{PMSG}	Reactive Power generated by the PMSG.
Q_r	Reactive Power generated by the active rectifier.
r	Stator resistor.
R	Rotor blade length.
T_L	Load torque.
v	Wind Speed (m/s).
v_1	Wind speed at Dorval airport.

v_2	Wind speed profile upstream the surroundings at the same level of the assumed anemometer over the roof.
$v_{2_{Eq}}$	Wind speed profile upstream the buildings at the same height of the installed anemometer over Equiterre building.
$v_{2.wT}$	Wind speed measured in the wind tunnel at the corresponding position in the upstream of the built model.
$v_{3.wT}$	Wind speed tested in the wind tunnel at the corresponding position over the roof of building X in the model.
V_{cut_in}	Cut-in speed of the wind turbine.
V_{cut_out}	Cut-out speed of the wind turbine.
V_G	Gradient wind speed.
V_{rated}	Rated speed of the wind turbine.
$\bar{x}$	Mean value of x_i.
x_i	Each value of the data.
Z_{EV}	Height of the installed anemometer above the roof of the EV building (measured from the ground).
Z_G	Gradient height.
$Z_{G\ O.T}$	Gradient height for open terrain.
$Z_{G\ Urb}$	Gradient height for urban area.
Z_X	Height of the installed anemometer over the building's roof.

α	Exponent factor.
$\alpha_{O.T}$	Exponent factor for open country terrain.
α_{Urb}	Exponent factor for urban terrain.
β	Blade pitch.
λ_{af}	PM flux linkage.
λ_q, λ_d	q and d axis flux linkage.
ρ	Air density (1.225kg/m^3).
σ	Standard deviation.
ω_s	Synchronous speed (rad/s).

CHAPTER 1: INTRODUCTION

1.1 Background

Renewable energy sources like wind, solar, hydro and tidal are used to generate electrical energy in an environmentally friendly at acceptable costs. These sources are being considered like as alternatives to the traditional energy sources such as oil, natural gas and coal. In recent years, distributed generation based on these renewable energy sources is of increasing interest to be used in the modern power systems. The reason is that the traditional sources cause environmental problems and subject to shortage in the near future. In addition, renewable energy resources are inexhaustible.

Among the renewable energy sources, wind energy is one of the most important and the fastest growing major sources of electricity around the world. The importance of wind energy comes from the immense potential in supplying electricity across the world. Generating electricity from small and distributed wind energy sources typically includes small wind turbines found at homes, farms, businesses and public facilities. There are significant differences between small wind turbines and the large ones. Large wind turbines, often grouped in wind farms, are widely used by utilities to provide electrical energy to electrical grids. While small wind turbines may look like miniature versions of large turbines, there are differences in technology, purchase decisions, application requirements and value of generated electricity.

Urban wind energy (UWE) is the energy based on using the small wind turbines in the urban environment. In the last few decades, there is a growing interest for using wind power in buildings using urban wind turbines (UWT). Wind turbine deployment in the built environment is inherently more complicated than in rural areas with open spaces.

In successfully exploiting wind energy in the built environment, three major issues can be identified: wind resource assessment and characterization of the wind around buildings, structural integration of wind turbines with buildings, and special urban wind turbine design requirements [1].

While the principles of wind turbines are simple, there are still big challenges regarding the best selection of the generator types and the machine performance. Several types of generators are used for wind applications. DC generators are not widely used in the WECS, because of the high maintenance requirement of brushes and commutator and the need of a full scale inverter in order to be connected to the AC grid. Usually, DC generators are restricted to non-grid-connected wind energy systems with small DC loads, i.e. battery chargers [2].

The induction generators require a source of reactive power. This leads to poor power factor of the machine. The power factor of smaller induction machines is lower in comparison to larger ones. The consumption of reactive power is penalized by many grid operators, since it causes losses in the grid. So the induction generator is not the best solution for the small WECS [3]-[5].

Use PMG are of the best solutions for grid connected WECS, especially for variable speed operation [6]-[7]. The reason is that the speed of the PMG can be controlled by power electronic devices for Maximum Power Point Tracking (MPPT) operation. Also, in the PMG there is no need for a DC excitation system. Moreover, by using the PMG the reactive power can be compensated easily when the load is changed by controlling the flux of the machine. This can be done by injecting a d-axis current ($+ve$ or $-ve$). Thus, the total air-gap flux of the machine can be enhanced or reduced.

1.2 Objectives

The objectives of this thesis are:

- Develop a method for estimating the urban wind power and energy over the roof of the buildings by means of wind tunnel experiments. This estimation can be used for selecting the best location of the urban wind turbines.
- Use a flux controller for a PMG based WECS for voltage regulation purposes at variable speed operation. Flux weakening operation of the controller is also used for speed range extension of the PMG.
- Investigate the effect of the flux controller of the PMG in the reactive power compensating capability for a variable inductive load.
- Provide a control strategy for a special PM machine (Variable Flux Machine (VFM)), which uses the AlNiCo PM as a low coercive PM for voltage regulation purposes. The control strategy is based on changing the magnet flux level by injecting d-axis current pulses to magnetize or demagnetize the magnet.

1.3 Thesis Outline

The prediction of the wind speed and energy in the urban environment is difficult, due to the adjacent buildings which affect the wind regime around a specific building in the urban environment. Moreover, the wind energy is a cubic function of the wind speed, so a small deviation in the estimation of the wind speed leads to large difference in the wind energy. This thesis provides a novel method for estimating the wind speed and energy using wind tunnel testing.

Since the wind speed is variable in the urban environment and the turbulence is always present, a method for regulating the voltage for a permanent magnet wind generator (PMG) for urban wind turbine applications is needed. This method is used to control the flux of a PM wind generator by selecting a suitable value of the d-axis current, so the terminal voltage of the PM generator can be regulated at variable wind speed. The controller and its implementation is discussed in chapter 3 in the thesis. In this controller, no special mechanical techniques or additional electromagnetic coils are used to achieve the purpose of this controller. However, such a controller will increase the losses of the machine and reduce the overall efficiency. A solution for this problem will be discussed in chapter 5 of the thesis.

Compensating the reactive power of the PMG is required in the urban environment, especially in the emergency cases when the electrical grid is shut down. A local source of reactive power, obtained from the compensating capability of the flux controller of the PMG, is useful for a case of electrical grid shut down. This issue is discussed in detail in chapter 4 in this thesis.

In order to overcome the problem of the controller of the conventional PMG which is discussed previously in Chapter 3, a new flux controller of a permanent magnet variable flux machine (PM-VFM) has also been designed and presented for voltage regulation purposes. The controller is designed based on injecting pulses of d-axis current for a short period of time. These pulses have negligible losses, and this improves the machine efficiency.

CHAPTER 2: URBAN WIND ENERGY MODELLING

2.1 Introduction

Urban energy generation such as that produced by small scale wind turbines installed on or around buildings can be defined as micro-generation. Recently, there is a growing interest in the use of wind energy in buildings for distributed generation. Since the generated power is a function of the cube of the wind speed, a small increase in the wind speed leads to a large difference in wind energy generation.

The prediction of the wind speed in the built environment is difficult, due to the roughness and the frictional effects which reduce the wind speed close to the ground. In addition, several adjacent buildings influence the wind regime around a specific building in the urban environment. The most dependable method for wind assessment in the urban environment is to directly measure the wind speed, ideally at the position and height of the proposed wind turbine. However, measuring the wind speed at a site is both time consuming and expensive, i.e. normally not appropriate for the early stages of wind energy development. Fortunately, several methods are available for the initial assessment of wind resource in urban areas, with varying degrees of resolution and accuracy. These are, in order of increasing accuracy, wind atlases, numerical methods including Computational Fluid Dynamics (CFD), wind tunnel modeling and direct wind resource measurement [8].

A wide range of wind atlases are available at the continental and national level. In Canada, the Canadian wind energy atlas - http://www.windatlas.ca - covers a wide area but its low resolution means that it can only give a general picture of the wind resource.

Another issue is that the wind atlases cannot take into account the local variations and their effect on the wind distribution.

On a more refined scale, wind speeds can be determined by using wind tunnel models, which must be combined with data at known locations. This role is usually fulfilled by local meteorological station measurements, other weather-related recorded data or airport data. The wind tunnel tests are used to give a more accurate estimate of wind without actually undertaking a wind measurement campaign.

The installation of a wind turbine in the built environment is only successful when there is enough wind resource. Therefore, the building under consideration needs to be free of surrounding obstacles and higher than directly adjacent buildings [9].

Many different types of roof wind turbines exist for the urban environment and they can be divided into two main groups depending on the orientation of their axis of rotation Horizontal Axis Wind Turbine (HAWT) and Vertical Axis Wind Turbine (VAWT). Several types of HAWTs and VAWTs are shown in Figs. 2.1 and 2.2 respectively.

This chapter is organized as follows: Section 2.2 discusses the literature review for the wind assessment in the built environment, section 2.3 refers to wind modeling, section 2.4 describes the wind tunnel facility and the instrumentation used in the measurements of this study, section 2.5 describes the methodology used in the estimation of the wind energy and in sections 2.6 and 2.7 this methodology has been tested using homogeneous and nonhomogeneous case studies prior to concluding the results in section 2.8.

(a)

(b)

Fig. 2. 1: Different Types of HAWTs. (a) Three Wind Turbines Installed over Strata Tower which is a 43-Story Building in London [10]. (b) Four small scale wind turbines in the Indigo Building in Portland's West, Washington [11].

(a)

(b)

Fig. 2. 2: Different Types of VAWTs. (a) Wind Farm installed on Roof of Oklahoma Medical Research Foundation, Consists of 18 VAWT [12]. (b) Four VAWTs in Marine Board Building in Hobart in Australia [13].

2.2 Literature Review for the Wind Assessment in the Built Environment

The wind assessment in the built environment is difficult, due to the roughness and the frictional effects which reduce the wind speed close to the ground. In addition, several adjacent buildings influence the wind regime around a specific building in the urban environment. In the literature, several methods are used to assess the wind energy in the urban area [8] i.e. field measurements, wind atlases, wind tunnel testing and numerical computation using CFD. Due to the difficulties in the first two methods, wind tunnel testing and computational methods are preferred, especially in the initial stages for the urban wind power development project.

Cheng in [14] used the UC Davis Atmospheric Boundary Layer Wind Tunnel to study the variation in local wind conditions over a region of the Altamont Pass, California, containing two wind farms. Meteorological data combined with wind tunnel results were used to predict the power output of the wind farms every half hour over a one year period from July 2001 to June 2002. It was observed that the power production of the wind farms could be predicted with 20% error.

The study in [15] used to measure the detailed wind speed distribution in front of a Concordia building wall by means of wind tunnel experiments. The aerodynamics laboratory at Concordia University, Montreal, was used in this study. The reason for the wind tunnel test is to study the thermal efficiency of the roof solar collectors and their performance influence by the wind direction.

Moreover, the wind tunnel is used in testing small wind turbines to generate the power curve according to some international standards such as the IEC 61400 [16].

The CFD methods have also a potential to be used in the wind energy resource assessment in complex urban terrains by modeling wind circulation around urban obstacles. Several research works have been done to estimate the wind energy using the CFD numerical methods:

In [17], the CFD simulation was used to evaluate the wind energy potential on the campus of the Massachusetts Institute of Technology in Cambridge, MA. The assessment was enhanced by integration of local wind measurements and observations from several nearby reference sites. Data from two meteorological wind stations were included in the wind energy analysis. Comparisons between the field measurements and the simulated results show a correlation of 70% between both of them.

CFD is also used in the prediction of the extracted wind energy from urban wind turbines [18]. This prediction is based on simulating urban areas with urban wind turbines. However, such a complicated numerical computer based method has limitation especially regarding the turbulence.

2.3 Wind Modelling

For winds near the ground surface, frictional effects play a significant role. Ground obstructions retard the movement of air close to the ground surface, causing a reduction in wind speed. At some height above ground, the movement of air is no longer affected by ground obstruction. This height is called gradient height Z_G which is a function of ground roughness. The unobstructed wind speed is called gradient wind speed, V_{ZG} and it is considered to be constant above gradient height. The power law, which is used by some engineers to represent the variation of wind speed with height, is an empirical equation, which for the case of mean speeds takes the form of:

$$\frac{V_Z}{V_{Z_G}} = \left(\frac{Z}{Z_G}\right)^{\alpha} \tag{2.1}$$

where:

Z_G Gradient height

α Exponent factor

Both are functions of the ground roughness. Typical values of Z_G and α are given in Table 2.1. Fig. 2.3 shows typical variations of wind speeds above different ground roughness.

Table 2. 1: Suggested Values of Z_G and α for Various Terrain Conditions [19].

Terrain Description	**Gradient height, $Z_G(m)$**	**Mean speed exponent (α)**
Large City centers, in which at least 50% of buildings are higher than 21 m.	460	0.33
Suburban, wooded areas, and other areas with closely spaced obstructions compared to or larger than single-family dwellings	370	0.22
Open terrain with scattered obstacles generally less than 10 m height.	300	0.15
Flat, Unobstructed areas exposed to wind flowing over a large water body.	210	0.1

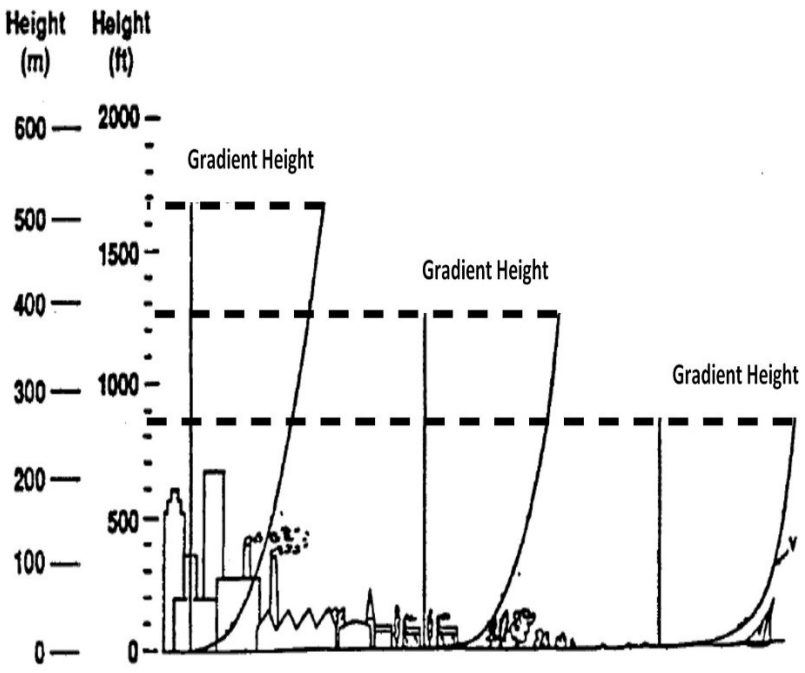

Fig. 2. 3: Variation of Wind Speed with Height [20].

2.4 Wind Tunnel Facility

Wind tunnels have been a key element in scientific research in a number of fields. Since the 19th century, experimenting with race cars, airplanes, weather patterns, and various other areas has been made much easier because of this development. Moreover, wind tunnels have a variety of important uses in the world today including the design of buildings [21]. A photo of an atmospheric boundary layer wind tunnel is shown in Fig. 2.4.

Fig. 2. 4: Wind Tunnel Facility at Concordia University.

2.4.1 Boundary Layer Wind Tunnel

The boundary layer wind tunnel of Concordia University, is 12.2 m in length and 1.8 m in width with a suspended roof that allows the height to be adjusted between 1.4 m and 1.8 m. The wind tunnel can be operated at velocities from 3 m/sec to 14 m/sec. A turntable, 1.6 m diameter, at the test section allows the model to be rotated to account for different wind directions. Fig. 2.5 shows a complete schematic of the wind tunnel and construction details [20]-[22].

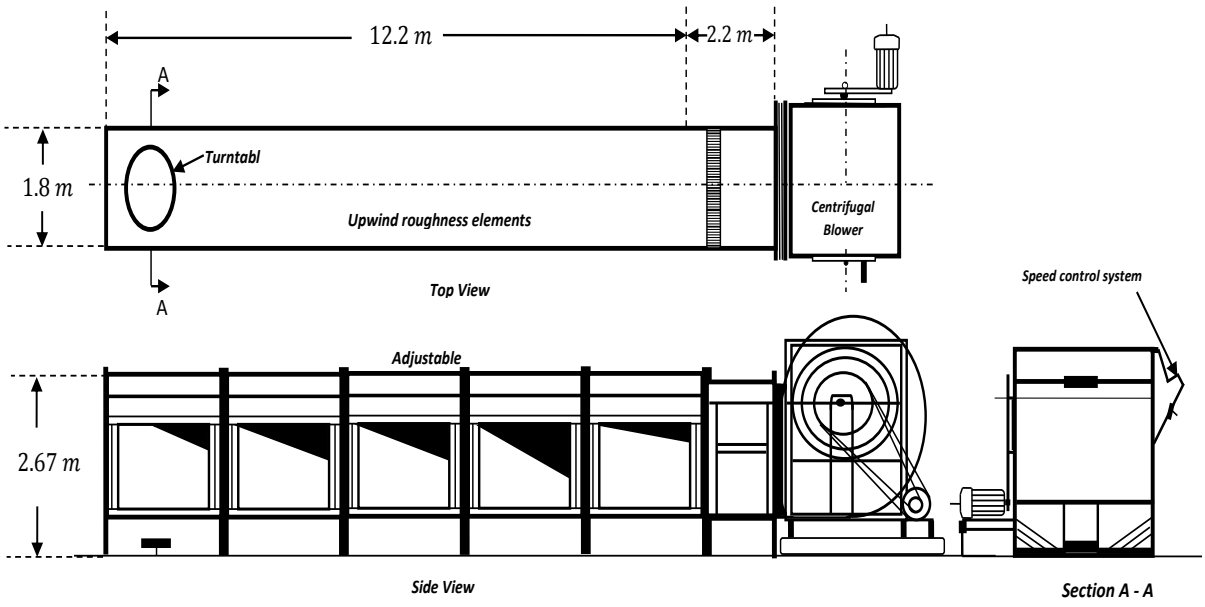

Fig. 2. 5: Complete Schematic of the Wind Tunnel and Construction Details [22].

2.4.2 Cobra Probe and 3-Dimensional Traversing System

The 4-hole Cobra probe, from Turbulent Flow Instrumentation (TFI), is a flow measurement device that measures static-pressure and velocity and resolves the velocity components in real-time. It is about 16 cm in length and 1.4 cm in diameter, with a 5 cm long stem and 0.5 cm long head as shown in Fig. 2.6 [21].

A graphical user interface and data acquisition software of the instrument enable the control of the measurement process and display of the data on a computer screen in real time.

The software stores this data in text files that can easily be imported into a spreadsheet. A three-dimensional traverse system attached to the wind tunnel ceiling above the test section enables accurate positioning of velocity measurement devices at points of interest on the model.

During the wind tunnel tests, the Cobra probe is mounted onto the 3-D traversing arm and positioned on the model using a control system whereby Cartesian co-ordinates of the point of interest are entered.

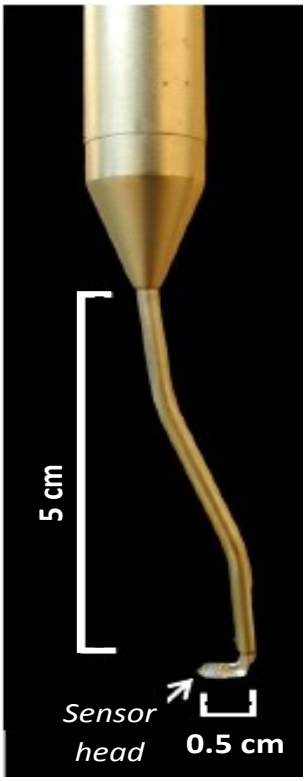

Fig. 2. 6: Cobra Probe for Wind Speed Measurements [21].

2.5 Methodology Used to Estimate the Wind Power and Energy over the Roof of the Buildings

Consider a case of wind energy estimation such as the situation in Fig. 2.7. The wind speed is measured in meteorological stations or at airports usually at 10m height from the ground level. In this case the wind speed is measured at Montreal's Dorval (PET) Airport and denoted by v_1.

The target is to estimate the wind velocity over a specific position at the roof of building X denoted by v_3, as shown in Fig. 2.7. At Dorval (PET) Airport in Montreal, the 10's degree convention is used to determine the direction of the wind speed in which 9 means 90 degrees true or an east wind, and 36 means 360 degrees true or a wind blowing from the north. A value of zero denotes a calm wind. Fig. 2.8 shows a schematic representation of the 10's Degree convention of wind direction in Dorval (PET) Airport in Montreal.

In Montreal the prevailing wind direction is the south-west (SW) which is clearly shown in Montreal wind rose in Fig. 2.9 where the wind direction distribution is presented in %. According to 10's degree convention SW is a number between (18 to 27). In order to obtain the best estimation of wind energy, all the wind directions from the south west will be considered in the estimation i.e. numbers from 18 to 27, and every two steps from other directions i.e. numbers 1, 3, 5, …, 15 and 18 to 27, then 29, 31, 33, 35 [23][24].

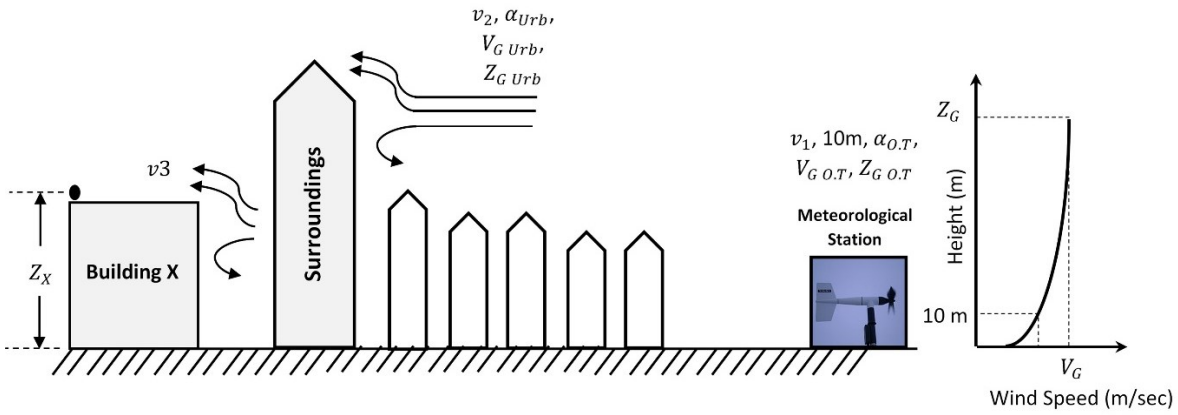

Fig. 2. 7: Schematic for Wind Energy Estimation.

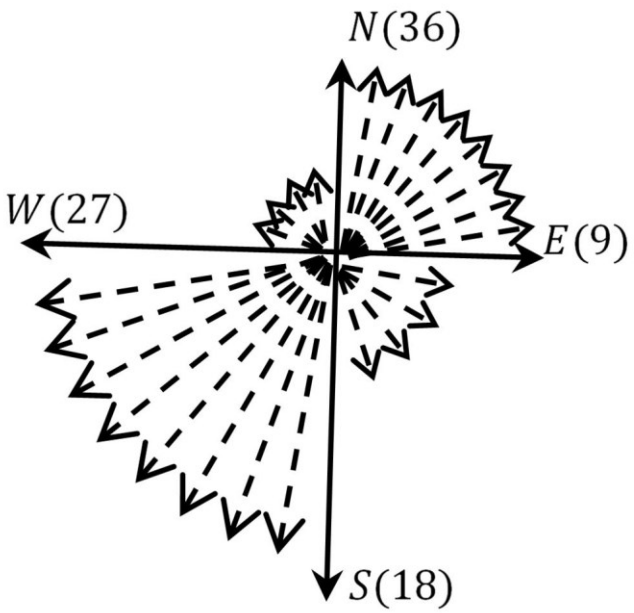

Fig. 2. 8: Schematic Representation of the 10's Degree Convention of Wind Direction in Dorval (PET) Airport in Montreal.

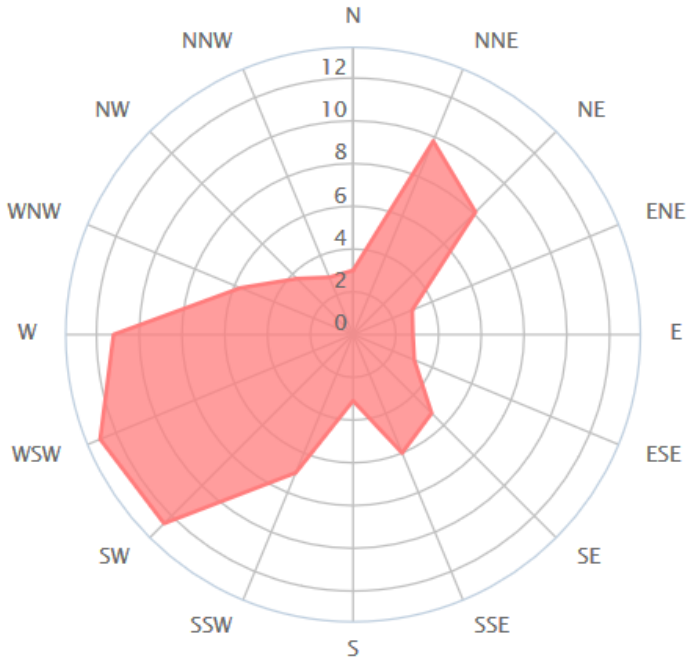

Fig. 2. 9: Yearly Wind Rose of Montreal (Wind Direction Distribution in %) [25].

The wind speed at Dorval airport can be estimated as follows:

$$\frac{v_1}{V_G} = \left(\frac{10}{Z_{G\,O.T}}\right)^{\alpha_{O.T}} \tag{2.2}$$

Where:

v_1 The wind speed at Dorval airport.

V_G The gradient wind speed.

$Z_{G\,O.T}$ The gradient height for open terrain.

$\alpha_{O.T}$ The exponent factor for open terrain.

The wind speed upstream the surroundings (v_2) can be estimated by considering urban upstream roughness as follows:

$$\frac{v_2}{V_G} = \left(\frac{Z_X}{Z_{G\,Urb}}\right)^{\alpha_{urb}} \tag{2.3}$$

Where:

v_2 The wind speed profile upstream the surroundings at the same level of the assumed anemometer over the roof.

$Z_{G\,Urb}$ The gradient height for urban area.

Z_X The height of the installed anemometer over the building's roof.

α_{Urb} The exponent factor for urban terrain.

By dividing (2.3) / (2.2), the relation between (v_2) and (v_1) can be obtained as follows:

$$\frac{v_2}{v_1} = \frac{\left(\frac{Z_X}{Z_{G\,Urb}}\right)^{\alpha_{Urb}}}{\left(\frac{10}{Z_{G\,O.T}}\right)^{\alpha_{O.T}}} \Longrightarrow v_2 = v_1 \times \frac{\left(\frac{Z_X}{Z_{G\,Urb}}\right)^{\alpha_{Urb}}}{\left(\frac{10}{Z_{G\,O.T}}\right)^{\alpha_{O.T}}} = v_1 \times Correction\ Factor \tag{2.4}$$

The wind speed at a specific position on top of the building roof can be calculated as follows:

$$v_3 = Ratio \times v_2 \tag{2.5}$$

Where this ratio can be obtained using wind tunnel tests as follows:

$$Ratio = \frac{v_{3.wT}}{v_{2.wT}} \tag{2.6}$$

and:

$v_{3.wT}$ The wind speed tested in the wind tunnel at specific position over the roof of building X in the model.

$v_{2.wT}$ The wind speed measured in the wind tunnel at the corresponding position in the upstream of the built model.

In order to find these ratios, physical models for building X and the surroundings have to be built and tested in the wind tunnel as shown in Fig. 2.10.

Using this methodology, a complete wind speed profile at a specific position over the roof can be obtained to be used in the wind energy estimation as follows:

$$E_3 = \frac{1}{2}\rho v_3^3 T \tag{2.7}$$

Where:

E_3 Wind energy above the roof of building X produced in T hours.

In order to study the variation of the data form the average value, the standard deviation (σ) has been used to implement this effect as follows:

$$\sigma = \sqrt{\frac{1}{N}\sum_{i=1}^{N}(x_i - \bar{x})^2} \tag{2.8}$$

Where:

σ Standard deviation.

N Number of data included in the study.

x_i Each value of the data.

$\bar{x}$ Mean value of x_i.

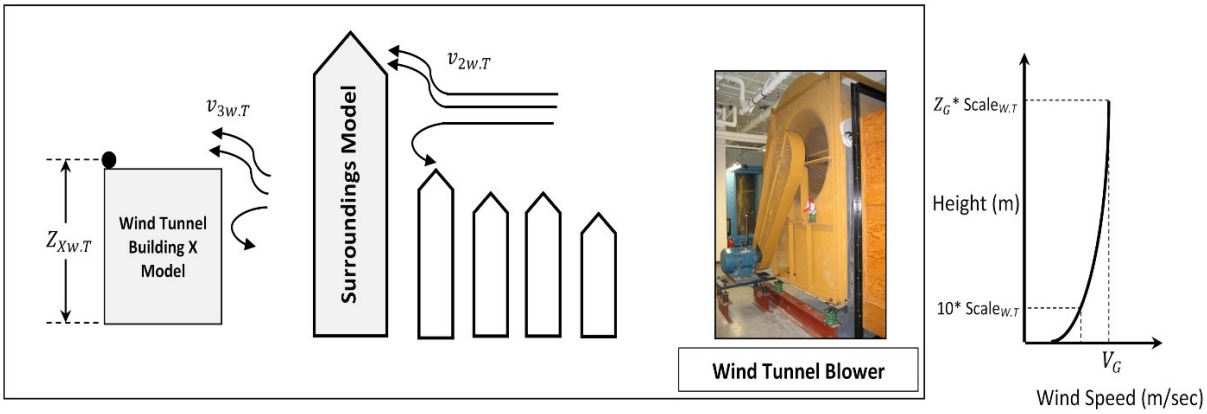

Fig. 2. 10: Wind Tunnel Test of Wind Energy Estimation.

2.6 Testing the Methodology Using a Homogeneous Terrain

In order to test this methodology, two cases with different terrains, non-homogeneous and homogeneous terrain, have been applied in Montreal as follows:

- EV building case (homogeneous terrain).
- Equiterre building case (non-homogeneous terrain).

A case study of wind energy estimation using the wind tunnel has been applied to the EV building which is the engineering complex of Concordia University. The height of the EV building is around 76 m. Fig. 2.11 shows the top view of the EV building and the surrounding areas.

To compare the calculated wind energy using the field measurements over the EV building roof and the estimated value using the proposed methodology, a three-cup anemometer was installed in one corner above the roof. The anemometer was programed to take one measurement every 5 seconds. The field measurements were collected from the beginning of August 2013 to the end of October 2013. Fig. 2.12 shows the installed three-cup anemometer at 2m height over the EV building roof. The obtained data was used to calculate the total wind energy for the corresponding period. Figs 2.13 and 2.14 show the monthly average wind speed above the roof of the EV building and the calculated total wind energy respectively using the field measurement data. The corresponding error bars is also shown in Figs 2.13 and 2.14.

Fig. 2. 11: EV Building and the Surrounding Area [27].

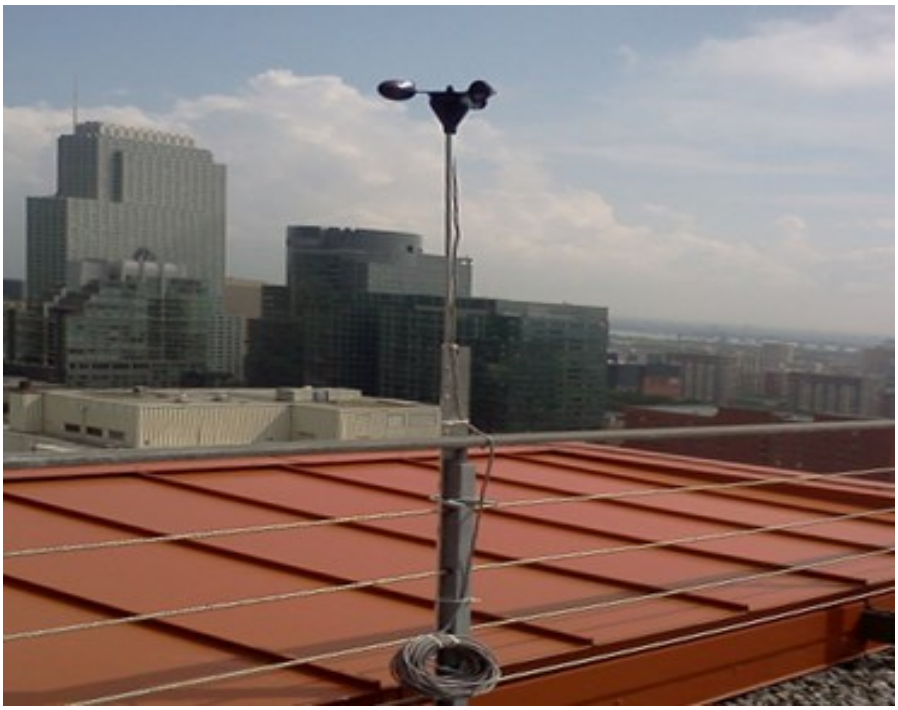

Fig. 2. 12: Installed Anemometer above the Roof of the EV Building.

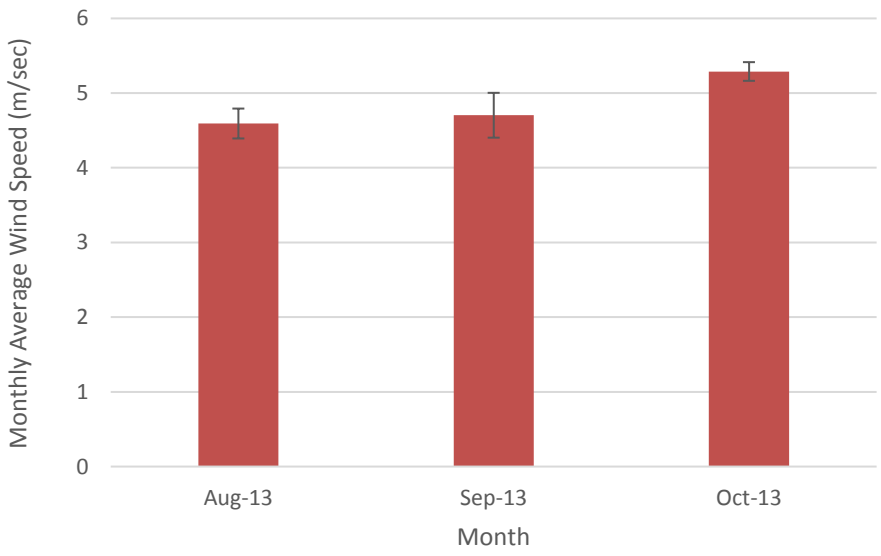

Fig. 2. 13: Average Wind Speed of the Field Measurement Data above the Roof of EV Building and the Corresponding Error Bars.

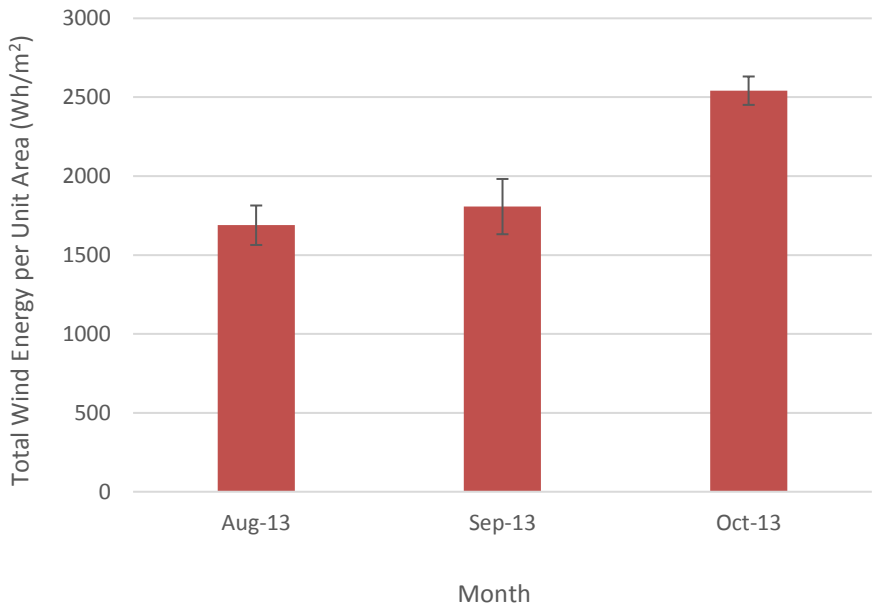

Fig. 2. 14: Calculated Total Wind Energy of the Field Measurement Data above the Roof of EV Building and the Corresponding Error Bars.

One year of wind speed data was obtained from Dorval (PET) Airport sensor from the beginning of November 2012 to the end of October 2013 for use in the energy estimation above the roof of the EV building. The wind tunnel tests in this case were carried out using the model of the EV building available in the wind tunnel laboratory of Concordia University. Fig. 2.15 shows the EV building model and the surrounding area. Using Eq. 2.4 and by considering an exponent factor (α) of 0.22 which is applicable in this case, a correction factor was used to estimate the wind speed in the upstream of the roof of the EV building at the same height of the installed anemometer. This correction factor is calculated as follows:

$$Correction\ Factor = \frac{[Z_{EV}/Z_{G\ S.Urb}]^{\alpha_{S.Urb}}}{[10/Z_{G\ O.T}]^{\alpha_{O.T}}} = \frac{[78/370]^{0.22}}{[10/300]^{0.15}} = 1.18 \quad (2.9)$$

The wind speed upstream the EV building ($v_{2_{EV}}$) is calculated as follows:

$$v_{2_{EV}} = Correction\ Factor * v_1 = 1.18 * v_1 \quad (2.10)$$

Where:

Z_{EV} Height of the installed anemometer above the roof of the EV building (measured from the ground).

Fig. 2. 15: EV Building Model with the Surroundings under the Test in the Wind Tunnel (Direction of the Wind is South-West).

The ratios of the upstream wind speed to the wind speed above the roof of the EV building from different directions were measured using the wind tunnel tests. These ratios - shown in Table 2.2 - were included in the estimation of the wind speed at the same position of the anemometer by using Eq. 2.5 to obtain a complete hourly wind speed profile for the duration of one year.

Then the hourly wind speeds were averaged for each month to be used in energy estimation. Comparisons between the field measurements wind speed and energy and their estimations are shown in Figs. 2.16 and 2.17 respectively. It can be shown that the error in the wind energy, evaluated by [(error = field – estimated)/field]*100%, is less than 5% as shown in Table 2.3. This means that this methodology is accurate enough to be used, at least in the case of homogeneous terrain. Using the estimated wind speed profile for a duration of one year, the wind energy were evaluated for the corresponding period using Eq. 2.7. Figs 2.18 and 2.19 show the estimated wind speed and wind energy above the roof of the EV building.

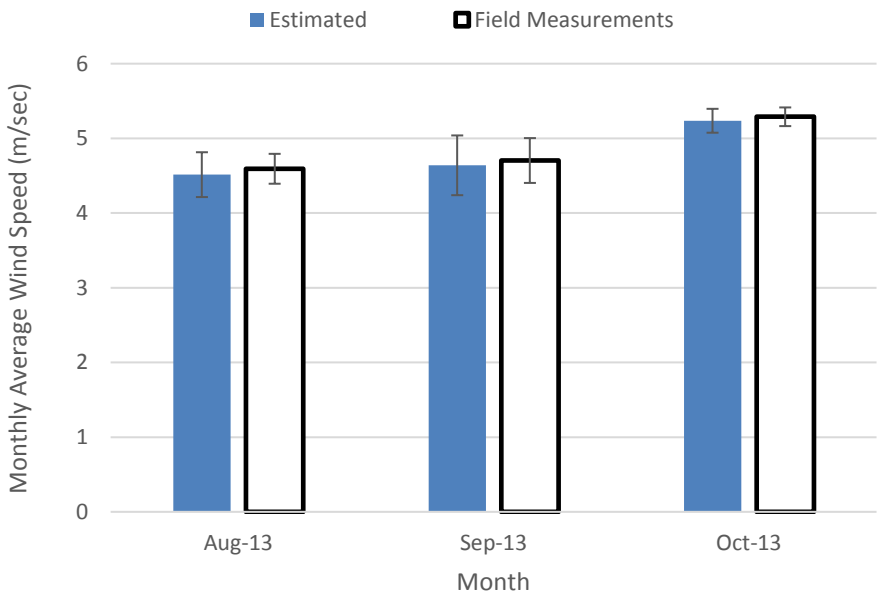

Fig. 2. 16: Field Measurement Data and the Estimated Values above the Roof of EV Building with the Corresponding Error Bars.

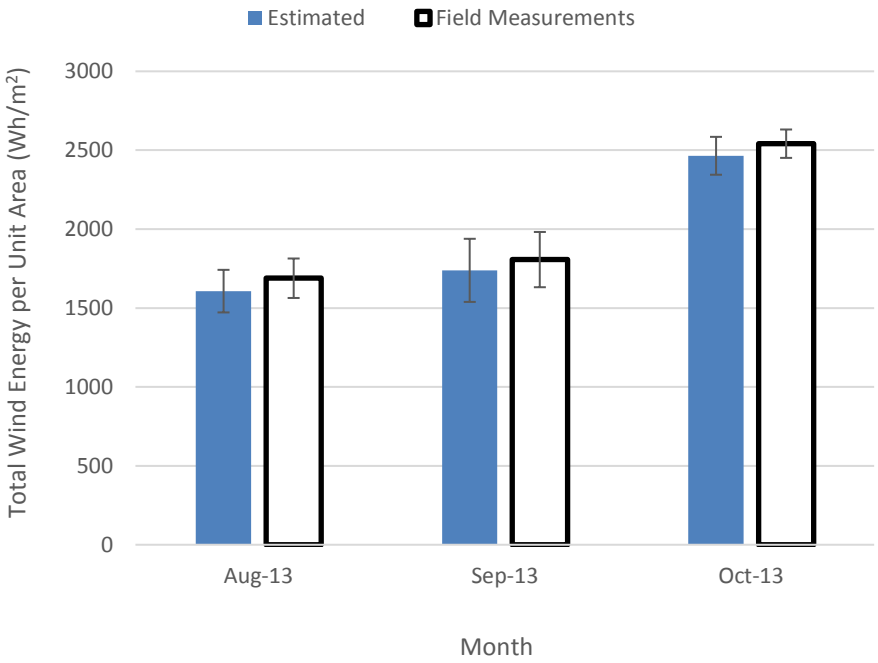

Fig. 2. 17: Field Measurement Data and the Estimated Values above the Roof of EV Building with the Corresponding Error Bars.

Table 2. 2: Wind Directions under the Wind Tunnel Tests and their Corresponding Ratios for the EV Building (Eq. 2.6).

Direction	Ratio	Direction	Ratio
1	0.98	20	1.06
3	0.95	21	0.99
5	0.98	22	0.94
7	1.07	23	0.91
9	1.10	24	1.01
11	1.13	25	1.06
13	0.93	26	1.17
15	1.06	27	1.02
17	0.96	29	1.09
18	1.11	31	0.98
19	1.02	33	0.93

Table 2. 3: The Error between the Field Measurements and the Estimation of the Wind Energy at the Roof of EV Building.

Month	Error (%)
August 2013	4.8
September 2013	3.8
October 2013	3

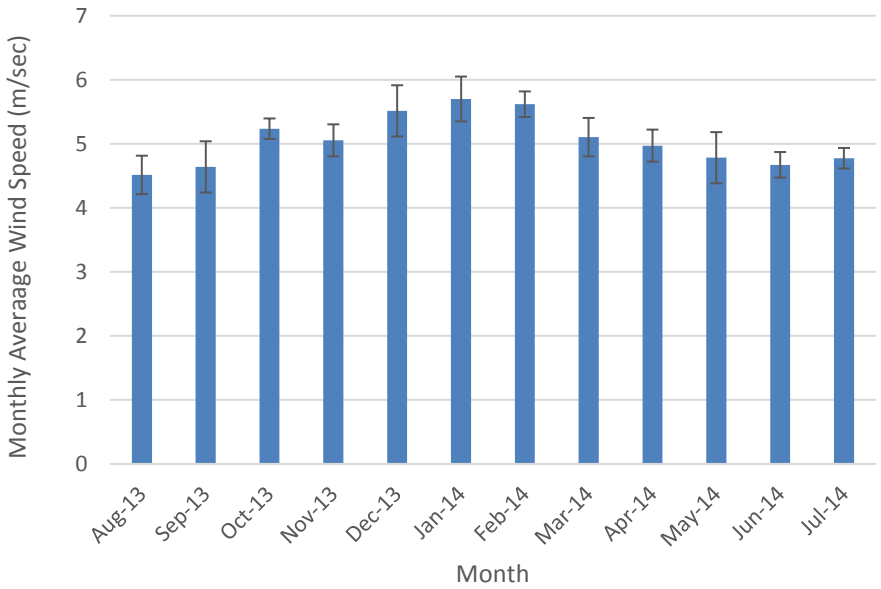

Fig. 2. 18: Estimated Average Wind Speed above the Roof of EV Building for Duration of One Year with the Corresponding Error Bars.

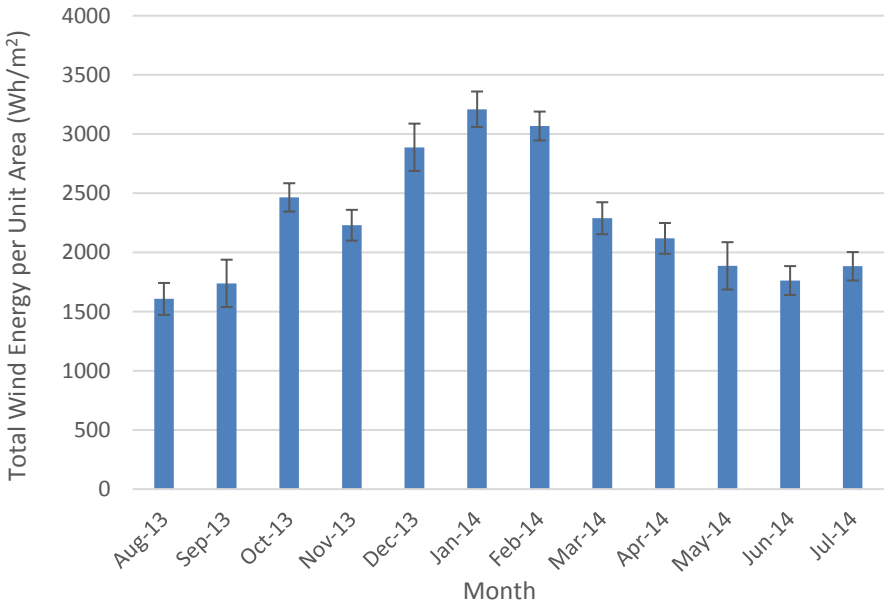

Fig. 2. 19: Estimated Total Wind Energy above the Roof of EV Building for Duration of One Year with the Corresponding Error Bars.

2.7 Testing the Methodology Using a non-Homogeneous Terrain

In order to generalize the use of this methodology, another case study was applied to Equiterre building, which is the Centre for Sustainable Development, a nonprofit organization whose mission is to build and operate a certified green building. This demonstration project aims to share space and resources with other social and environmental organizations and provide citizens, businesses and governments with information on sustainable development in Canada. Equiterre building is 23 m tall and it is surrounded by three high-rise buildings as shown in Fig. 2.20. These buildings are:

- Hydro-Quebec building which is 113 m tall.
- Complex Desjardins, which consists of two separate buildings:
  - Building 1 which is 123 m tall.
  - Building 2 which is 100 m tall.

The Equiterre building is around 20 km North-East from Dorval (PET) Airport. Its location with respect to the Dorval (PET) Airport is shown in Fig. 2.21. A photo for the Equiterre building is shown in Fig. 2.22.

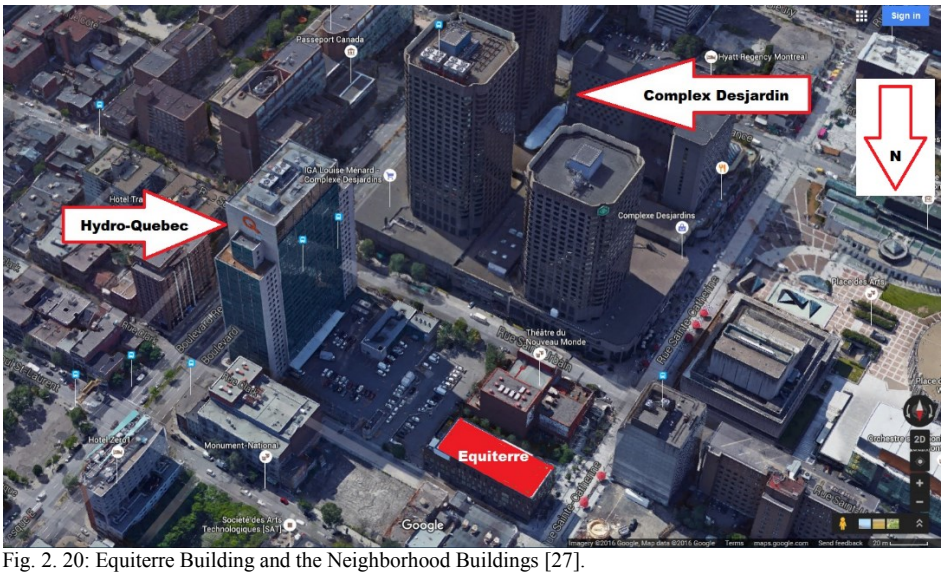

Fig. 2. 20: Equiterre Building and the Neighborhood Buildings [27].

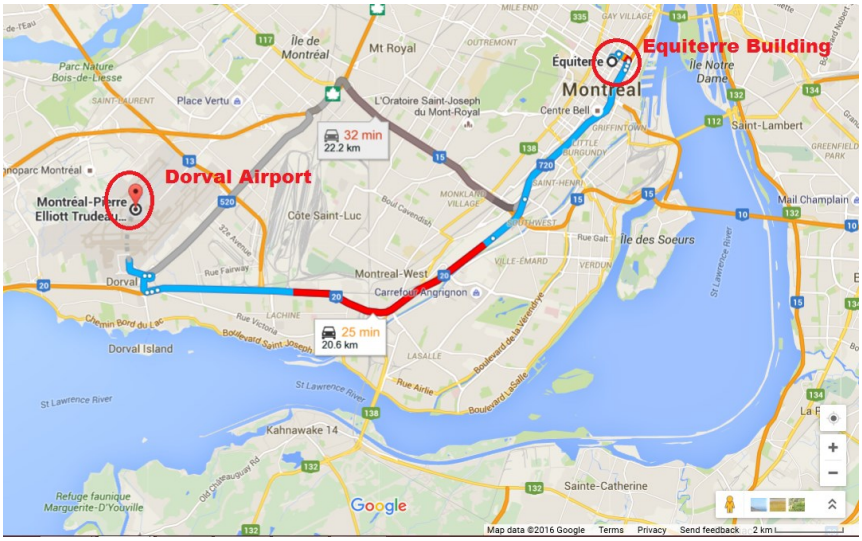

Fig. 2. 21: Equiterre Building Location with Respect to Dorval Airport [27].

Fig. 2. 22: Photo of Equiterre Building [28].

A three cup anemometer was installed in one corner above the roof of the Equiterre building, identical to the one on the roof of the EV building and with the same settings. Fig. 2.23 shows this anemometer at one meter height above the roof. The field measurement data- magnitude of the wind speed only - was collected for a 3-month period: November 1, 2012 to January 31, 2013.

This field data was used for wind energy calculations. Figs 2.24 and 2.25 show the monthly average wind speed and the total wind energy above the roof of the Equiterre building and their corresponding error bars. This data was significantly reduced in comparison to those obtained from the EV building - see Fig. 2.13 - but this was expected due to the lower height and the sheltering of the Equiterre building.

Fig. 2. 23: Installed Anemometer over the Roof of Equiterre Building where the North is toward the Corner of the Building.

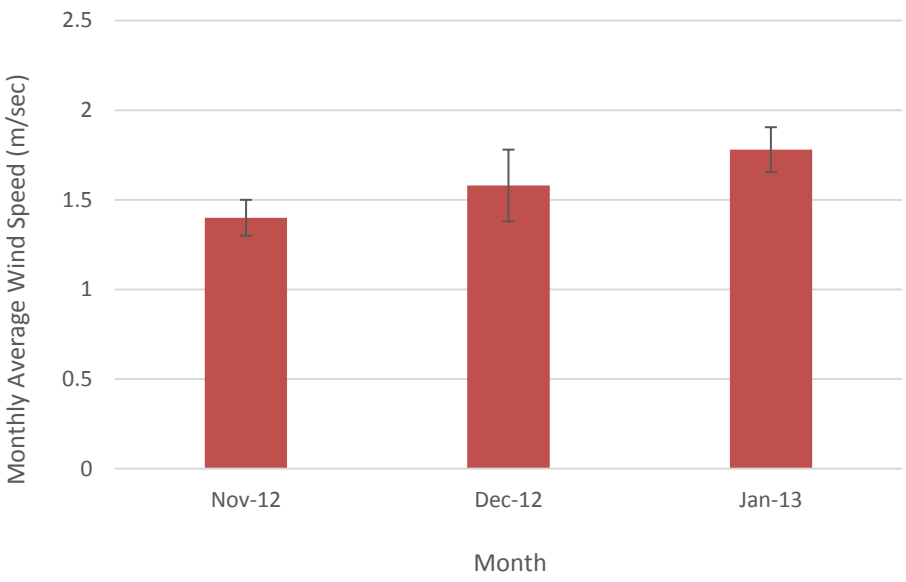

Fig. 2. 24: Monthly Average Wind Speed above the Roof of the Equiterre Building Using the Field Measurement Data with the Corresponding Error Bars.

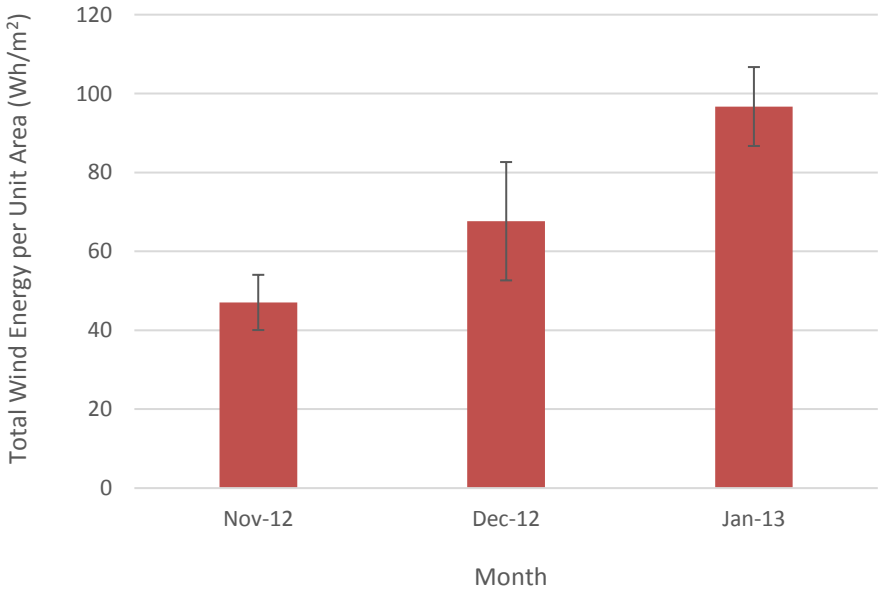

Fig. 2. 25: Monthly Calculated Wind Energy over the Roof of the Equiterre Building Using the Field Measurement Data with the Corresponding Error Bars.

For the corresponding period of the field measurement data, the wind speed and the wind energy were also estimated using the proposed methodology, which is the objective of this study. Using Eq. 2.4 again and by considering the first category in Table 2.1 which is applicable in this case, a correction factor of 0.63, evaluated as in the case of the homogeneous terrain, was used to estimate the wind speed upstream of the building at the same height with the installed anemometer above the roof of Equiterre building:

$$v_{2_{Eq}} = \frac{[24/460]^{0.33}}{[10/300]^{0.15}} \times v_1 = 0.63 \times v_1 \tag{2.11}$$

where:

$v_{2_{Eq}}$ The wind speed profile upstream the buildings at the same height of the installed anemometer over Equiterre building.

In order to estimate the wind speed over this building, wind tunnel measurements were again carried out to find the ratio between the wind speeds upstream to the wind speeds above the roof of the Equiterre building. For this purpose, a complete model of the Equiterre Building and the surroundings was built in the wind tunnel, as shown in Fig. 2.26. The model was built to a scale of 1:400. Fig. 2.27 shows the approximate schematic diagram of the top view of the model, indicating the location of the anemometer [23] [24].

The simulated wind flow in the wind tunnel was used to evaluate the ratios from several wind directions as in the case of the homogeneous terrain. Table 2.4, similarly with Table 2.2, shows the wind directions and their corresponding ratios. It can be shown from Table 2.4 that there is a significant variation in the ratio of the Equiterre building case. This is occurred due to the inhomogeneity in the surrounded buildings as previously discussed.

If v_{3Eq} is the wind speed profile for one year estimated above the roof of Equiterre building, then:

$$v_{3_{Eq}} = \text{Ratio} \times v_{2_{Eq}} \tag{2.12}$$

As in the homogeneous terrain case, a complete hourly wind speed profile for one year was obtained. Then the wind speeds were averaged for each month to be used for power and energy estimation. A comparison between the estimated wind speeds and estimated wind energy with the field measurements values are shown in Figs. 2.28 and 2.29, as in the previous case.

The obtained results show that the error between the wind energy field measurement and the estimation using the wind tunnel is less than 20% as shown in Table 2.5, which means that this method can be used in the case of non-homogeneous terrain but for initial stages of wind energy estimation only. Using the estimated wind speed profile for a duration of one year, the wind energy was evaluated for the corresponding period using Eq. 2.7, as in the previous case. Figs 2.30 and 2.31 show the estimated monthly average wind speed and total energy for the Equiterre building case.

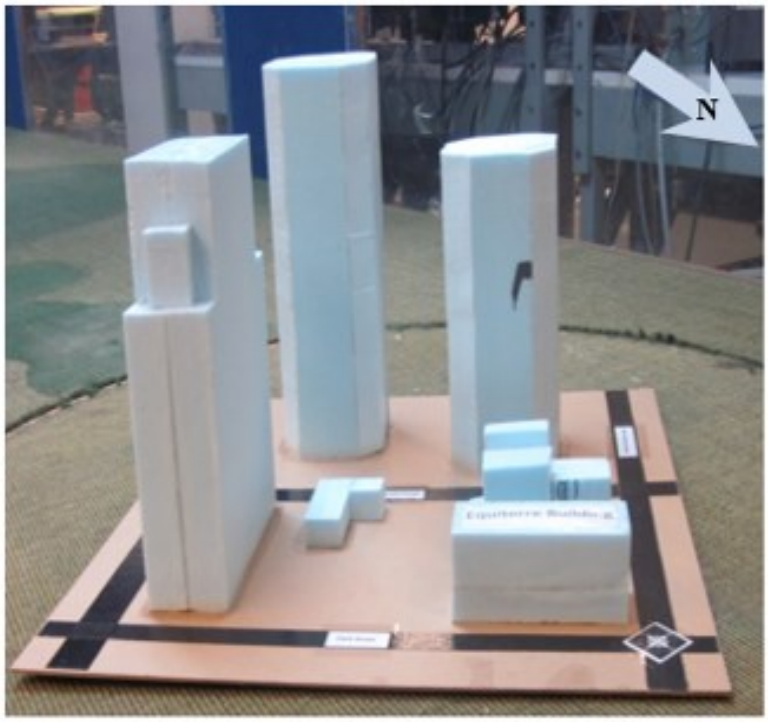

Fig. 2. 26: Equiterre Building Model and the Surroundings.

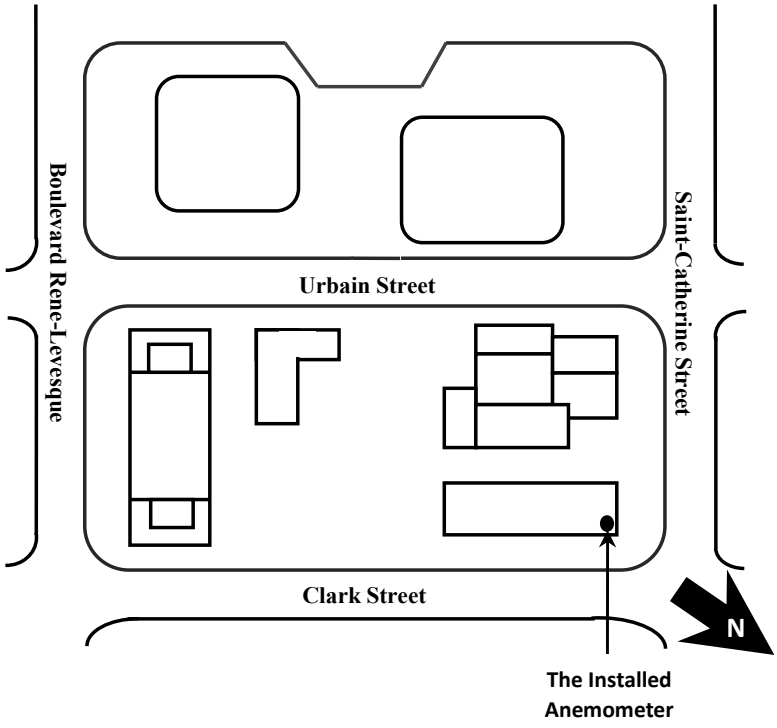

Fig. 2. 27: Approximate Schematic Diagram of the Top View of the Equiterre Building and the Surroundings

Table 2. 4: Wind Directions under the Wind Tunnel Tests and their Corresponding Ratios for Equiterre Building (Eq. 2.6).

Direction	Ratio	Direction	Ratio
1	0.98	20	0.46
3	0.95	21	0.49
5	0.98	22	0.54
7	1.07	23	0.91
9	1.1	24	1.0
11	1	25	1.1
13	0.56	26	0.93
15	0.20	27	1
17	0.36	29	1.1
18	0.45	31	0.98
19	0.50	33	0.93

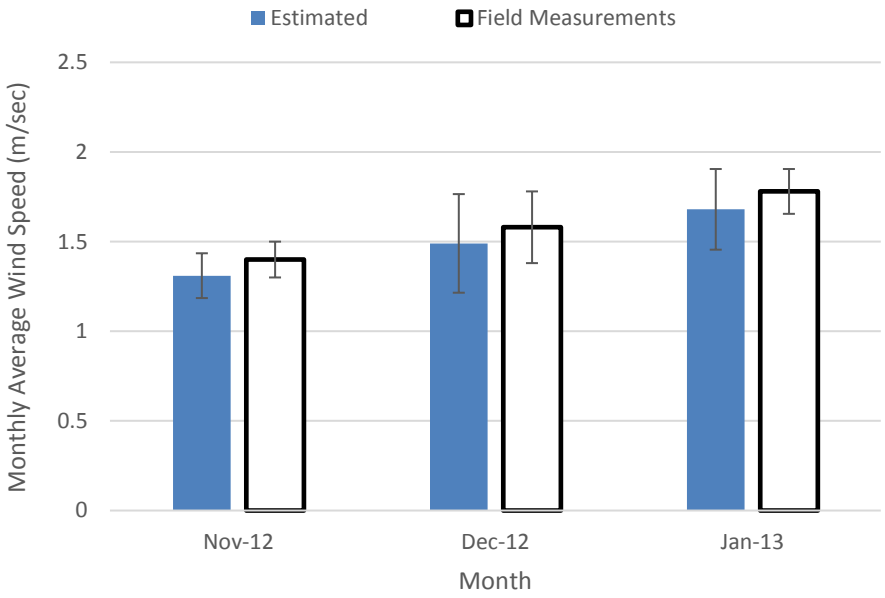

Fig. 2. 28: Wind Speed Field Measurement Data and the Estimated Values above the Roof of Equiterre Building with the Corresponding Error Bars.

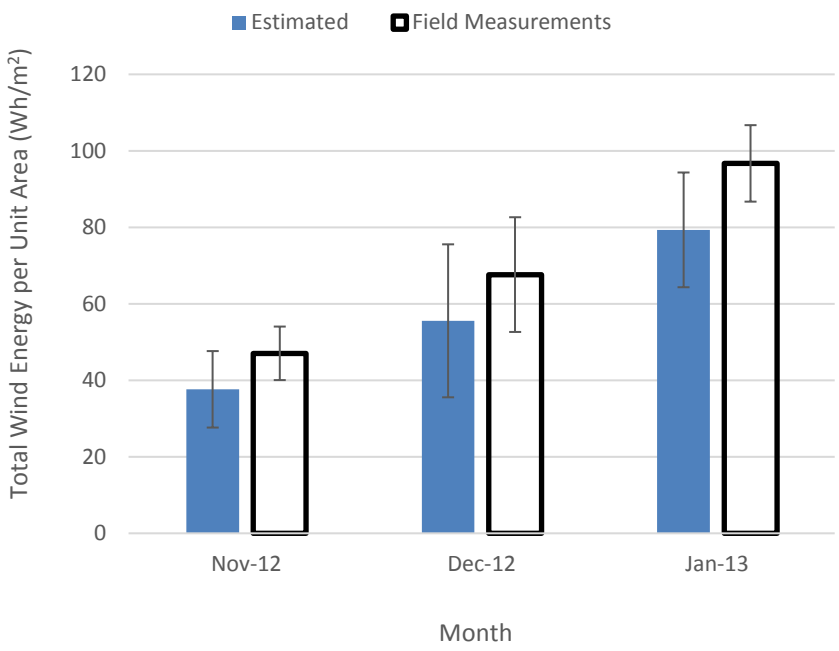

Fig. 2. 29: Total Wind Energy Using the Field Measurement Data and the Estimated Value above the Roof of Equiterre Building with the Corresponding Error Bars.

Table 2. 5: The Error between the Field Measurements and the Estimation of the Wind Energy at the Roof of Equiterre Building.

Month	Error (%)
August 2013	19.9
September 2013	17.8
October 2013	17.9

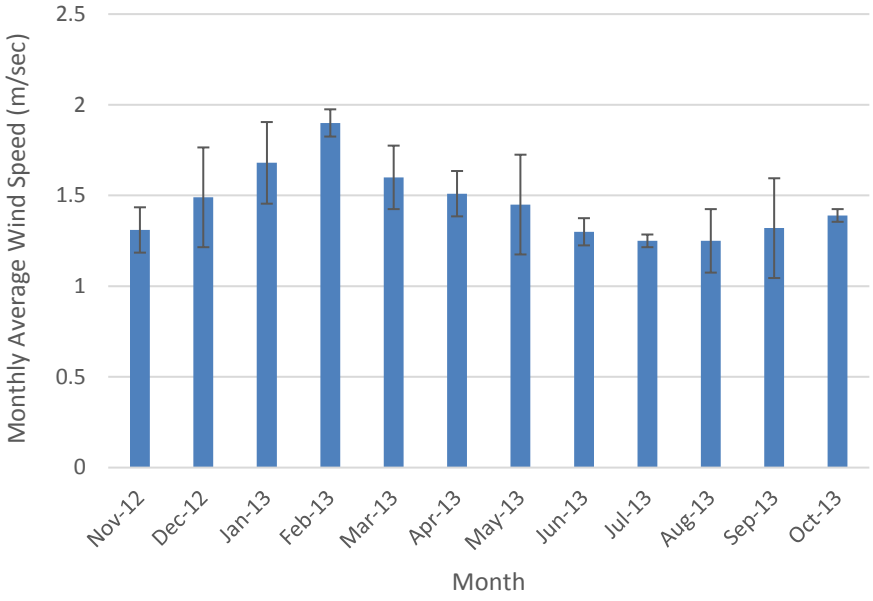

Fig. 2. 30: Estimated Average Wind Speed above the Roof of Equiterre Building for a Duration of One Year with the Corresponding Error Bars.

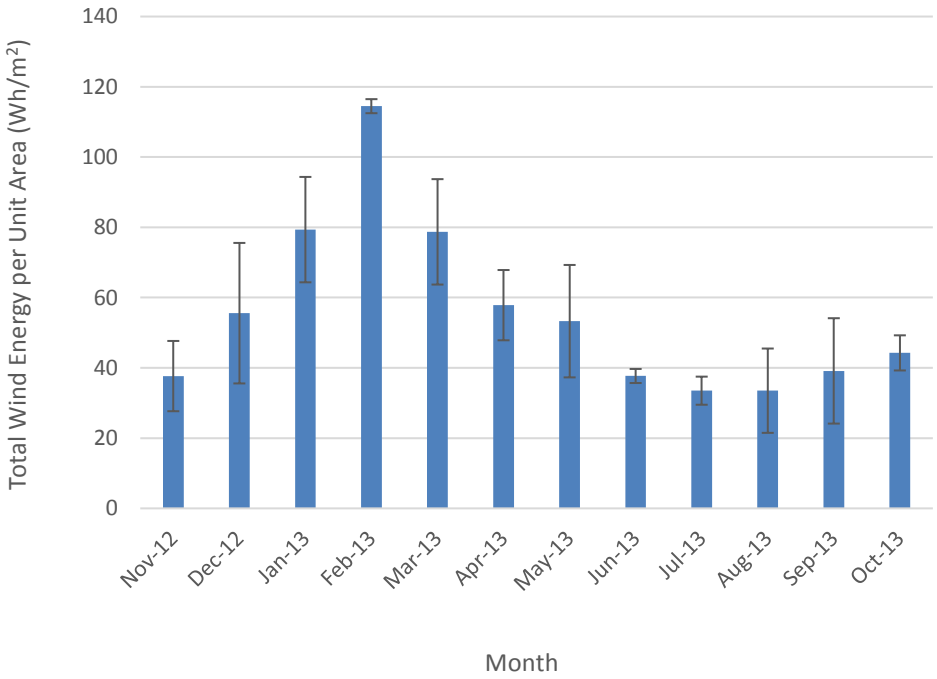

Fig. 2. 31: Estimated Calculated Total Wind Energy above the Roof of Equiterre Building for a Duration of One Year with the Corresponding Error Bars.

2.8 Conclusion

A methodology for estimating the wind power and energy for all terrains in the urban environment in Montreal using the wind tunnel is presented in this chapter. Two case studies were discussed in detail. In the first case of homogeneous terrain, the results show a high correlation between the estimation of the wind energy using the proposed methodology and the field measurements calculation over the roof of the EV building.

In the second case where the terrain is highly non-homogeneous, the discrepancy is higher.

In general, the accuracy of this methodology depends on the complexity of the upstream terrain. Therefore, this methodology of estimating the wind power and energy can be very useful especially for homogeneous upstream terrains.

CHAPTER 3: A NOVEL VOLTAGE CONTROL STRATEGY OF A PERMANENT MAGNET WIND GENERATOR

3.1 Introduction

In the last few years, wind turbines have become one of the most popular methods for renewable energy power production. At the end of 2013, the global installed capacity of both on-shore and off-shore wind turbines was 318 GW, which is a 12% increase compared to the year before [40][41]. Most of these turbines have a rated power of a few MWs. However, smaller wind turbines have great potential because they are ideal for distributed generation units on the top of residential or industrial buildings and micro or nano-grids[41]. Different types of generators are used in the construction of the small wind turbines. The most popular one is the PMG.

PMGs are widely used in various applications, especially in the wind power generation system with variable speed operation. In order to provide a DC power supply, the PMG is connected to rectifier with a low pass filter (LPF) to stabilize the DC output voltage[42]. The field excitation of the PMGs is usually constant. Thus, the back emf of the machine increases with the rotor speed. In order to control the DC voltage over a wide speed range, the field excitation has to be adjusted.

In the literature, several control techniques have been studied for WECS. The voltage regulation at the Point of Common Coupling (PCC) is achieved through a reactive power controller [43] [44]. Using this controller the WECS produces reactive power when the voltage is less than the grid nominal voltage and it absorbs it in the opposite case. Also several power controllers are proposed to optimally control the power generated by the turbine and effectively manage the power that is supplied to different loads for a stand-alone WECS [45][46].

A special power electronic configuration (Vienna Rectifier) and its controller are proposed in [47] to improve the efficiency of the WECS. Moreover, field control of the PMG has been proposed using several methods, especially using mechanical and electromagnetic techniques. The authors in [48] propose a mechanical method for the field regulation of the two rotor axial-flux PMGs based on changing the relative angle between these two rotors. Another mechanical method for the field regulation of the axial-flux PMG is based on changing the distance between the stator and the rotor [49]. Several techniques are proposed for the electromagnetic field regulation such as hybrid excitation which combine the permanent magnet flux with the variable flux generated by the stator field winding [50]. Extension of the speed range by flux-weakening operation is widely used in the Permanent Magnet Synchronous Motor (PMSM) [51]-[52]. However, few papers are concerned about field weakening operation and the speed range extension for the PMG. Moreover, no clear approaches are provided.

This chapter presents a new technique to control the flux of the PM machine by varying the d-axis stator current. By selecting a suitable value of d-axis current, the terminal voltage of the PM generator can be regulated for variable wind speed. Consequently, the terminal voltage across the load is also regulated. No special mechanical techniques or additional electromagnetic coils are used to achieve this goal. This technique can be used for small wind turbine to provide dc loads or medium size turbine to supply ac loads in micro-grids. Moreover, it provides an improvement in permanent magnet generator control, with the application to wind generators. Also it can be applied to PM generators fed from other renewable or conventional sources.

The primary aim is to develop a new way for voltage regulation which up to now has not been done for these applications when fed with a PM generator.

In order to enhance or reduce the flux of the PMG, an active rectifier has to be connected with the machine. The active rectifier helps the regulating current, $-i_d$ for weakening the flux or $+i_d$ for enhancing the flux, to be injected to the machine.

These regulating currents help not only to control the output voltage, but also to extend the speed range of the machine. In order to carry out this objective, a Hysteresis Current Controller (HCC) has been utilized to design the controller which generates the gate pulses of the active rectifier in the PMG system.

This chapter is organized as follows: section 3.2 discusses the WECS and its implementation in detail, section 3.3 discusses the implementation of the control system using the HCC, and section 3.4 discusses the permanent magnet operation. Section 3.5 presents the case study in which the experimental setup is explained. In section 3.6 the results based on HCC are observed and analyzed. Finally, conclusions of the chapter are presented in section 3.7.

3.2 Implementation of the Wind Energy Conversion System

Fig. 3.1 shows the WECS based on PMG wind turbine. The system starts from the wind turbine and ends at the electrical grid at the PCC. The grid side converter is simplified by a constant DC voltage link from the broken red line. This simplification is assumed based on running the generator in a stand-alone mode to supply dc loads. The simplified model of the WECS is shown in Fig. 3.2. For a deeper understanding of WECS, each part will be described individually in this section.

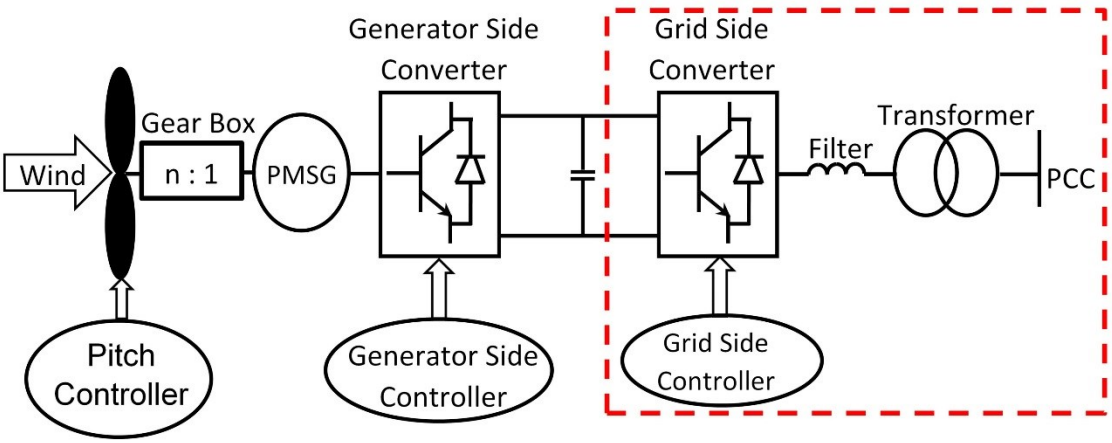

Fig. 3. 1: Block Diagram of WECS Based on PMG Wind Turbine.

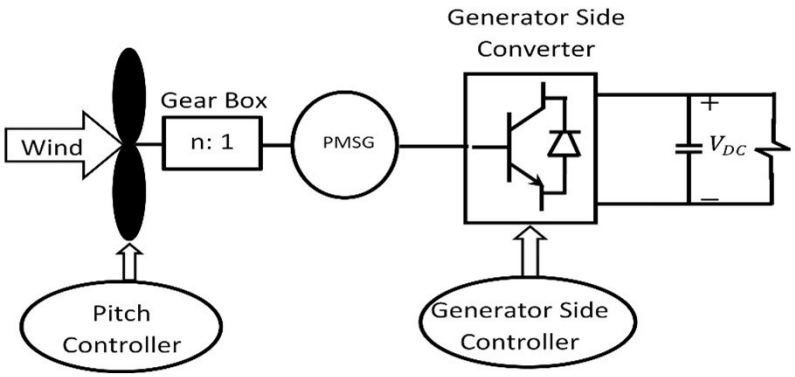

Fig. 3. 2: The Simplified Model of the WECS.

3.2.1 Wind Energy

The wind is the movement of the air from areas with high pressure to areas with low pressure. The wind power depends on several factors which are related as follows:

$$P_w = 0.5\rho A v^3 \tag{3.1}$$

Where:

P_w Wind Power.

ρ Air density (1.225kg.m3).

A Cross-sectional area of the wind.

v Wind Speed (m/sec).

3.2.2 Wind Turbine Model

The wind energy cannot be transferred to mechanical energy with 100% efficiency conversion. The extracted energy from the wind turbines is limited by their power coefficients (C_p), which depend on manufacturer and geometrical parameters.

Usually C_p is given by a function of two parameters $C_P(\lambda,\beta)$ [53]:

$$C_P(\lambda,\beta) = c_1\left(\frac{c_2}{\lambda_i} - c_3\beta - c_4\right)e^{\frac{-c_5}{\lambda_i}} + c_6\lambda \tag{3.2}$$

Where:

$$\lambda = \frac{\omega_{wT}R}{v} \tag{3.3}$$

$$\frac{1}{\lambda_i} = \frac{1}{\lambda + 0.08\beta} - \frac{0.035}{\beta^3 + 1} \tag{3.4}$$

And:

ω_{wT} Speed of the wind turbine.

Fig. 3.3 shows $C_p - \lambda$ curves at different pitch angles. It can be observed that when the pitch angle is equal to 0 degree, the peak value of the power coefficient ($C_{p\_\max}$) is 0.48, which is less than Betz's Limit (0.59). The corresponding value of λ is 8.1. This value is called the optimum tip speed ratio (λ_{opt}) and it is considered the optimum working point at wind speeds below the rated value. By increasing the value of the pitch angle, it can be seen that the power coefficient becomes smaller.

The extracted power and the developed torque from the wind turbine can be calculated as follows [53]:

$$P_{wT} = 0.5\rho\pi R^2 C_p(\lambda,\beta)v^3 \tag{3.5}$$

$$T_{wT} = P_{wT}/\omega_{wT} \tag{3.6}$$

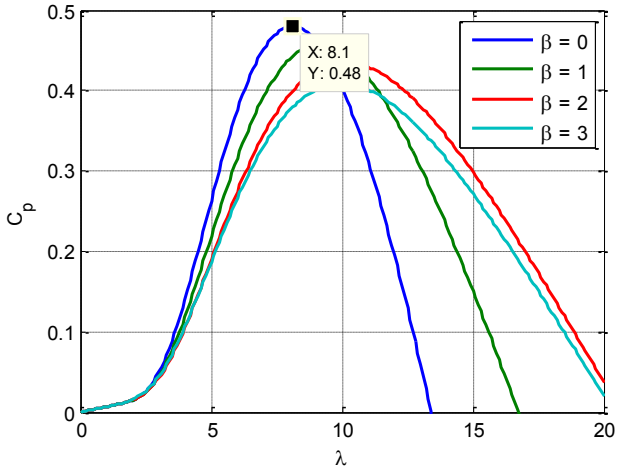

Fig. 3. 3: Cp-λ Curves at different Pitch Angles.

Fig. 3.4 shows the power speed characteristics for the wind turbine. It can be shown that the wind turbine model is divided into four regions (R1, R2, R3 and R4). According to the wind speed, the wind turbine needs to be controlled in different modes of operation as follows [55]:

1. Parking Mode (R1): when the wind speed is lower than the cut-in speed (V_{cut_in}), the wind turbine will not rotate due to the fact that the electrical power generated by the PMG system is insufficient to compensate for the internal power losses in the system.
2. MPPT mode (R2): when the wind speed is greater than (V_{cut_in}), the wind turbine starts to work and generate electrical power. The wind speed in this region is relatively low and the power captured by the wind turbine is below its rated value.

Thus, the MPPT control needs to be applied to ensure a maximum power efficiency of the wind turbine.

3. Constant power region (R3): when the wind speed is greater than the rated speed (V_{Rated}) and less than the cut-out speed (V_{cut_out}), the power generated by the wind turbine will be larger than its rated limit if the MPPT control is still applied.

   Thus, the electrical stress on the PMGs will increase and would further damage them. Therefore, the blade angle of the wind turbine needs to be controlled in this region to keep the system operating within its rated output limit.

4. Braking Mode (R4): when the wind speed is greater than (V_{cut_out}), the wind turbine system should completely shut down to protect the system from the damage. This can be done by adjusting the blade angle to 90°.

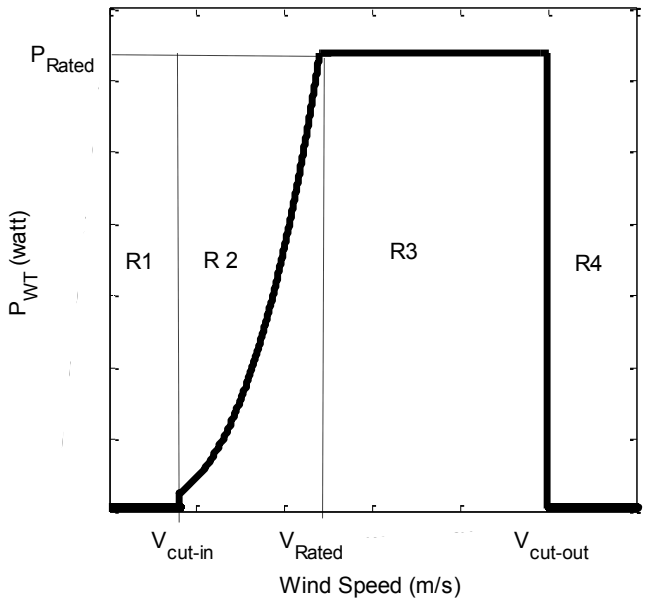

Fig. 3. 4: Wind Turbine Power Curve.

3.2.3 Pitch Control

Pitch control is the most commonly used technique for controlling the aerodynamic power generated by a turbine rotor. The aims of this controller are:

- Producing power as much as possible in the range of slow speed, where in general there is no need to vary the pitch angle. The pitch angle should only be at its optimum value to produce maximum power.
- Keeping the aerodynamic power constant at its rated value in the range of high speed, so that the design limits are not exceeded. This is done by rotating the rotor blades around their own axis to reduce the attack angle of the wind. Usually the range of the pitch angle is between 0° and 24° [55].

3.2.4 Gear Box and Drive Train Model

The mechanical power from the rotation of the wind turbine rotor is transferred to the generator through the drive train which is composed of wind rotor, main shaft, and gear box. Fig. 3.5 shows the implemented drive train model.

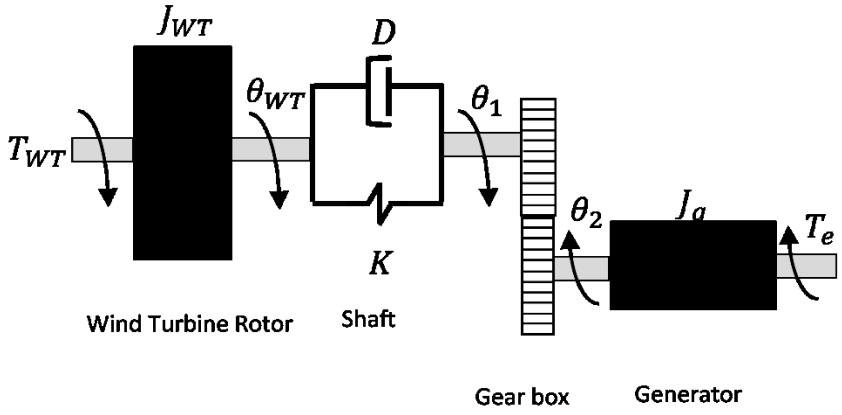

Fig. 3. 5: The Drive-Train Model with Gearbox.

The drive train can be described by the following set of equations [55]:

$$x = \frac{d\theta_2/dt}{d\theta_1/dt} \tag{3.7}$$

$$T_{WT}^{'} = \frac{T_{WT}}{x} \tag{3.8}$$

$$J_{WT}^{'} = \frac{J_{WT}}{x} \tag{3.9}$$

$$K^{'} = \frac{K}{x} \tag{3.10}$$

$$D^{'} = \frac{D}{x} \tag{3.11}$$

$$J_{WT}^{'} \frac{d^2\theta_{WT}^{'}}{dt^2} = T_{WT}^{'} - K^{'}(\theta_{WT}^{'} - \theta_m) - D^{'}(\frac{d\theta^{'}{}_{WT}}{dt} - \frac{d\theta_m}{dt}) \tag{3.12}$$

$$J_g \frac{d^2\theta_m}{dt^2} = K^{'}(\theta_{WT}^{'} - \theta_m) + D^{'}(\frac{d\theta_{WT}^{'}}{dt} - \frac{d\theta_m}{dt}) + T_e \tag{3.13}$$

3.2.5 PMG Model

The dynamic model of the PMG has been built in the synchronous d-q rotating reference frame, where the q-axis is ahead 90^o from the d-axis with respect to the direction of rotation [42] [54]. The equivalent circuits of the Q and D axis of the PMG respectively are shown in Fig. 3.6.

The q and d axis stator voltages are given by:

$$-v_q = Ri_q + p\lambda_q - \omega_s\lambda_d \tag{3.14}$$

$$-v_d = Ri_d + p\lambda_d - \omega_s\lambda_q \tag{3.15}$$

Where:

$$\lambda_q = L_q i_q \tag{3.16}$$

$$\lambda_d = L_d i_d + \lambda_{af} \tag{3.17}$$

The electrical torque equation of the PMG is given by:

$$T_e = \frac{-3}{2} P(\lambda_{af} i_q + (L_d - L_q) i_d i_q) \tag{3.18}$$

And the machine dynamic equation is given by:

$$T_e = T_L + B\omega_r + Jp\omega_r \tag{3.19}$$

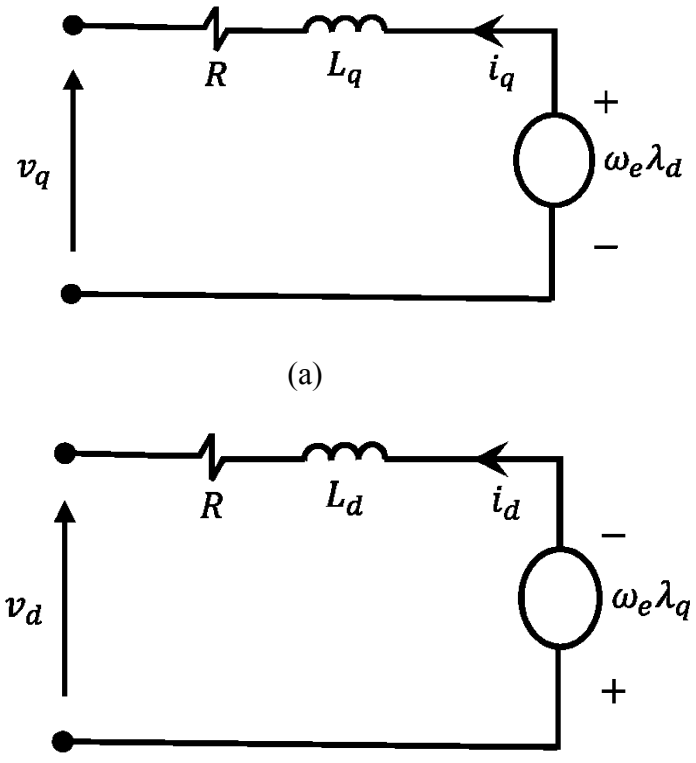

Fig. 3. 6: Dynamical Model for PMG. (a) q-axis Circuit (b) d-Axis Circuit.

Fig. 3.7 shows phasor diagram of the dynamic model of the PMG in the d-q reference frame. The dynamical model of the PMG can be represented in the rotor reference frame using (3.14) - (3. 19) [54] [70]:

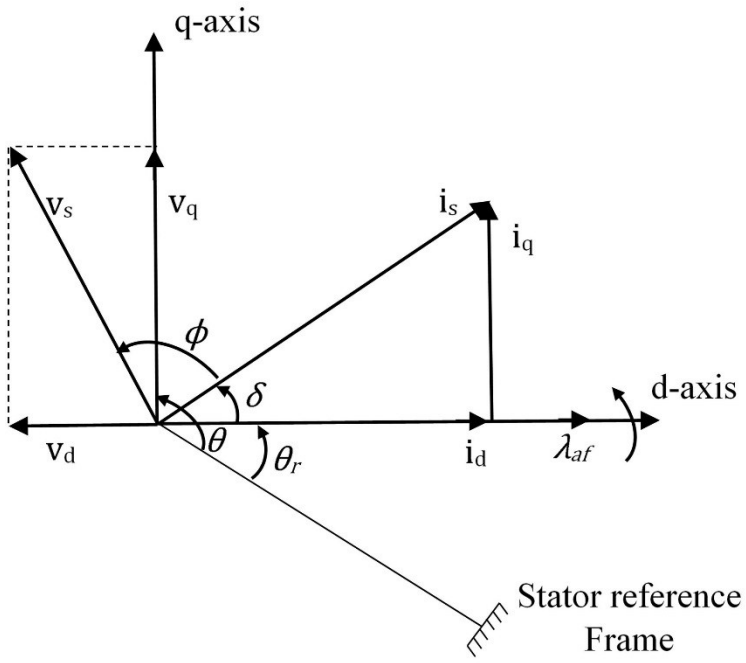

Fig. 3. 7: Phasor Diagram of PMG.

The d and q axes currents are constant in the d-q reference frames, since δ is constant for a given load torque. Thus, they are very similar to the armature and field currents in the separately-excited dc machine.

The q axis current is equivalent to the armature current of the dc machine, while the d axis current is similar to the field current. The other part is contributed by the equivalent current source representing the permanent magnet field. If δ is negative with respect to the rotor flux linkages, the machine becomes a generator.

3.3 Implementation of the Control System

The proposed system configuration of the simplified WECS is illustrated in Fig. 3.2. The DC link voltage V_{DC} is represented across a resistive load. The PMG rotor speed and its position are measured using an absolute encoder.

The 3-ph armature currents i_a, i_b and i_c are obtained with ac current sensors, while the 3-ph voltages v_a, v_b and v_c are obtained with ac voltage sensors and their fundamental components were obtained through a low pass filters.

A DC voltage sensor feeds back the output voltage. The major part of the controller function is the implementation of the closed-loop control and the pulse generation of the active rectifier. Both V_{DC}^* and V_{DC} are the input of the controller, so as to generate a Q-axis current reference i_q^* with a PI controller. The D-axis current reference i_d^* is also input to the controller module. Also, the 3-ph armature currents i_a, i_b and i_c as well as the rotor speed ω and the rotor angle position θ are all fed into the controller module. In order to generate gate pulses for the active rectifier, HCC has been used and consequently the currents of the PMG has also been injected to the controller. This closed-loop controller is used to make V_{DC} track V_{DC}^* closely. In this chapter, i_q^* is directly injected into the controller module to study its influence on V_{DC} at different rotational speeds.

The HCC is implemented inside the controller module. With a given i_q^* and i_d^*, the 3-ph armature current references i_a^*, i_b^* and i_c^* are obtained using the required frame transformation. Then, the 3-ph armature currents are compared with references to generate the gate signals of the active rectifier using the HCC.

Always, the upper and the lower switches of the active rectifier are on opposite status. Fig. 3.7 shows the schematic diagram of the controller module.

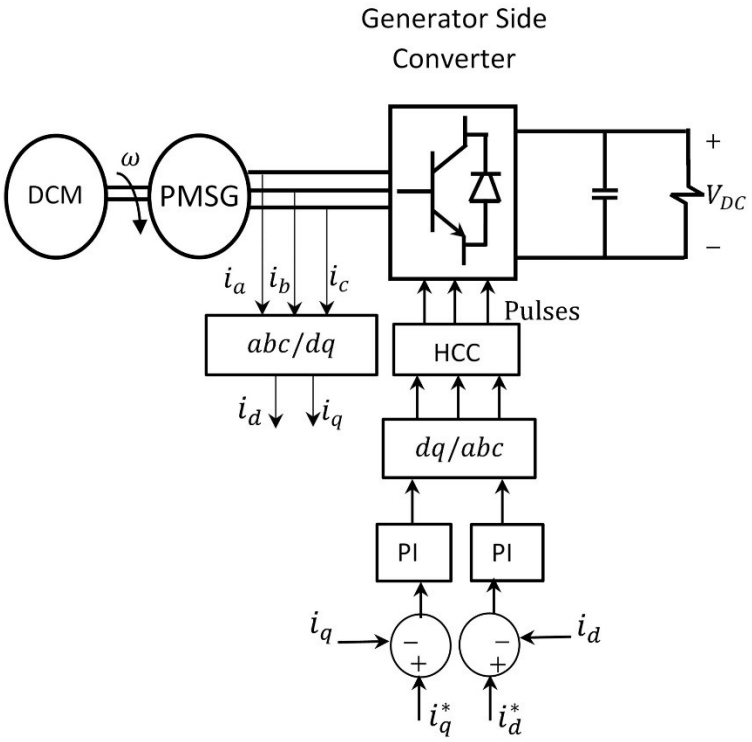

Fig. 3. 8: Schematic Diagram of the Controller Module.

3.4 Permanent Magnet Operation

The operating flux density on the demagnetization characteristics can be written as, assuming it is straight line:

$$B_m = B_r + \mu_0 \mu_m H_m \tag{3.20}$$

The operating point of the magnet is shown in Fig. 3.8. The line connecting the operating flux density B_m and the origin is known as the air-gap line. When the stator is excited electrically, a demagnetizing current is flown. Then the air-gap line moves in parallel to the original one and the operating point is moving from point A to point B as shown in Fig. 3.9.

Therefore, the operating flux density is decreased from B_m to B'_m. Also, when the flux control is applied by injecting $+i_d$ for the flux enhancing control, or $-i_d$ for the flux weakening control, the operating point moves to point D or point C respectively.

Thus, the operating point flux density of the magnet is increased or decreased accordingly as shown in Fig. 3.9.

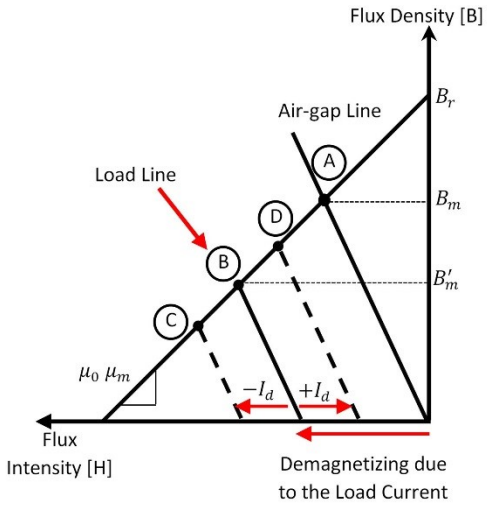

Fig. 3. 9: Operating Point of the Magnets.

3.5 Case Study

3.5.1 System Parameters

A case study has been applied using the simplified model of the WECS, where a resistive load is assumed to be in the DC side. The parameters of the system are shown in Table 3.1.

Table 3. 1: Parameters of the Case Study.

Wind Turbine Rotor	Blade Length	2m
	$V_{cut\text{-}in}$	4 m/s
	V_{Rated}	12 m/s
	$V_{cut\text{-}out}$	25 m/s
	λ_{opt}	8.1
	C_p Coefficients [c1-c6]	[0.5176, 116, 0.4, 5, 21, 0.0068]
Drive Train	J_{wT}	3 kg.m^2
	J_g	0.03334 kg.m^2
	K	0.3 N.m/rad
	D	1 N.m.s/rad
PMG	P_{rated}	5kw
	p	4 poles
	R	0.1718
	[L_q, L_d]	[0.00514, 0.01419]
	λ_{af}	0.591
	B	0.004252

3.5.2 Experimental Work

Experimental setup was carried out to validate the selected case-study system. The Wind Turbine (WT) was implemented with the dc machine driven by a buck converter. Figs. 3.10-3.13 shows the WT experimental setup bench. The torque developed by the WT is controlled via armature current and a PI controller. The control logic of the WT was implemented with a DS-1103 from dSPACE. A user interface was developed with ControlDesk for varying parameters such as the wind speed and the inertia of the wind turbine.

In order to approximate the performance of the discrete-time microcontrollers which are commonly used in the industrial control systems, the simulation type for the controller in the Simulink file is set as a discrete-type with a sampling time of 50μsec. The buck converter, supplied by a three-phase diode bridge rectifier, was employed for controlling the armature current and consequently the developed torque by the WT. A HCC was used to achieve fast response of the current loop.

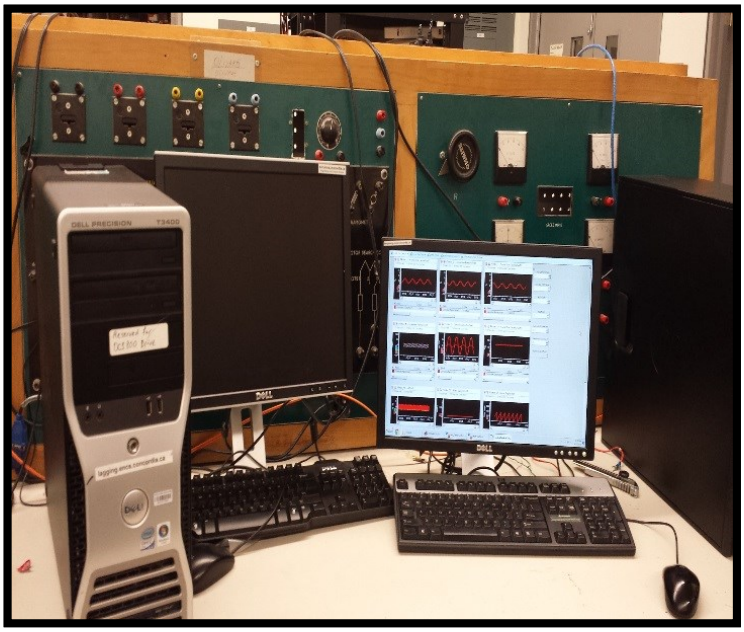

Fig. 3. 10: Digital Control System Based on Computer Application.

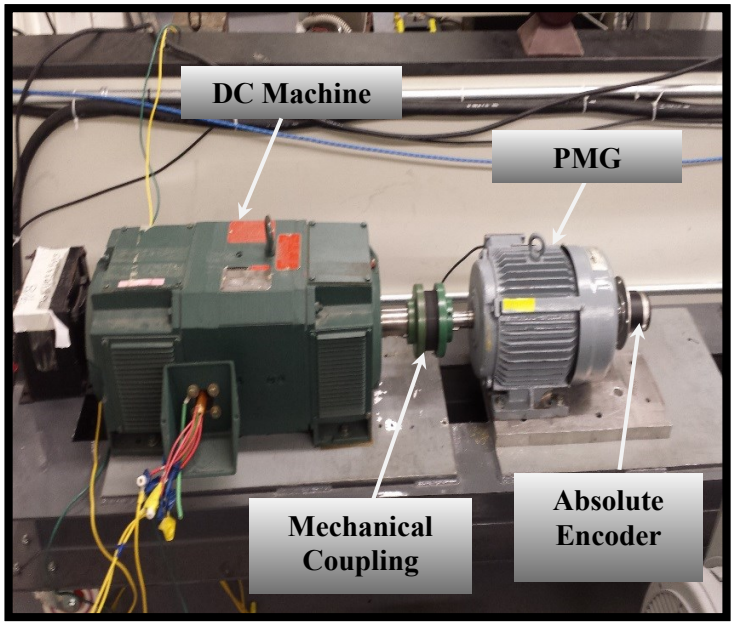

Fig. 3. 11: PMG Driven by DC Machine for Wind Turbine Emulation.

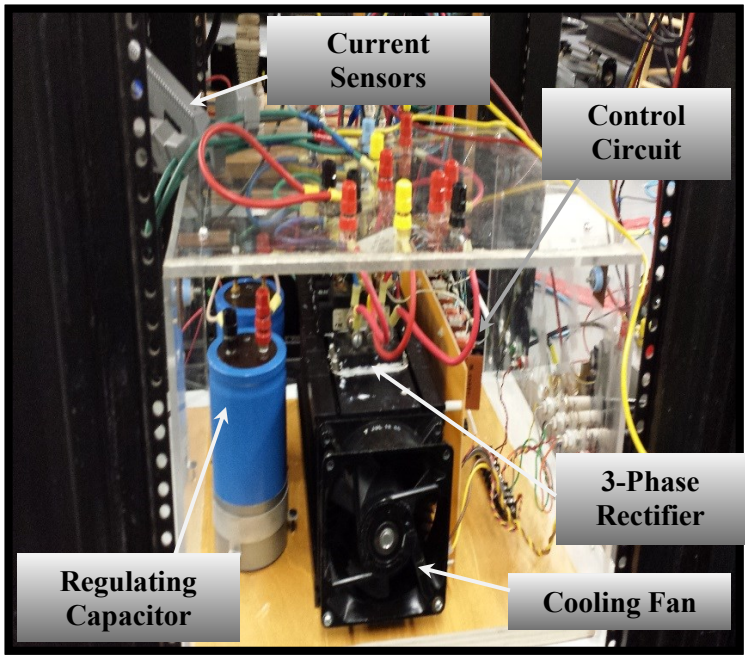

Fig. 3. 12: Three Phase PWM Rectifier.

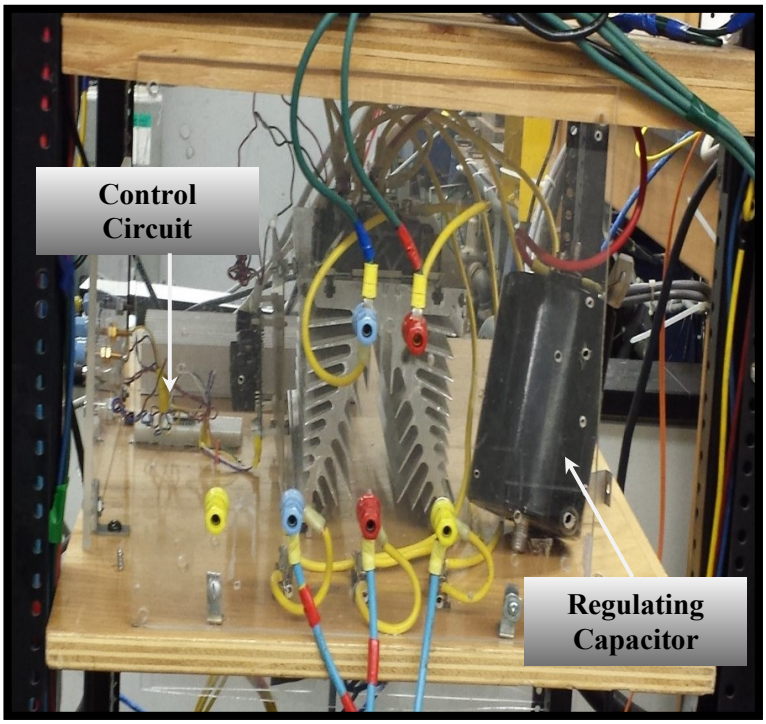

Fig. 3. 13: DC-DC Based Step-Down (Buck) Converter to Drive the Emulated Wind Turbine Using the DC Machine.

3.6 Results and Discussions

3.6.1 Voltage Regulation Based Field Controller of PMG

In order to indicate the effectiveness of the flux control in the voltage regulation purposes, three scenarios will be discussed as follows:

1. The injected i_d current is zero, while the rotor speed is increased by a step function.
2. The injected i_d current is negative, while the rotor speed is increased by a step function.
3. The injected i_d current is positive, while the rotor speed is decreased by a step function.

In the first scenario when (i_d =0), the amplitude of the 1st harmonic of the terminal line voltage increased when the rotor speed increased from 400 rpm to 600 rpm as shown in Fig. 3.14.

In the second scenario, several cases of injecting a demagnetizing current (i_d < 0) has been studied to investigate its effect on the voltage regulation when the rotor speed steps up from 400 rpm to 600 rpm. These cases are shown in Figs. 3.15-4.17. For the first case when (i_d = -2A), it can be seen from Fig. 3.15 (B) that the increase in the 1st harmonic of the line voltage is reduced compared to the previous scenario. For the second case when (i_d = -4A), the regulation of 1st harmonic of the line voltage has been improved compared to (i_d = -2A) as shown in Fig. 3.16(A).

For the third case when (i_d = -6A), it can be seen from Fig 3.17 (B) that the amplitude of the 1st harmonic of the line voltage is completely regulated. The explanation of this voltage regulation by injecting a demagnetizing current is described as follows:

The demagnetizing current produces a flux opposing the magnet flux.

Thus, the total air-gap flux and the terminal voltage of the machine have been reduced. Further increase of the demagnetizing current is not necessary, since the voltage is clearly regulated.

In the third scenario, where the wind speed is changed from high speed to low speed, a magnetizing current ($i_d > 0$) has to be applied for voltage regulation purposes.

Three cases have been studied to investigate the effect of the magnetizing current on the voltage regulation when the rotor speed steps down from 800 rpm to 600 rpm.

For the first case when (i_d =0), the 1st harmonic of the line voltage is reduced as shown in Fig. 3.18 (B).

For the second case when (i_d = +2A), the 1st harmonic of the line voltage is not completely regulated but it's better than the line voltage for the first case as shown in Fig. 3.19 (B). For the third case when (i_d = +4A), the 1st harmonic of the line voltage has been completely regulated as shown in Fig. 3.20 (B).

The explanation of this voltage regulation by injecting a magnetizing current is described as follows: The magnetizing current produces a flux enhancing the magnet flux. Thus, the total air-gap flux is increased and the terminal voltage of the machine has been regulated. Further increase of the magnetizing current is not necessary, since the voltage is clearly regulated.

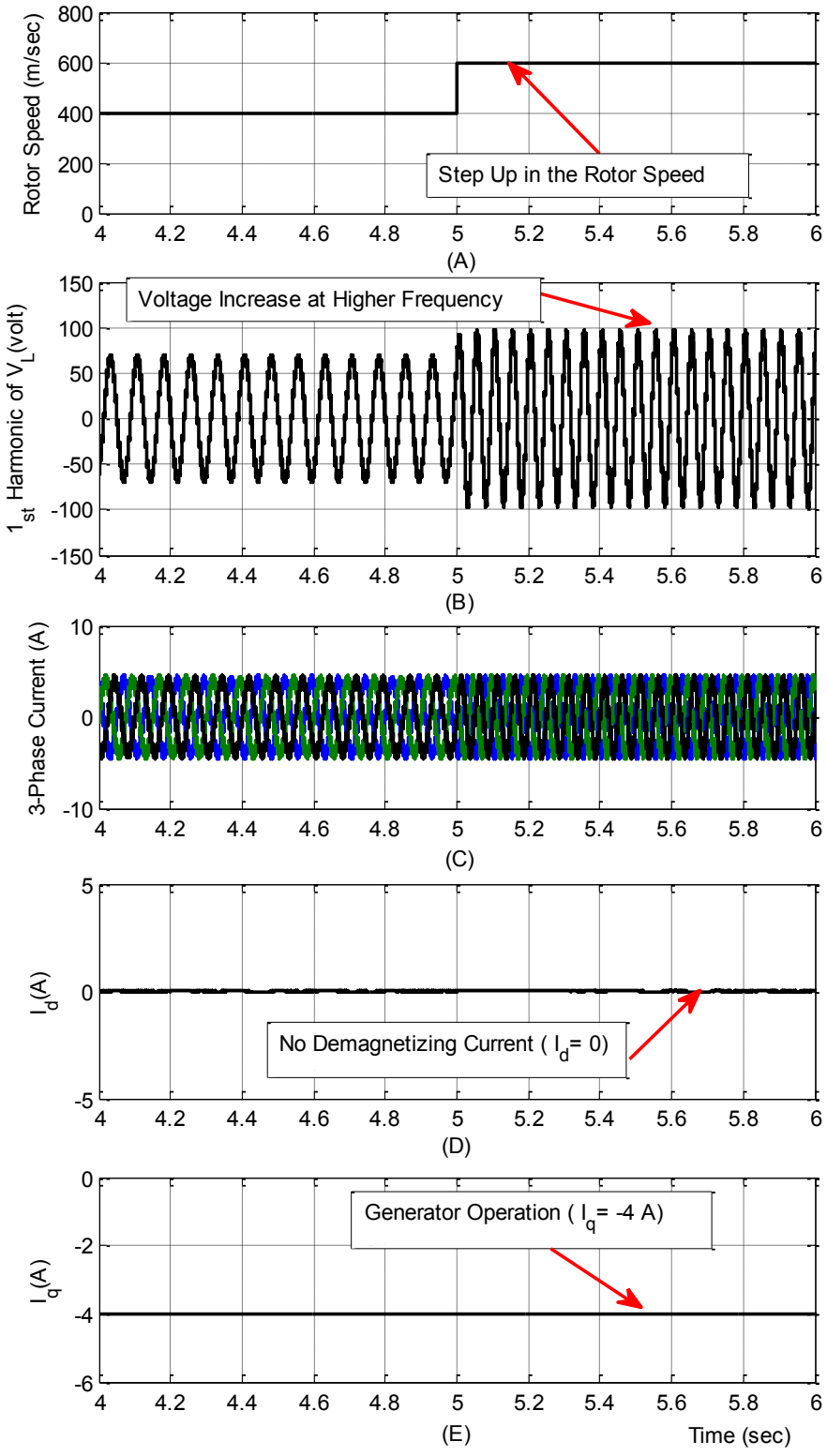

Fig. 3. 14: PMG Response to a Step Change in the Rotor Speed (400-600 rpm), without flux control ($i_d = 0$): (A) Rotor Speed. (B) 1st Harmonic of V_L. (C) 3-Phase Current. (D) D-axis Current Component. (E) Q-axis Current Component.

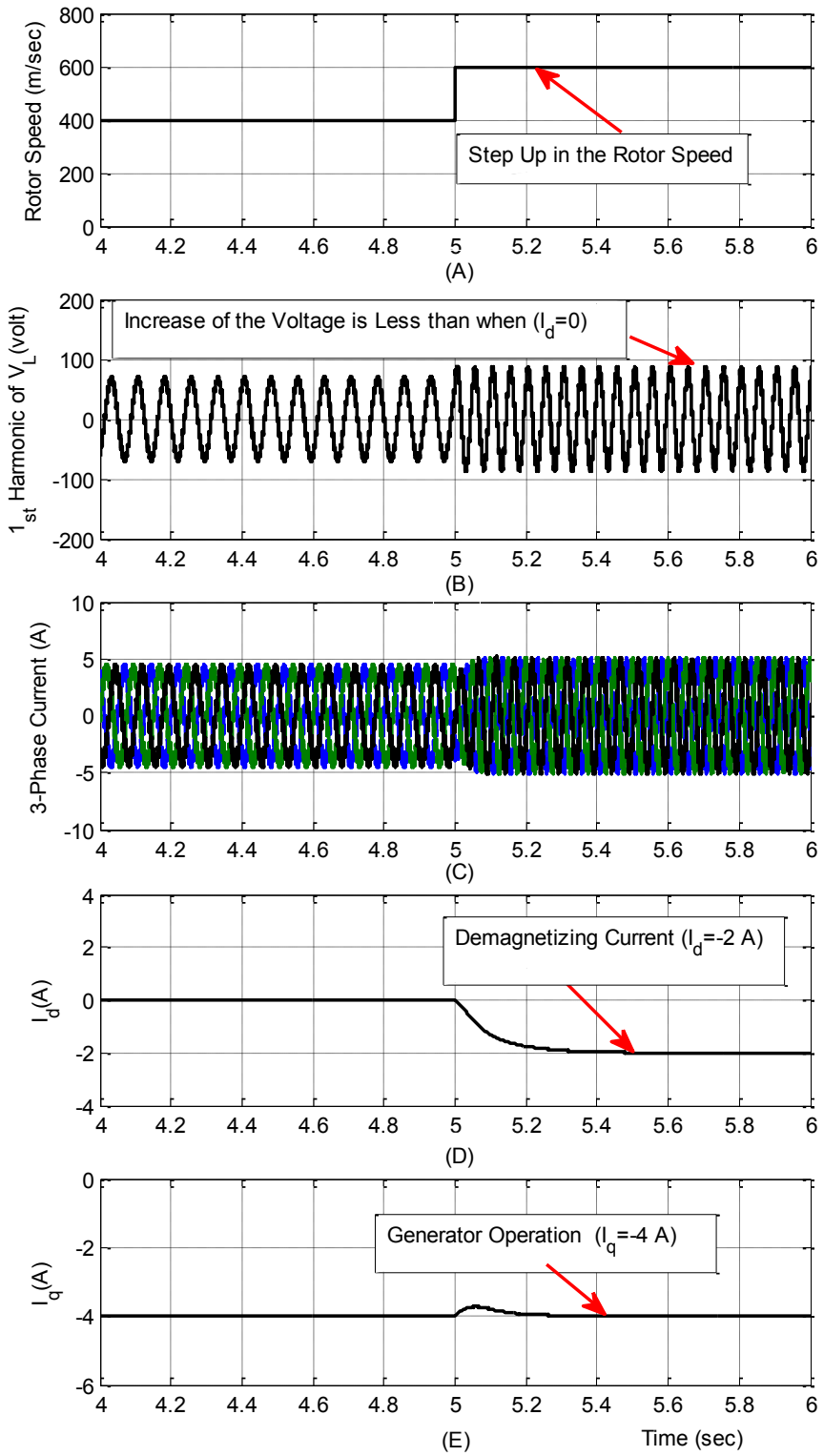

Fig. 3. 15: PMG Response to a Step up in the Rotor Speed (400-600 rpm), without flux control (i_d = -2 A): (A) Rotor Speed. (B) 1st Harmonic of V_L. (C) 3-Phase Current. (D) D-axis Current Component. (E) Q-axis Current Component.

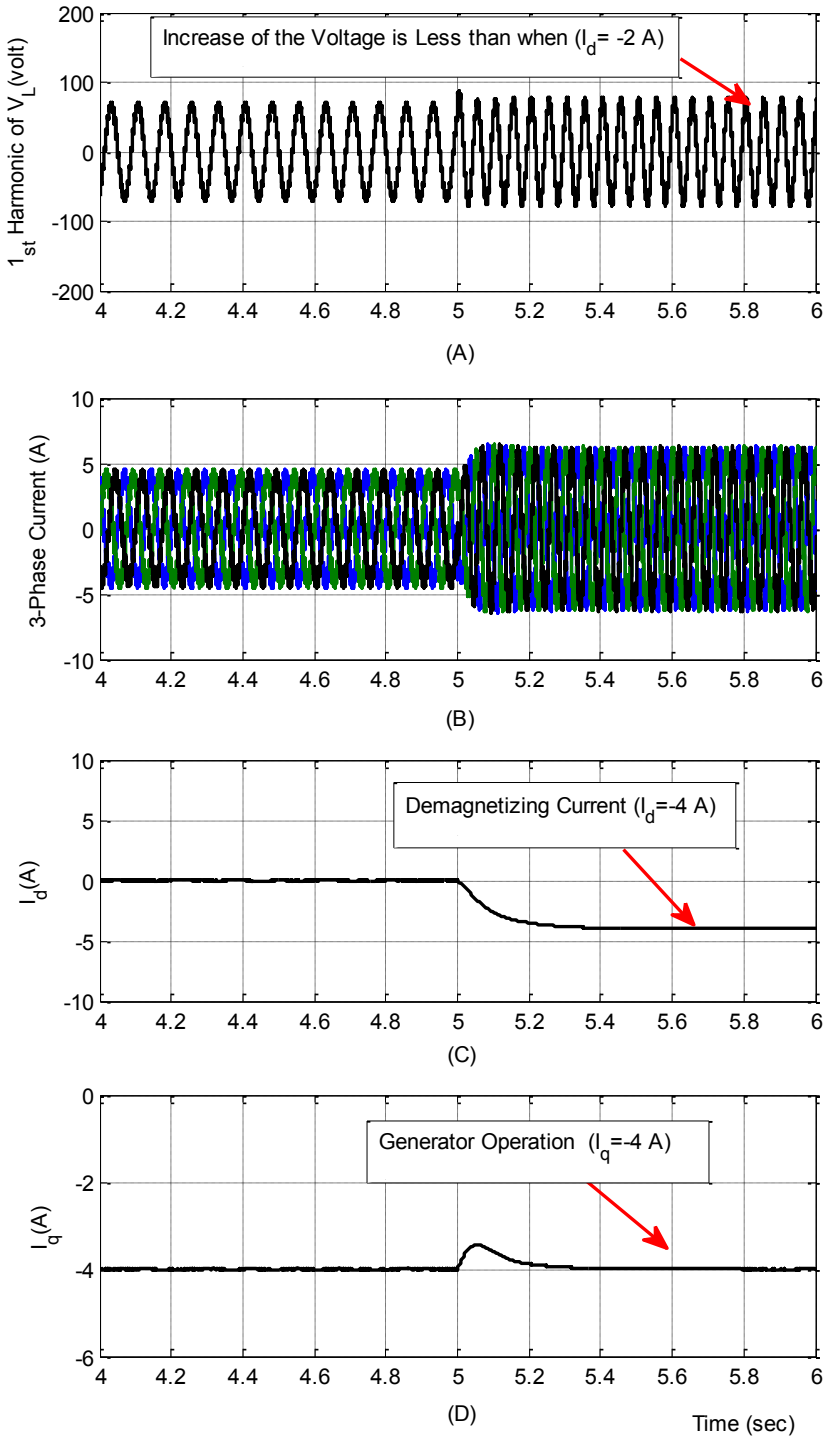

Fig. 3. 16: Response of the PMG to a Step up in the Rotor Speed (400-600 rpm), with a flux weakening control (i_d = -4A): (A) 1st Harmonic of V_L. (B) 3 Phase Current. (C) D-axis Current Component. (D) Q-axis Current Component.

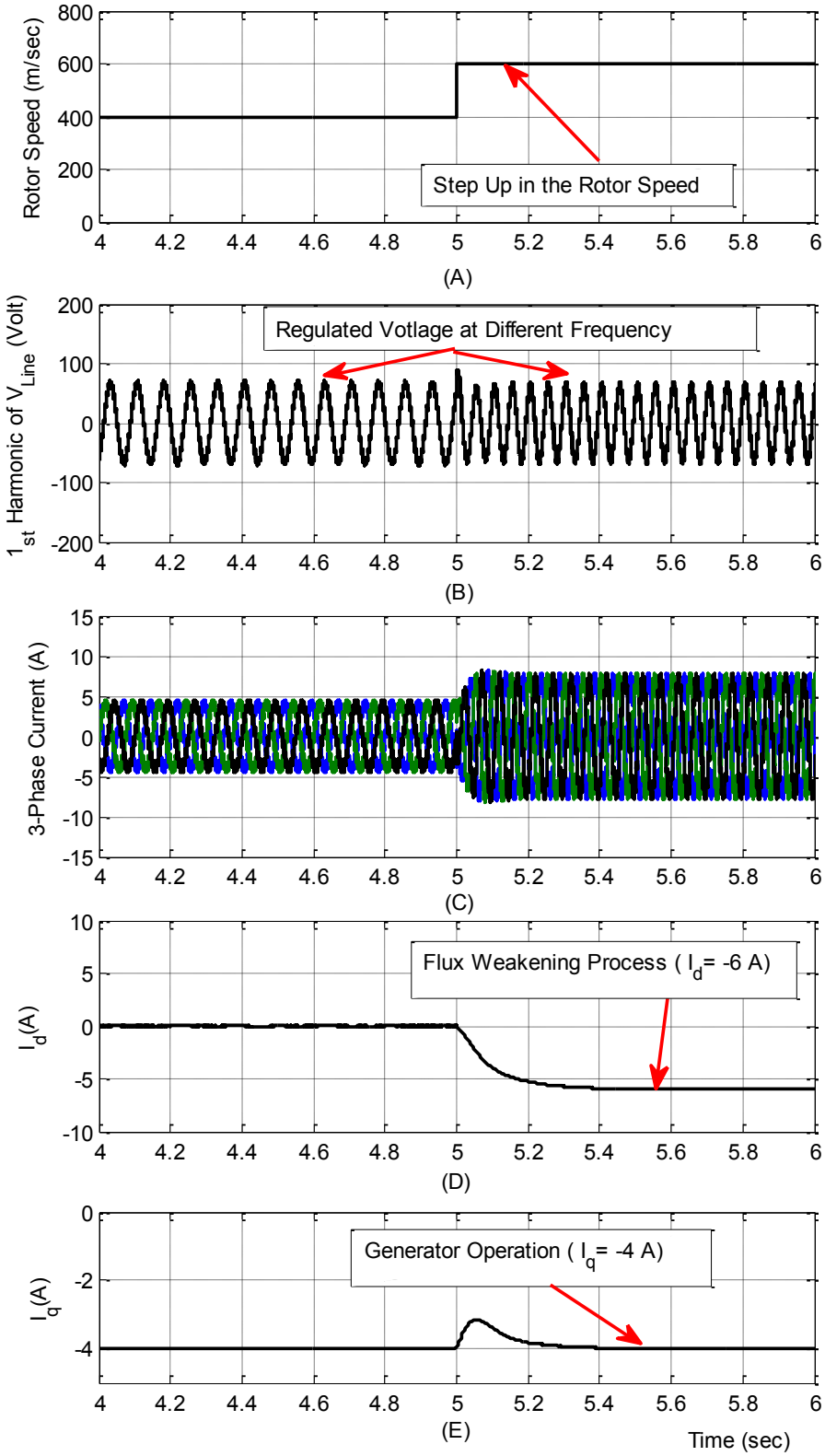

Fig. 3. 17: Response of the PMG to a Step up in the Rotor Speed (400-600 rpm), with a flux weakening control (i_d = -6A): (A) Rotor Speed. (B) 1st Harmonic of V_L. (C) 3 Phase Current. (D) D-axis Current Component. (E) Q-axis Current Component.

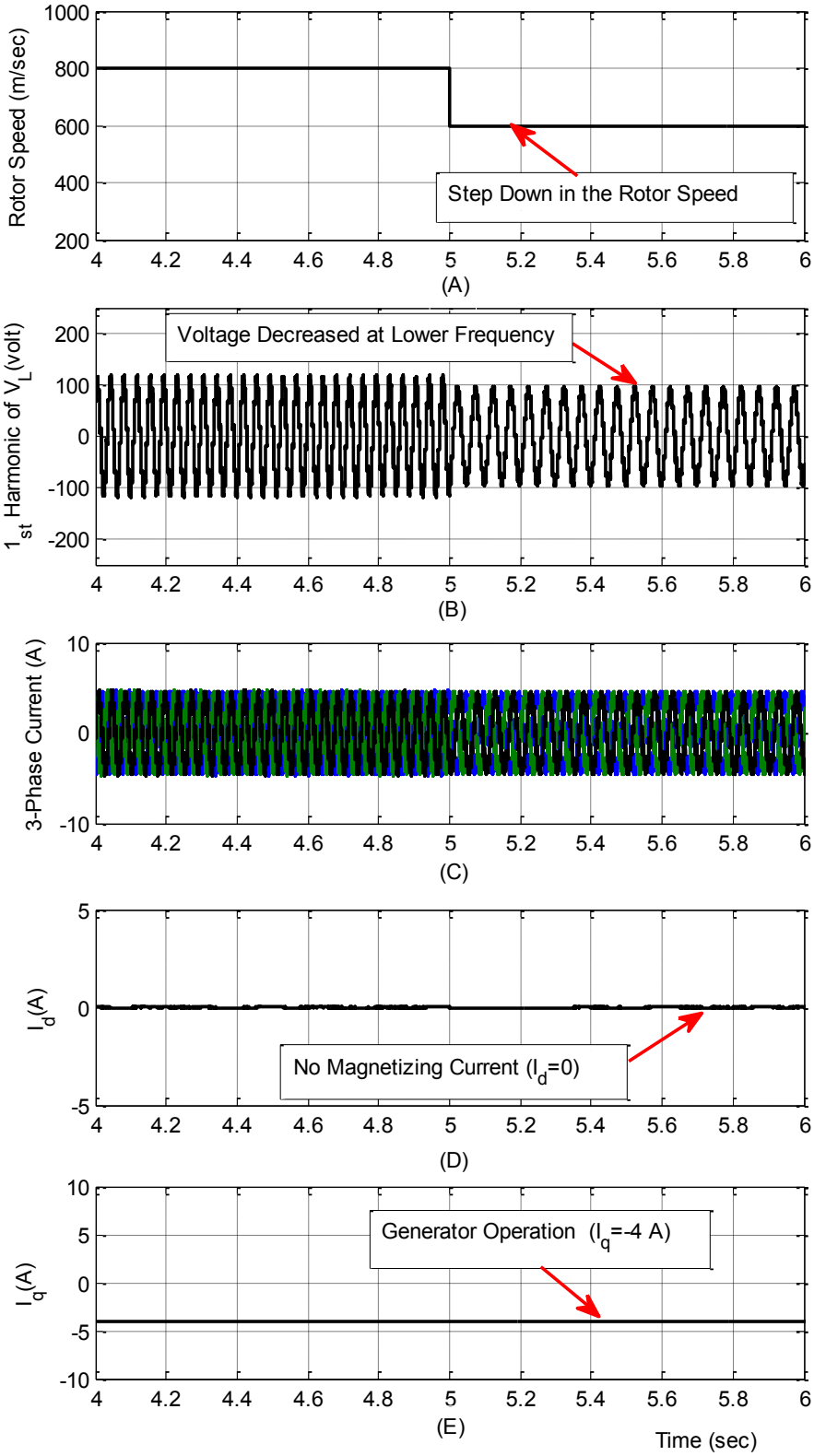

Fig. 3. 18: Response of the PMG to a Step down in the Rotor Speed (800-600 rpm), without flux control (i_d = 0): (A) Rotor Speed. (B) 1st Harmonic of V_L. (C) 3-Ph PMG Current. (D) D-axis Current Component. (E) Q-axis Current Component.

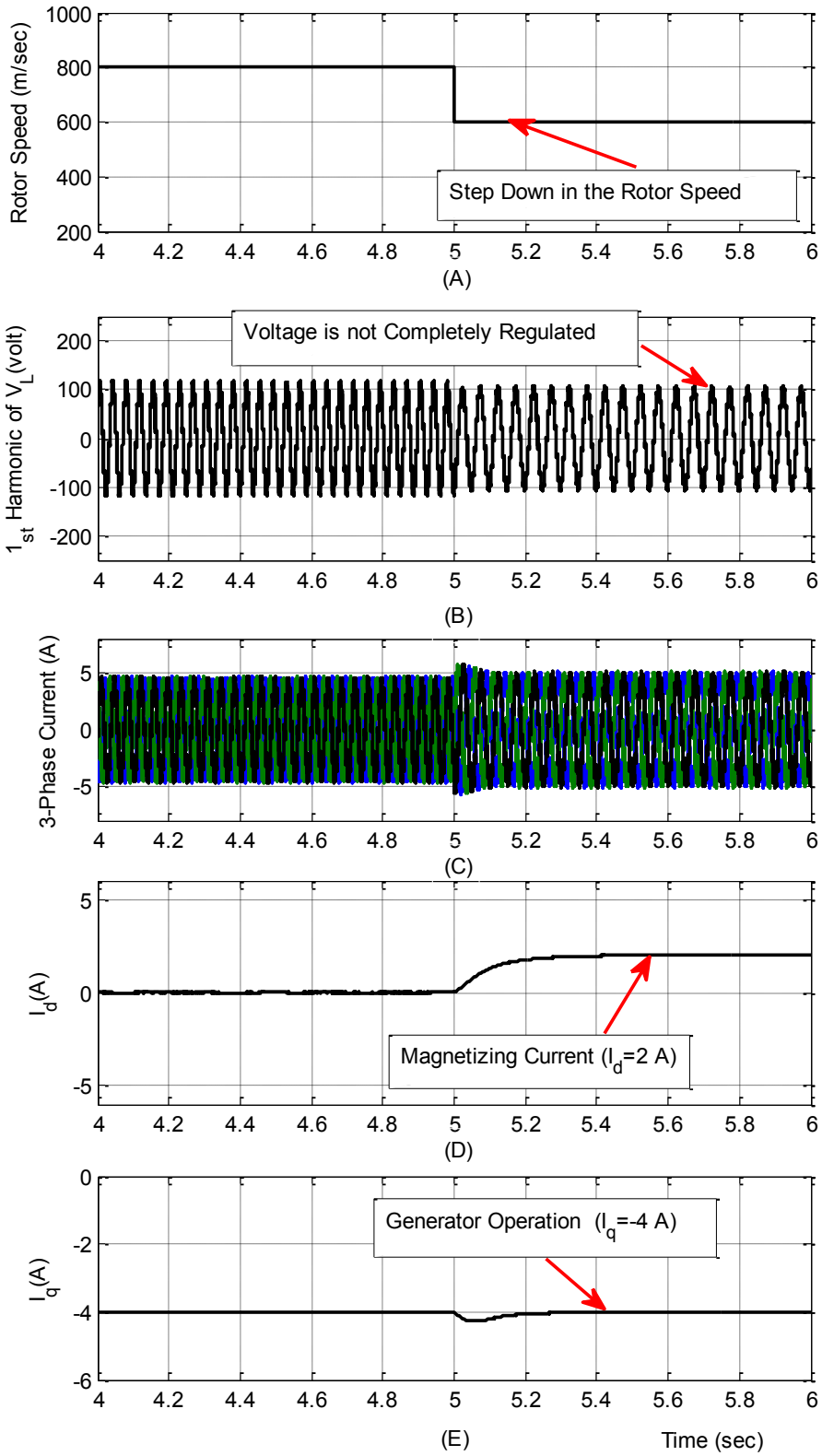

Fig. 3. 19: Response of the PMG to a Step down in the Rotor Speed (800-600 rpm), with a flux enhancing control (i_d = 2A): (A) Rotor Speed. (B) 1st Harmonic of V_L. (C) 3-Ph PMG Current. (D) D-axis Current Component. (E) Q-axis Current Component.

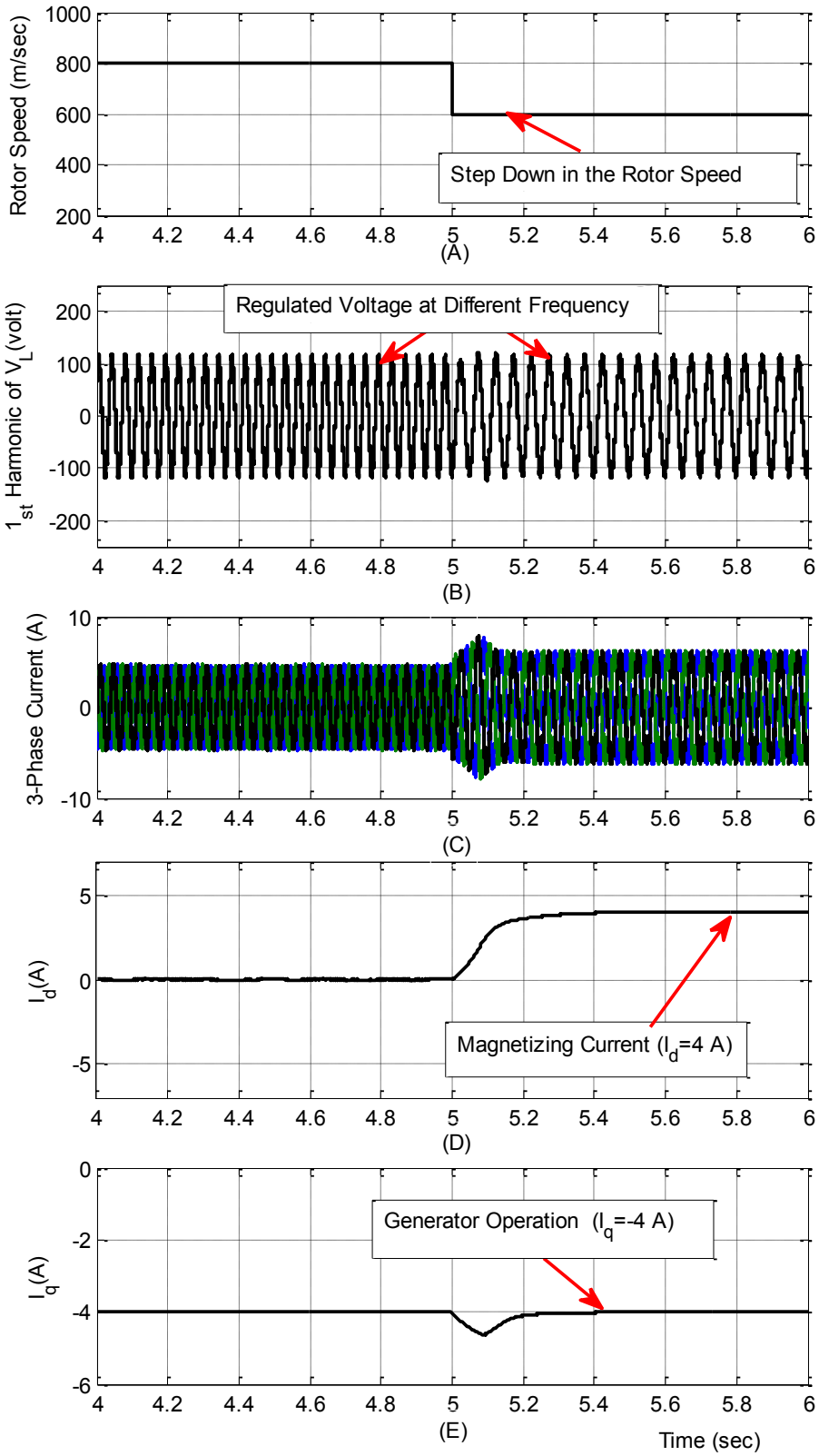

Fig. 3. 20: Response of the PMG to a Step down in the Rotor Speed (800-600 rpm), with a flux enhancing control (i_d = 4A): (A) Rotor Speed (B) 1st Harmonic of V_L. (C) 3-Ph PMG Current. (D) D-axis Current Component. (E) Q-axis Current Component.

3.6.2 Speed Range Extension for Field Weakening Operation

In order to test the effect of the flux weakening control on the performance of the system and the extension of the speed range of the PMG, several cases have been implemented at variable Q-axis reference current i_q^* and for several rotor speeds (2200, 1800, 1600, 1500, 1400, 1200, 1000, 800, 600) rpm. These cases are based on changing the D-axis reference current i_d^* as follows: i_d^*= (0, -2, -6 and -8)A. When the system is under control, all currents (i_q, i_d, i_a, i_b and i_c) are tracking their references.

For the first case, when $i_d^* = 0$, Fig. 3.21 shows that V_{dc} decreased and remained regulated with the reduction of i_q^* for a given rotor speed. For each rotor speed, there is always a minimum i_q^*.

This value is at the left end of each curve in Fig. 3.22. When i_q^* is below this minimum value, the real currents will not track their references and V_{dc} cannot decrease anymore and goes out of control. For example, when N=1500 rpm, the minimum i_q^*=3.6A and the minimum V_{dc} is 150 volt. Thus, if N > 1500 rpm volt a V_{dc} of 150v cannot be achieved.

For the second case when i_d^*= -4A , the minimum i_q^* value becomes smaller. This can be shown in the dashed-red lines in Fig. 3.22. For example, when N=1500 rpm the minimum i_q^* is 2A and the corresponding V_{dc} minimum is 120 volt. However, to obtain V_{dc} of 150 volt, the maximum operation speed is extended to approximately 1800 rpm. On the other hand, the maximum i_q^* is limited by the machine rating. This can be observed at the right end of each curve. Thus, the maximum DC output voltage is also limited.

Similarly for the third and the fourth cases, when i_d^*= -6A and i_d^*= -8A respectively, the minimum i_q^* value can decrease more and more for a given rotor speed as shown in Fig. 3.23 and Fig. 3.24. In other words, for a given V_{dc} the maximum operation speed for the PMG can be extended by running the machine in the field weakening region. This can be explained as follows: the flux-weakening operation (when applying - i_d) helps to limit the PMG output voltage even at high speed. From Figs. 3.21-3.24, it is clear that for obtaining a given V_{dc}=75 volt, the maximum operating speed is extended from 800 rpm at i_d = 0, to 1000 rpm at i_d = -4A , to 1200 rpm at i_d = -6A to 1400 rpm at i_d = -8A. Thus, the rotor speed has been extended by running the machine using flux weakening control.

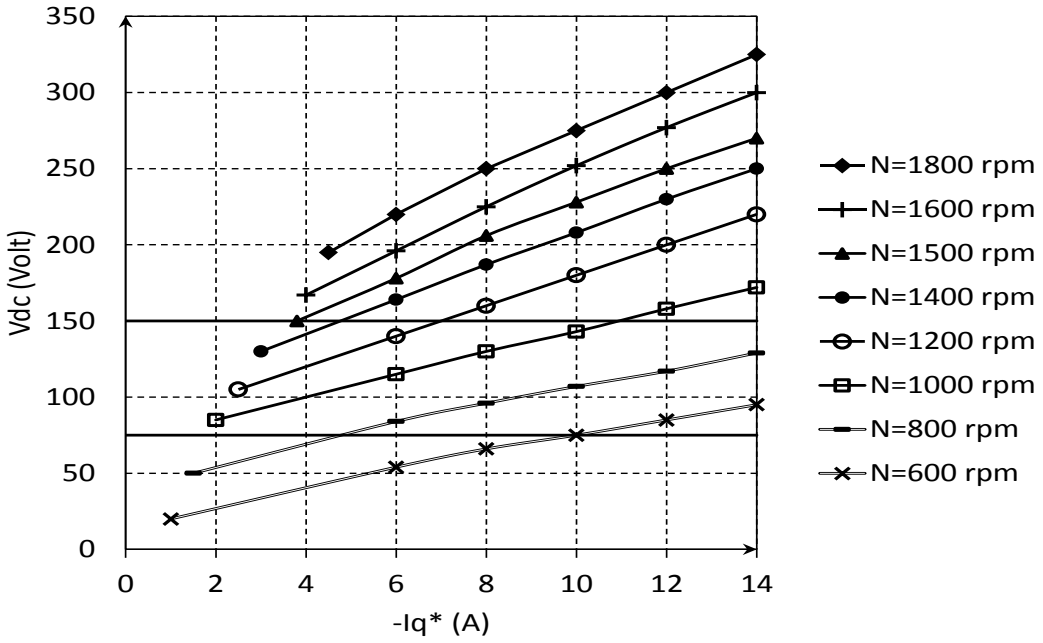

Fig. 3. 21: V_{dc} vs i_q^* when i_d^* = 0.

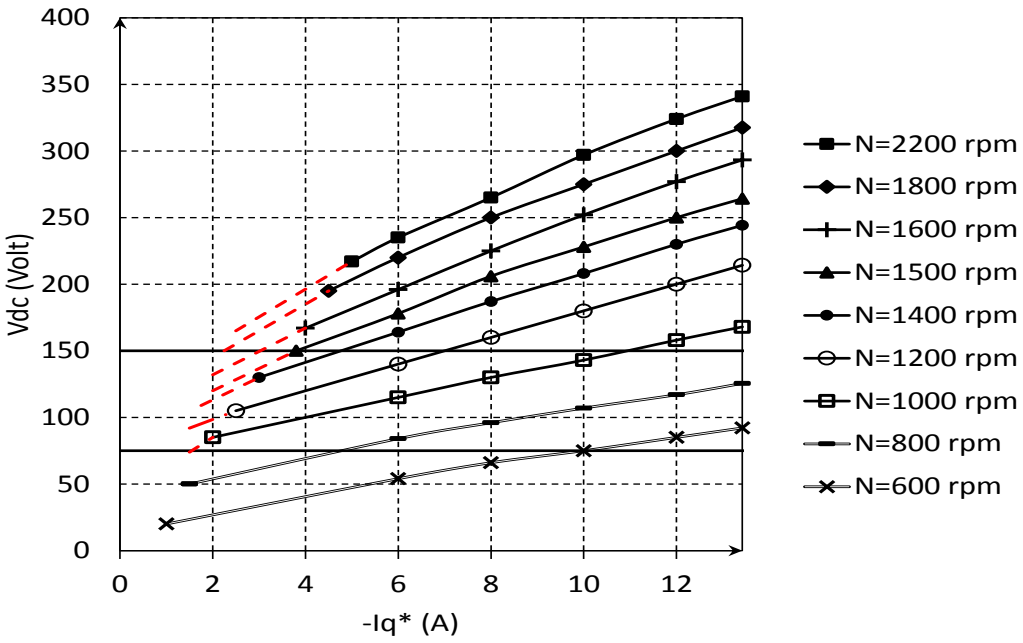

Fig. 3. 22: V_{dc} vs i_q^* when i_d^* = -4A.

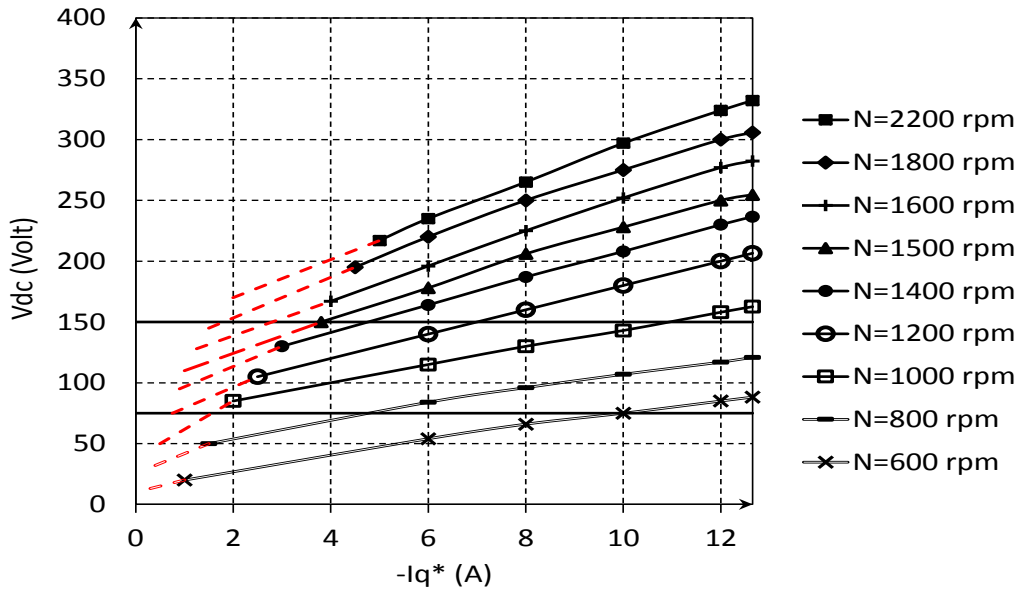

Fig. 3. 23: V_{dc} vs i_q* when i_d* = -6A.

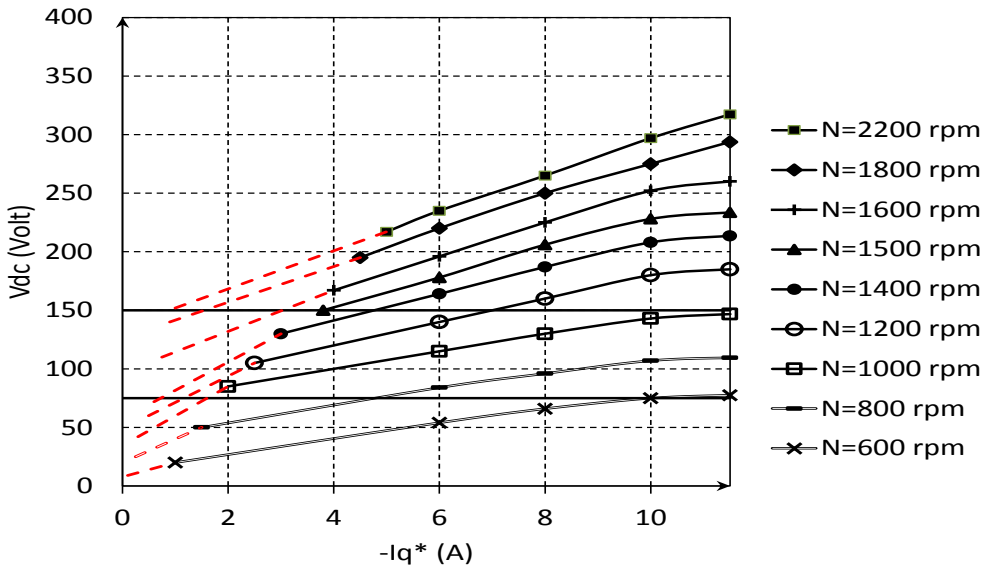

Fig. 3. 24: V_{dc} vs i_q^* when i_d^*= -8A.

3.7 Conclusion

This chapter has presented a new technique for controlling the flux of a PMG in a small wind turbine connected to a remote load. This technique provides an improvement in permanent magnet generator control, with the application to wind generators. Also it can be applied to PM generators fed from other renewable or conventional sources. The primary aim is to develop new ways for voltage regulation which up to now has not been done for these applications when fed with a PM generator. This technique was done based on injecting a negative or positive d-axis current to the stator coils of the PMG. Injecting d-axis current controls the flux of the machine either by weakening or strengthening the flux to regulate the output voltage of PMG. A case study was applied for small WECS. The results show how injecting different values of d-axis current can regulate the output voltage for variable speed operation.

The proposed control strategy was used to control the flux without any auxiliary coils or any special mechanical arrangements of the machine. However, injecting a d-axis current in the stator coils leads to higher losses and a reduction of the machine efficiency.

Flux weakening control for speed range extension purposes was proposed and analyzed in this chapter. If the PMG q-axis current (i_q) decreases at a given rotor speed, the DC voltage (V_{dc}) decreases. If i_q is beyond a minimum value, V_{dc} goes out of control and the 3-ph armature currents of the machine are distorted. Thus, the minimum V_{dc} or i_q is limited for a given rotor speed. On the other hand, for a given V_{dc}, the maximum operating rotor speed is limited. By applying a flux weakening d-axis current ($-i_d$), the PMG can provide lower V_{dc} for a given rotor speed. In other words, the PMG system can provide a given V_{dc} at higher rotor speed. Thus, the flux weakening extends the operational speed of the PMG. Therefore, through the simulation analysis, it is verified that flux weakening control is workable for the variable speed PMG system and significantly extends the operating speed range.

CHAPTER 4: REACTIVE POWER COMPENSATION CAPABILITY of a PERMANENT MAGNET SYNCHRONOUS GENERATOR for WECS APPLICATIONS

4.1 Introduction

Recently Small WECS units which are used to supply electricity to remote areas that are beyond the reach of an electric power grid or cannot be connected to a grid for economic reasons are of increasing interest [57][58]. Several electrical machines have been used to implement the electro-mechanical energy conversion system and its control. Each of them has their own advantages and disadvantages [58][59]. However, for a stand-alone power system in isolated and remote areas, the study of PMGs have been the subject of much research. The PMGs are interesting in low-power wind applications due to their high power densities and small sizes. The major benefit of using the PMG is the property of self-excitation, which permits operation at a high power factor and higher efficiency. Moreover, without the need to control the flux of the PMG, a diode rectifier can be used at the generator terminals, since no excitation current is required [61] [62].

Reactive power compensation capability of variable speed WECS is usually required for voltage regulation purposes. Also, it increases the active power limitation capability of the WECS [63][64]. In the literature, several methods have been used to control the reactive power of the WECS. The authors in [65] developed a new converter (matrix converter) for shunt reactive power compensation based PMSG. However, the high losses of the converter switches reduces the WECS efficiency. A new configuration of WECS for series compensation of the reactive power has been proposed in [66]. The proposed configuration is based on replacing the voltage source converter with a current source converter to remove the decoupling between the generator side converter and the grid side

converter. Therefore, a series compensation of the reactive power can be achieved using this configuration of the WECS.

In this chapter the reactive power compensation capability of the flux control has been studied for PMG based WECS applications. The compensation capability of the flux control has done by injecting d-axis current component for flux control. These current components are used not only to control the flux of the PMG but also to compensate the reactive power demanded by the three-phase inductive load which is directly connected to the PMG. Therefore, the aim of this chapter is to investigate the effect of the PMG flux control on the reactive power compensating capability for a variable inductive load.

The chapter is organized as follows: section 4.2 describes the Stand-alone wind energy conversion system. Section 4.3 describes the system controller based on HCC strategy. Section 4.4 discusses the reactive power calculations. Section 4.5 presents the experimental work of 5kw PMG case study and its results. Conclusions of the chapter are discussed in section 4.6.

4.2 Stand-Alone Wind Energy Conversion System

4.2.1 System Configuration

The proposed stand-alone WECS consists of a PMG connected to an active rectifier. A 3-phase variable inductive load is directly connected to the PMG. Fig. 4.1 shows the schematic diagram of the proposed autonomous WECS.

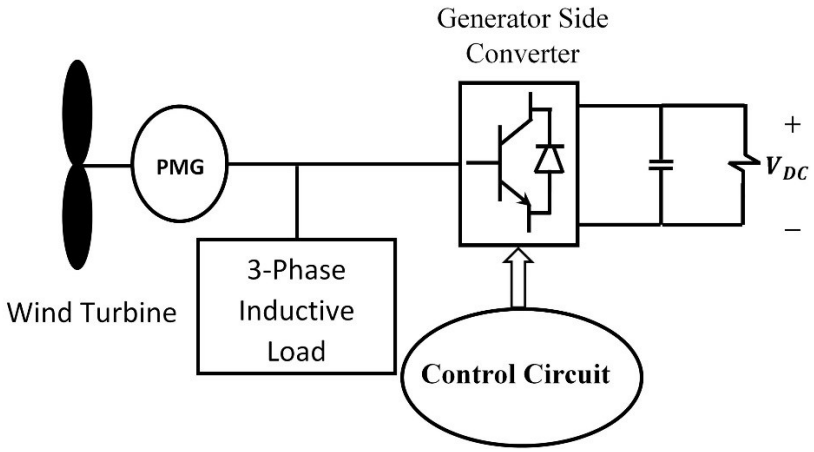

Fig. 4. 1: Schematic Diagram of the Proposed Autonomous WECS.

4.2.2 MPPT Operation and Model of the Wind Turbine

The wind power captured by a particular wind turbine (P_{Turb}) depends on its power coefficient (C_p) which is given by the relation [65]:

$$C_p = \frac{P_{Turb}}{P_w} \tag{4.1}$$

At a particular rotational speed, this power is maximized at a speed optimum value of the tip speed ratio λ_{opt}. This means that for each wind speed, there exists a specific point in the wind generator power characteristics where the output power is maximized. Therefore, the system can operate at the peak of the power-speed curve when the wind speed changes. Thus, the maximum power can be extracted continuously from the wind (MPPT control) [67][69].

The optimum power from the wind turbine can be written as follows:

$$P_{Turb\_opt} = 0.5\rho\pi R^2 C_{p\max} V_w^3 \tag{4.2}$$

Substitute (3.3) in (4.2), the obtained results can be expressed as function of λ_{opt}:

$$P_{Turb\_opt} = 0.5\rho\pi R^2 C_{p\max} \left(\frac{\omega_{wT} R}{\lambda_{opt}} \right)^3 \tag{4.3}$$

Where:

$C_{p\max}$ Power coefficient corresponding to λ_{opt}.

Rearrange (4.3), P_{Turb_opt} can be represented as follows:

$$P_{Turb\_opt} = K_{opt}(\omega_{wT})^3 \tag{4.4}$$

Where:

$$K_{opt} = \frac{0.5\rho\pi R^5 C_{p\max}}{\lambda_{opt}^3} \tag{4.5}$$

The torque developed by the wind turbine can be given by:

$$T_{Turb\_opt} = K_{opt}(\omega_{wT})^2 \tag{4.6}$$

The mechanical power generated by the wind turbine as a function of the rotor speed is shown in Fig. 4.2. The curve of the optimum power ($P_{Turb\text{-}opt}$) shows how the maximum power can be captured from the variation of the wind. Thus, the generator should work at optimum torque given by (4.6). Fig. 4.3 shows the block diagram for the wind turbine model, where the inputs are: the pitch angle of the blades and the wind speed. The optimum value of the tip-speed ratio is obtained using the information in Fig. 3.3.

The rotor speed, the power and the torque of the wind generator are calculated using (3.3), (4.3) and (4.6) respectively. These parameters are the inputs of the PMG control system.

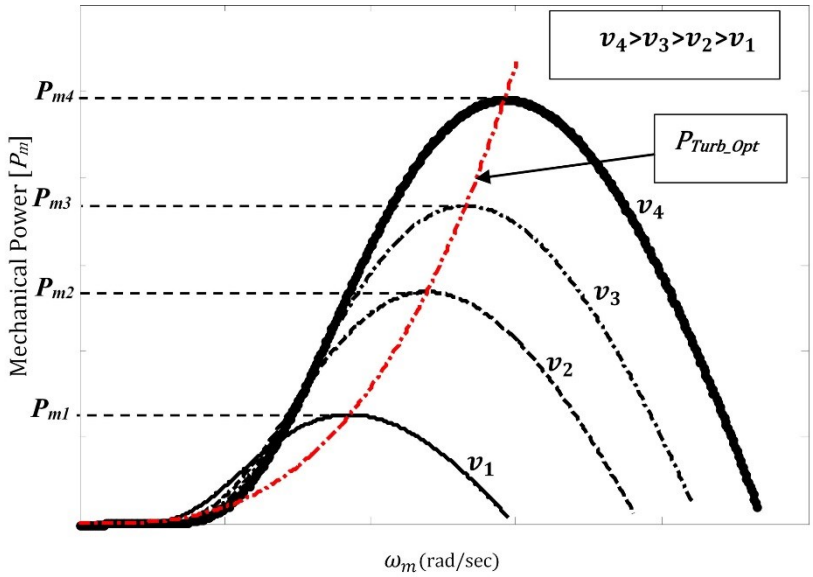

Fig. 4. 2: Optimum Power Curve at Different Wind Speed.

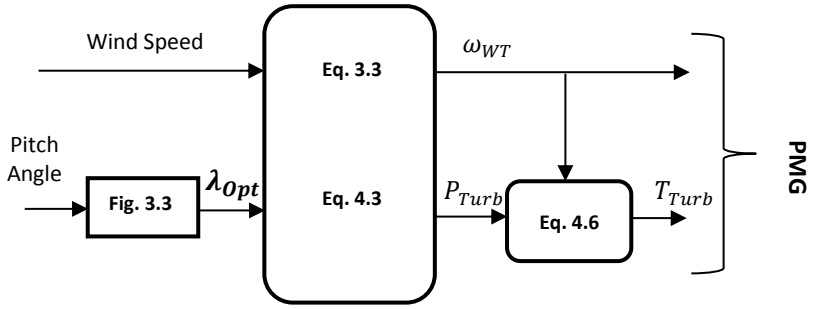

Fig. 4. 3: Diagram of Turbine Model.

4.3 System Controller

The proposed system configuration of the stand-alone WECS with its controller is illustrated in Fig. 4.4. The PMG rotor speed and its position are measured using an absolute encoder. The 3-ph armature currents i_a, i_b and i_c are obtained with ac current sensors, while the 3-ph voltages v_a, v_b and v_c are obtained with ac voltage sensors. The major part of the controller function is the implementation of the pulse generation of the

active rectifier. The reference current i_d^* is directly injected to the controller, while i_q^* is generated based on the MPPT operation of the wind turbine. The 3-ph armature current i_a, i_b and i_c as well as the rotor angle position θ are all fed into the controller module. In order to generate gate pulses for the active rectifier, HCC has been used and consequently the currents of the PMG are also injected to the controller. i_d^* is directly injected into the controller module to study its influence on the reactive power compensation capability.

The HCC is implemented inside the controller module. From $i_q^*$and i_d^* references current, the 3-ph armature current references i_a^*, i_b^* and i_c^* are obtained using the required frame transformation, d-q transformation. Then, the 3-ph armature currents are compared with the references to generate the gate signals of the active rectifier using HCC. Always, the upper and the lower switches of the active rectifier are on opposite status. Fig. 4.4 shows the schematic diagram of the controller module.

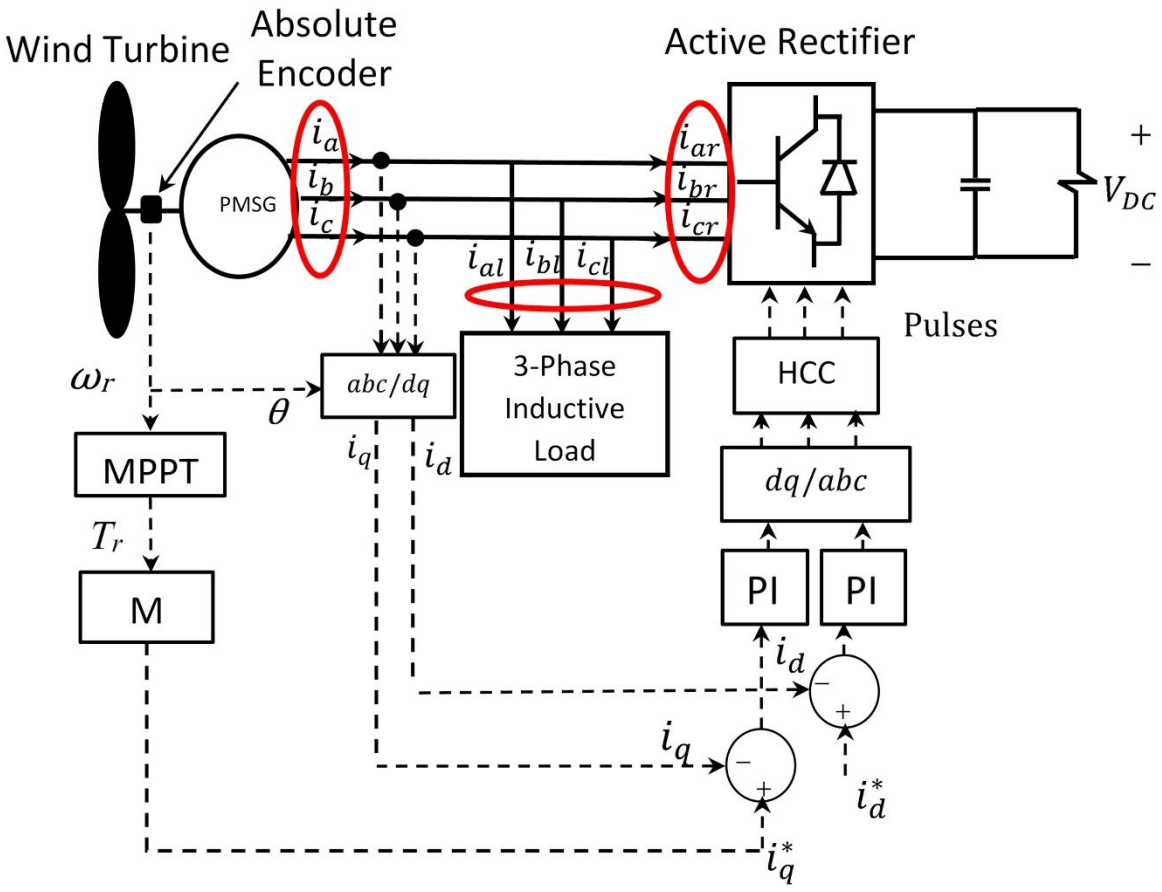

Fig. 4. 4: Schematic Diagram of the Controller Module.

4.4 Reactive Power Calculation

In order to study the effect of flux control on the reactive power of the system, the flow of the reactive power has been studied at different positions. These positons are shown in Fig. 4.4 with circles. The reactive power of the PMG is given by [69] [70]:

$$Q_{PMG} = \frac{3}{2}(v_d i_q - v_q i_d) \tag{4.7}$$

Where:

v_d, v_q D,Q-axis voltage of the PMG.

i_d, i_q D,Q-axis current of the PMG.

The reactive power consumed by the load (Q_L) and generated by the active rectifier (Q_r) are given respectively by:

$$Q_L = \frac{3}{2}(v_d i_{qL} - v_q i_{dL}) = \frac{v_L^2}{X_L} \tag{4.8}$$

$$Q_r = \frac{3}{2}(v_d i_{qr} - v_q i_{dr}) \tag{4.9}$$

Where:

i_{dl}, i_{ql}	d, q axis current of the load.
i_{dr}, i_{qr}	d, q axis current of the ac-side of the active rectifier.
L	Load Inductance.
f	System frequency.

4.5 Case Study and Results

A case study has been simulated using the proposed model of the WECS, where a three phase variable inductive load is directly connected to the PMG as shown in Fig. 4.1. The parameters of the system are shown in Table 3.1. Two different cases have been studied when the load inductance increases from L = 5 mH to L =10 mH while the load resistance is kept constant. The first case is based on running the PMG without flux control ($i_d = 0$), while the second case is based on running the PMG with flux control ($i_d \neq 0$). For each case the reactive power at the selected positions have been evaluated using (4.7), (4.8) and (4.9) respectively. For validation purposes, an experimental test was applied only for 10mH inductance load because of the difficulty of changing the load inductance while the system is running.

For the first case ($i_d = 0$), Fig. 4.5(A) shows that the load reactive power increases when the load inductance is doubled. This can be explained as follows: when the load inductance increases, the load reactance and the load voltage increase also as shown in Fig. 4.5(B) ($v_L = IX_L$; where X_L is the load reactance). Consequently, the load reactive power will increase according to (4.8). Fig. 4.6 shows the experimental results obtained for this case, L=10mH. By comparing Figs 4.5 and 4.6, it can be seen that the simulation prediction is quite close to the experimental results. However, high ripple appears in the measured line voltage - Fig. 4.6(B) - due to the commutation process in the free-wheeling diodes of the active rectifier. Fig. 4.7 shows that the generated reactive power on the ac side of the active rectifier is consumed by the load and the PMG. These results match well with the measured ones shown in Fig. 4.8.

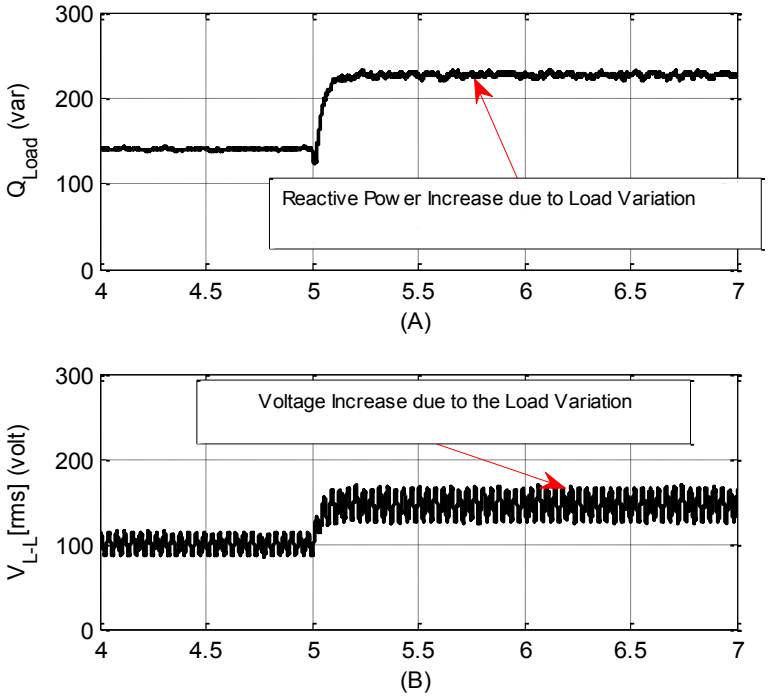

Fig. 4. 5: Operation of the System without Flux Control (i_d =0). (A) Load reactive power. (B) Line-Line voltage of the PMG.

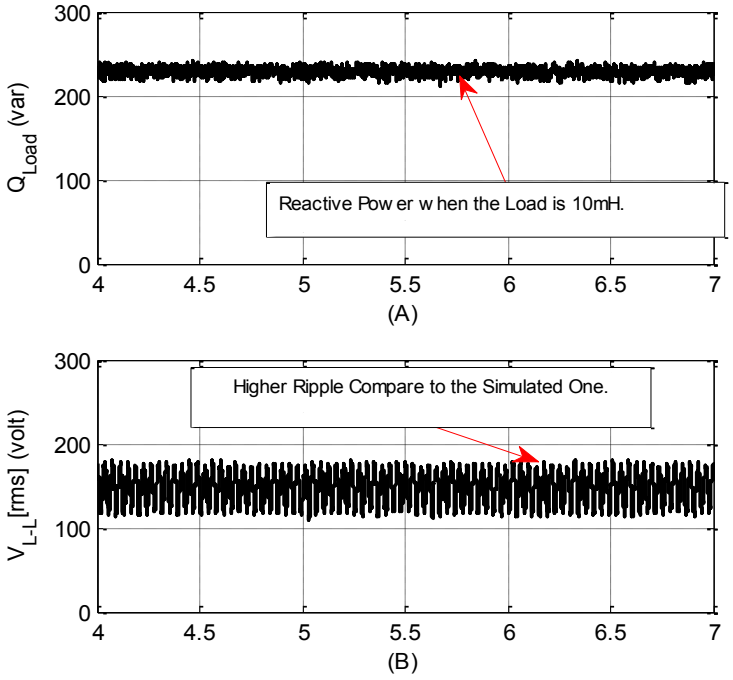

Fig. 4. 6: Experimental test for L= 10mH Operating without Flux Control. (A) Load Reactive Power. (B) Rms Line-Line Voltage of the PMG.

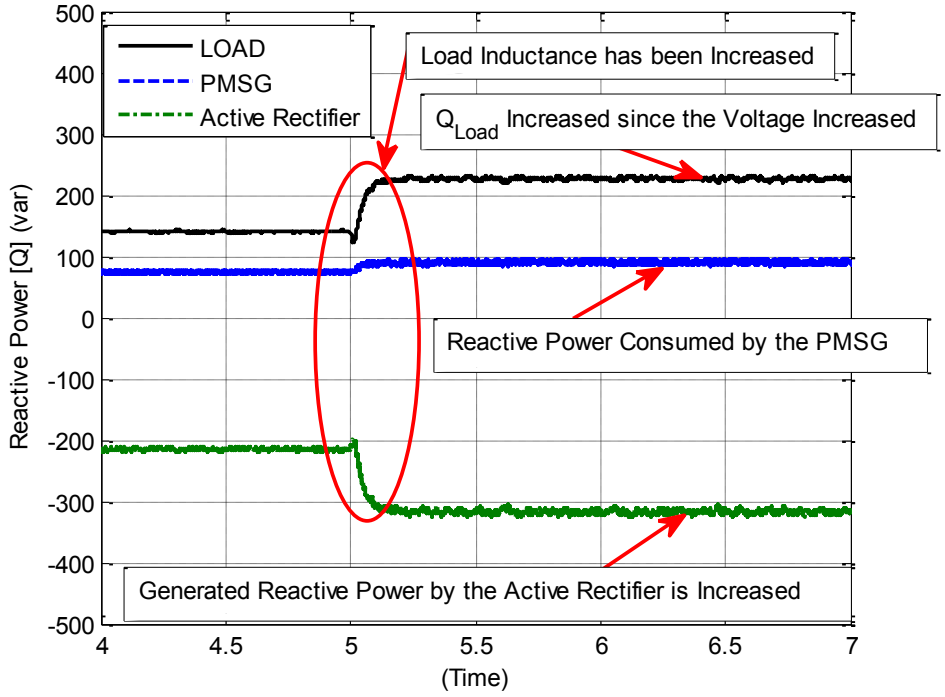

Fig. 4. 7: Reactive Power Flow for the Load, PMG and Active Rectifier when i_d =0.

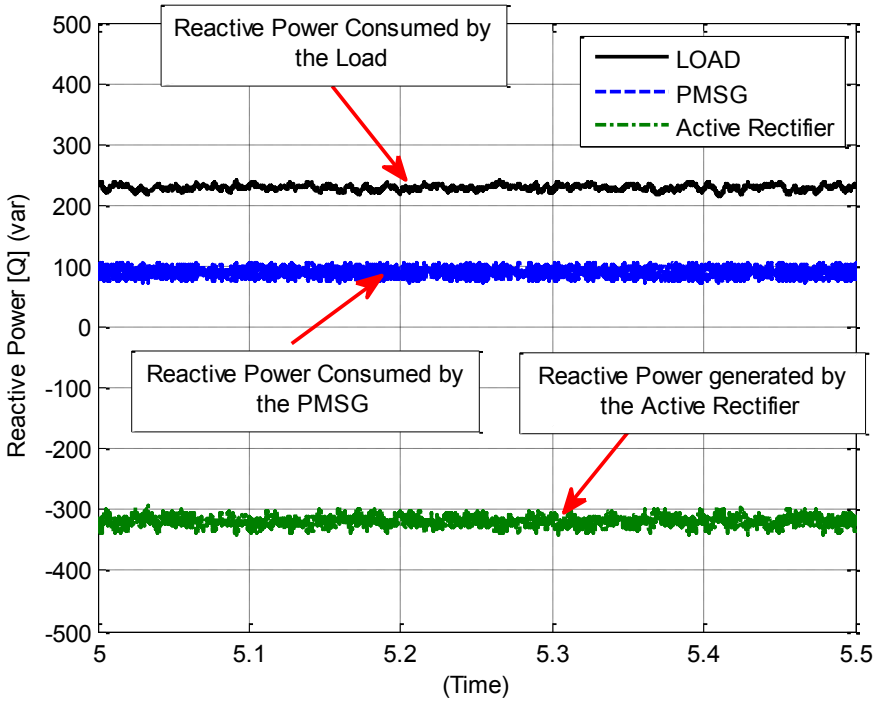

Fig. 4. 8: Reactive Power Flow Measured from the Experimental Setup when the System is Operating without Flux Control (i_d = 0, L=10 mH).

In the second case, when the PMG operates with flux control, three scenarios have been studied based on injecting several values of d-axis currents (i_d = -2, -3 and -5) Amps.

For i_d = -2A, Fig. 4.9(B) shows that the load reactive power is increased when the load inductance is doubled. However, this increase in the reactive power is less than that in the previous case when (i_d = 0). The reduction in the reactive power in this scenario can be explained as follows:

When the PMG is operating with flux control (i_d = -2A), the flux of the PMG is reduced and the terminal voltage is reduced too. Consequently, the reactive power consumed by the load reduces according to (4.8). Fig. 4.10 shows the experimental results obtained for this case, when L=10mH. By comparing Figs 4.9 and 4.10, it can be seen that the simulation prediction is quite close to the experimental results. However, as with the previous case, a high ripple appears in the measured line voltage - Fig. 4.10(B) - due to the commutation process in the free-wheeling diodes of the active rectifier as previously discussed.

Fig. 4.11 shows that the generated reactive power on the ac side of the active rectifier is consumed by the load and the PMG. However, the reactive power consumed by the PMG is less than the previous case when i_d = 0, because the flux control starts compensating the reactive power consumed by the PMG. These results match well with the measured ones shown in Fig. 4.12.

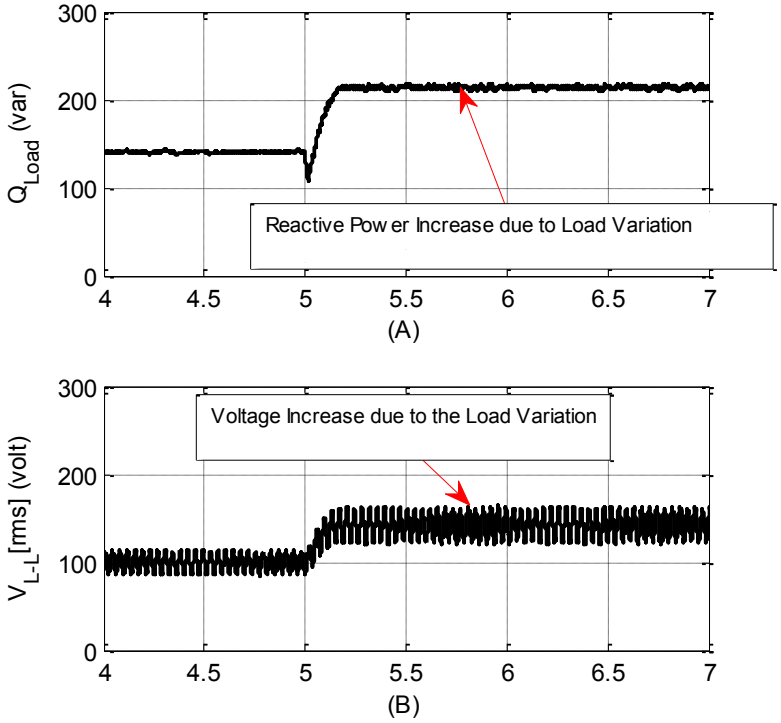

Fig. 4. 9: Operation of the PMG with Flux Control (i_d =-2A). (A) Load Reactive Power. (B) Line-Line Voltage of the PMG.

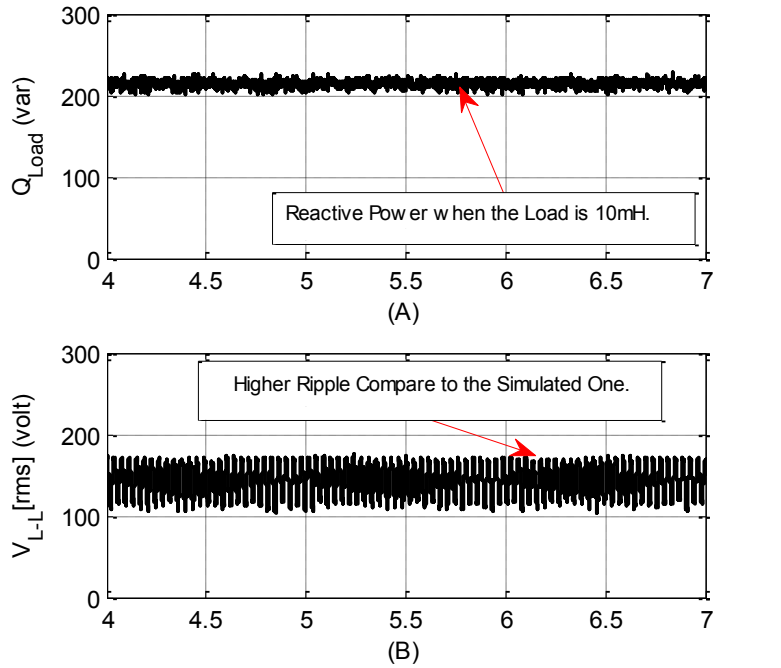

Fig. 4. 10: Experimental test for L= 10mH operating with flux control (i_d = -2A). (A) Load reactive power. (B) Rms Line-Line voltage of the PMG.

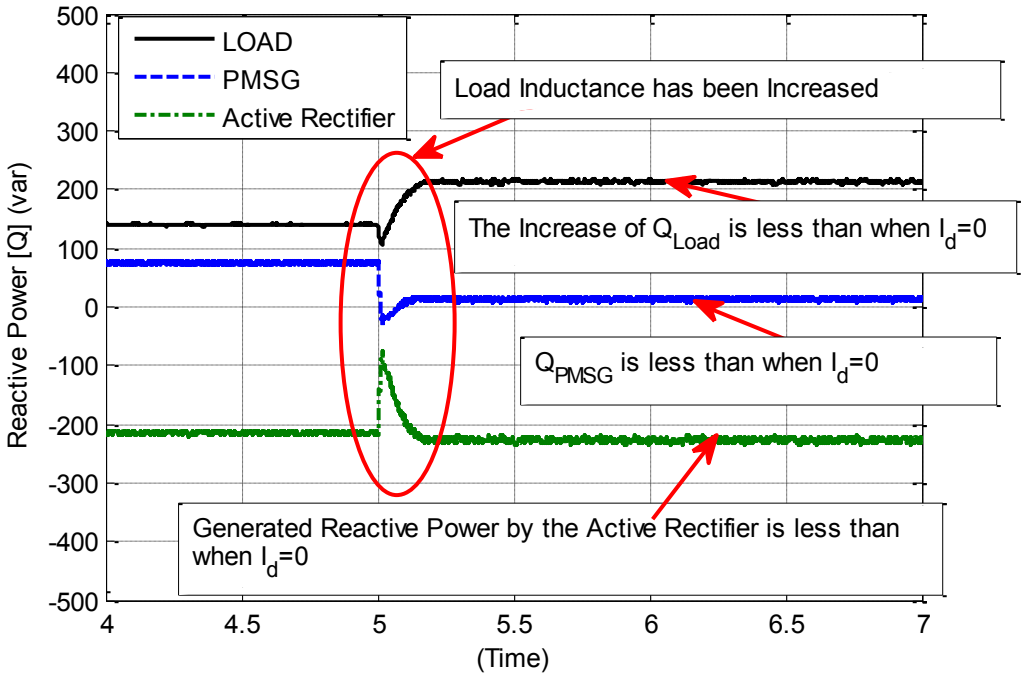

Fig. 4. 11: Reactive power flow for the load, PMG and active rectifier when i_d = -2A.

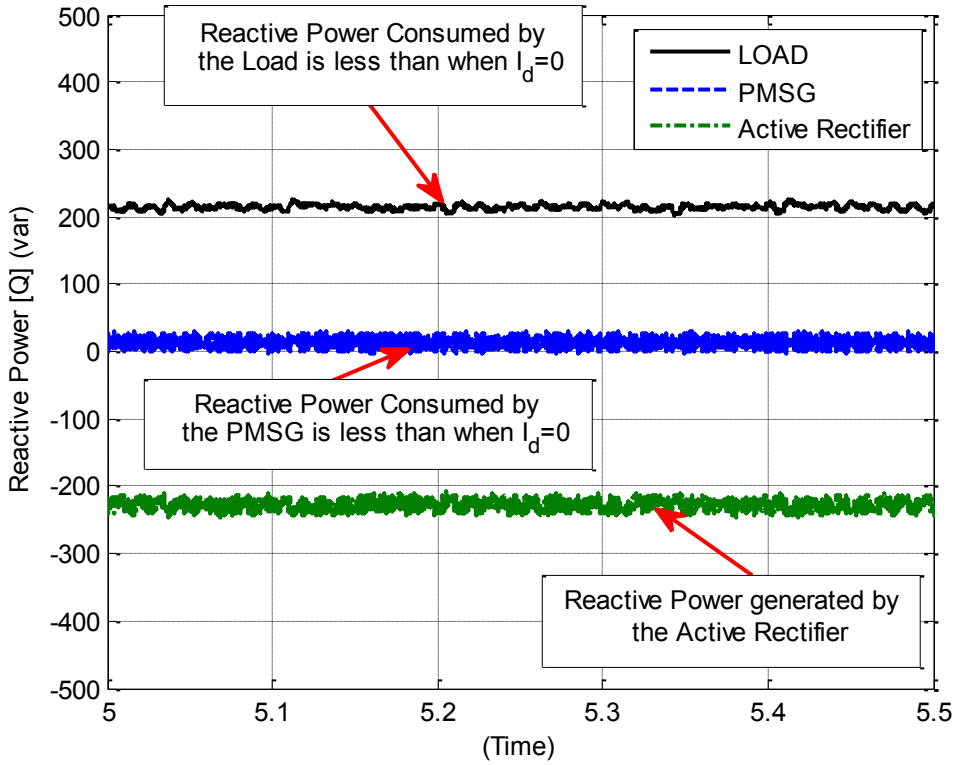

Fig. 4. 12: Reactive power flow measured from the experimental setup when the system is operating with flux control (i_d = -2A, L=10 mH).

For i_d =-3A, Fig. 4.13 (B) shows that the load reactive power increases when the load inductance changes from 5mH to 10mH. However this increase of reactive power is less than the previous scenario when i_d = -2A. Fig. 4.14 shows the experimental results obtained for this case, when L=10mH. It is clear that these results match with the simulation ones shown in Fig. 4.13. Fig. 4.15 shows that the generated reactive power on the ac side of the active rectifier is consumed by the load and the PMG. These results match well with the measured ones shown in Fig. 4.16.

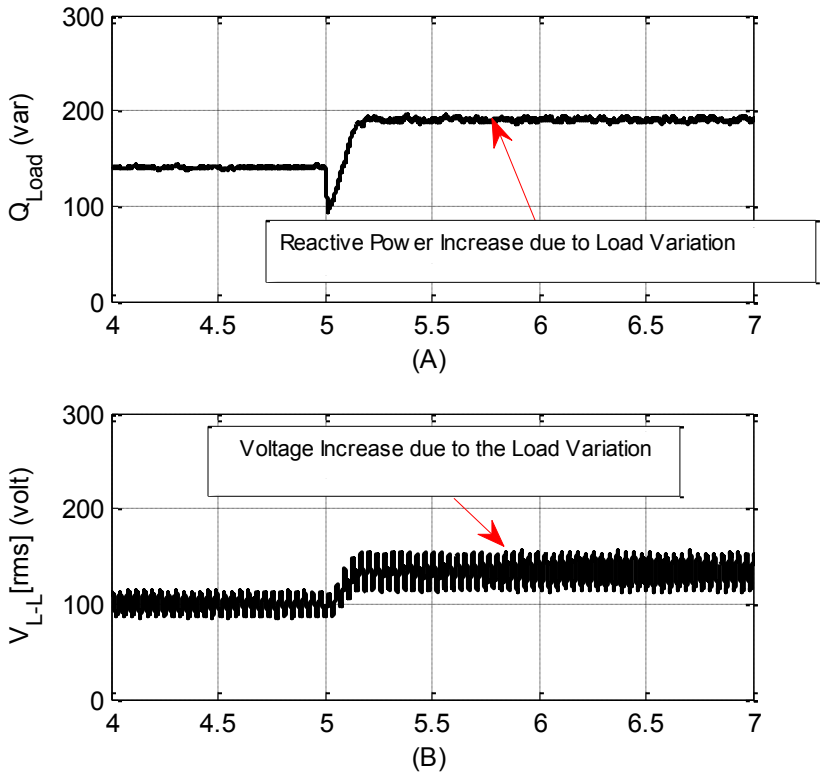

Fig. 4. 13: Operation of the PMG with flux control (i_d =-3A). (A) Load reactive power. (B) Line-Line voltage of the PMG.

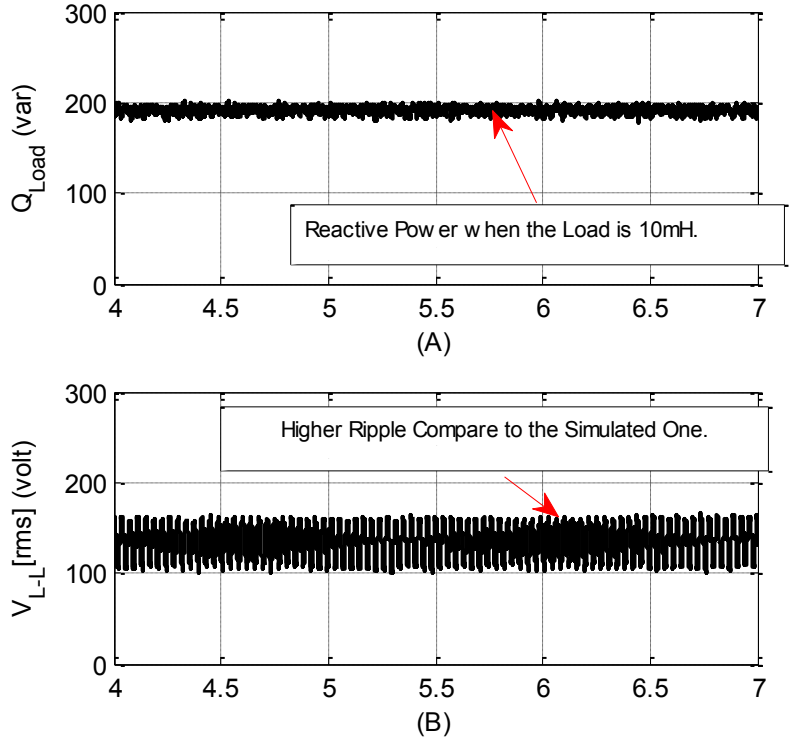

Fig. 4. 14: Experimental test for L= 10mH operating with flux control (i_d= -3A). (A) Load reactive power. (B) Rms Line-Line voltage of the PMG.

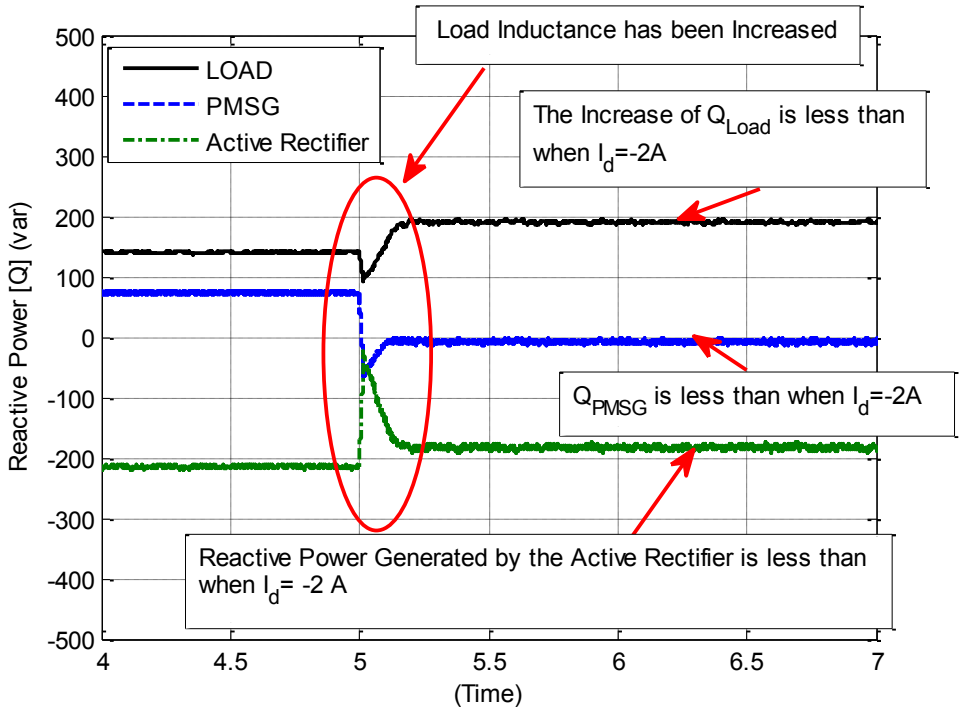

Fig. 4. 15: Reactive power flow for the load, PMG and active rectifier when i_d = -3A.

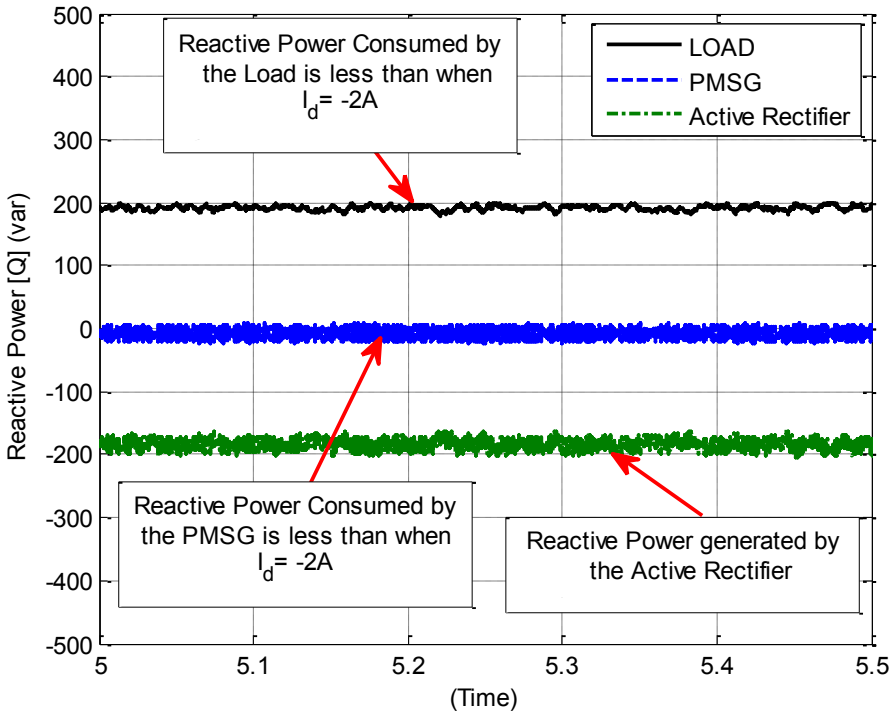

Fig. 4. 16: Reactive power flow measured from the experimental setup when the system is operating with flux control (i_d = -3A, L=10 mH).

Finally for the third scenario when i_d =-5A, Fig. 4.17(B) shows that the line voltage has been regulated when the load inductance changes from 5mH to 10mH. Also the reactive power is decreased when the load is doubled. This decreased in the reactive power is explained because of the compensation capability of the flux control. Fig. 4.18 shows the experimental results obtained for this case, when L=10mH. The total reactive power generated by the active rectifier is reduced compared to the previous scenarios when i_d =-2A, -3A which is clearly shown in Fig. 4.19. These results match well with the measured ones shown in Fig. 4.20. In this scenario, the PMG shares responsibility for generating the reactive power which is consumed by the load with the active rectifier. This means that controlling the flux of the PMG by injecting different values of the D-axis currents can be used for reactive power compensation capability.

The flow of the reactive power in the system for all cases and scenarios are shown schematically in Figs. 4.21-4.24.

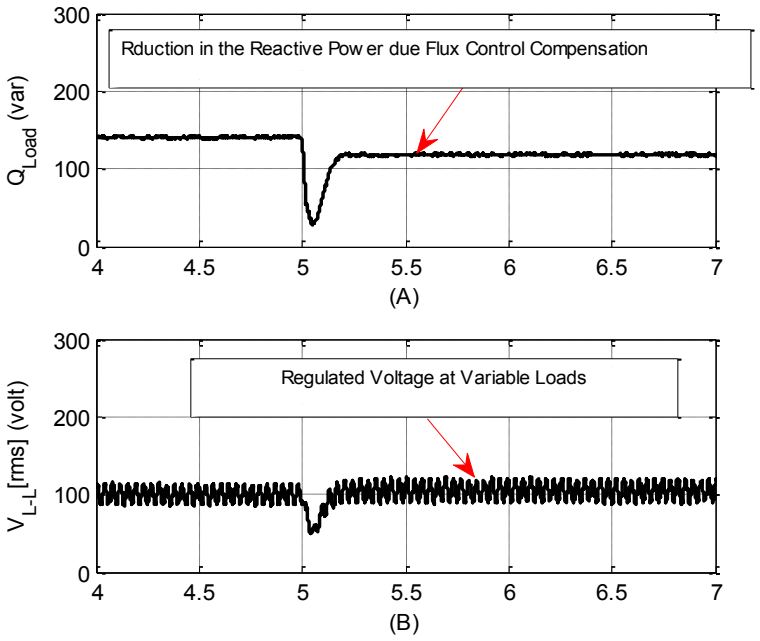

Fig. 4. 17: Operation of the PMG with Flux Control (i_d =-5A). (A) Load Reactive Power. (B) Line-Line Voltage of the PMG.

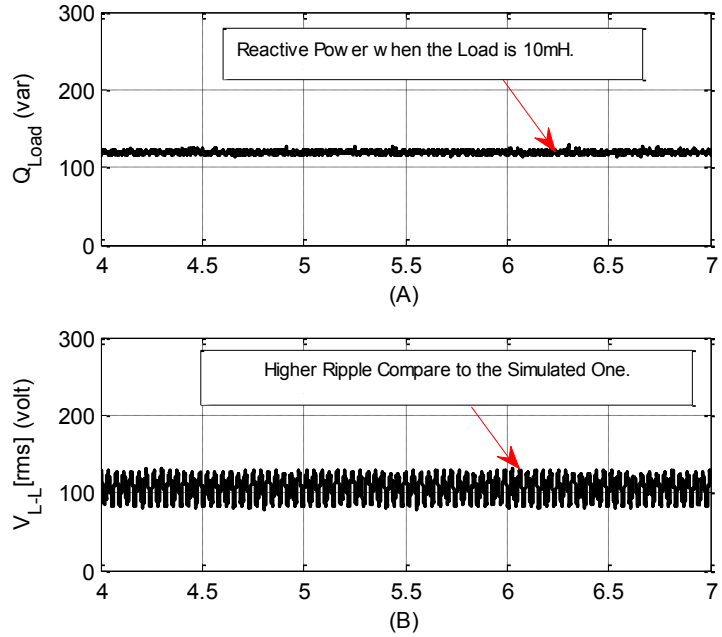

Fig. 4. 18: Experimental test for L= 10mH operating with flux control (i_d = -5A). (A) Load reactive power. (B) Rms Line-Line voltage of the PMG.

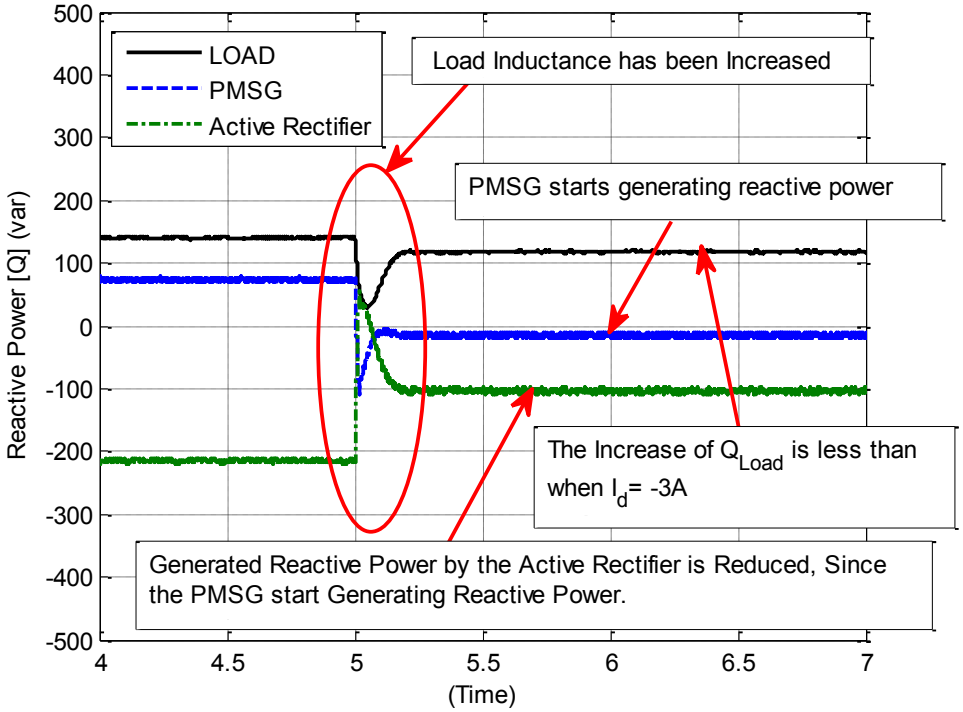

Fig. 4. 19: Reactive power flow for the load, PMG and active rectifier when i_d = -5A.

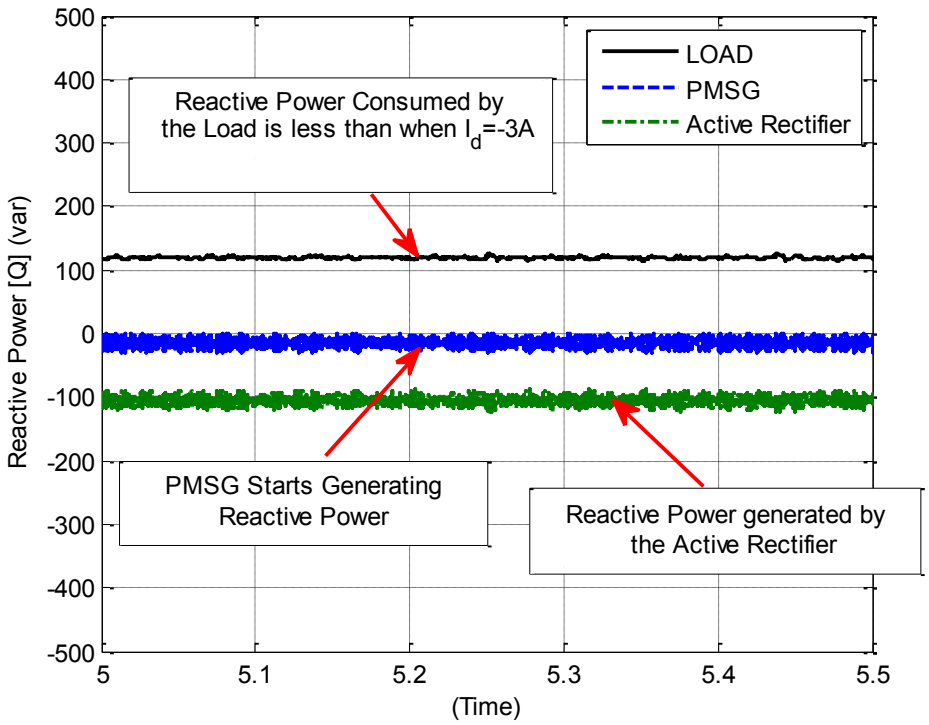

Fig. 4. 20: Reactive Power Flow Measured from the Experimental Setup when the System is Operating with Flux Control (i_d = -5A, L=10 mH).

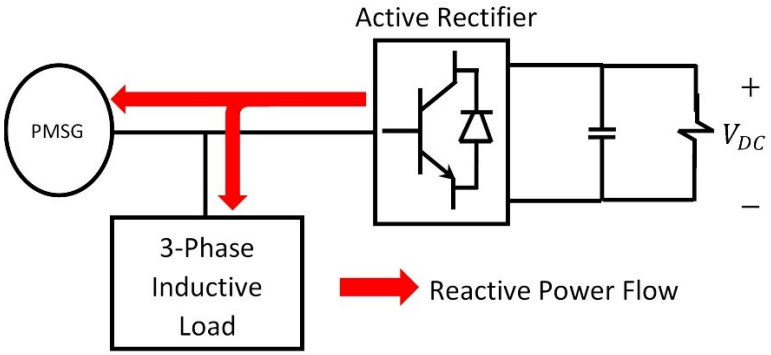

Fig. 4. 21: Schematic of the reactive power flow in the system when $i_d = 0$.

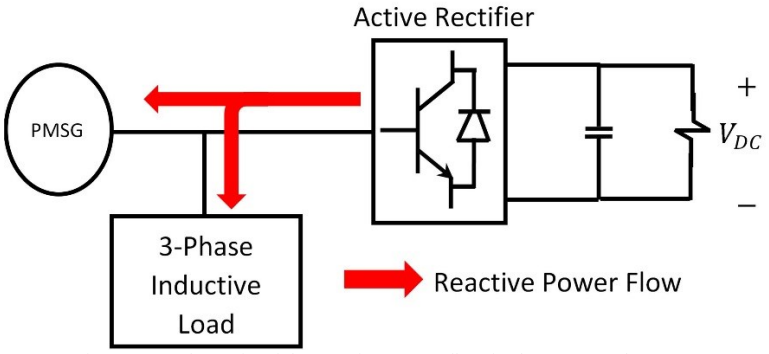

Fig. 4. 22: Schematic of the reactive power flow in the system when i_d = -2A.

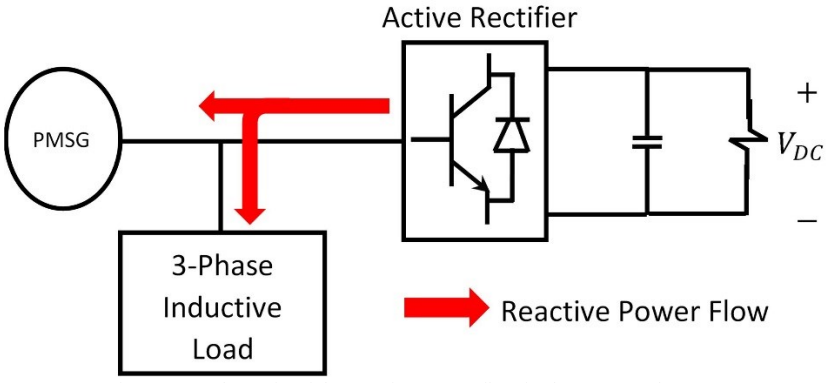

Fig. 4. 23: Schematic of the reactive power flow in the system when i_d = -3A.

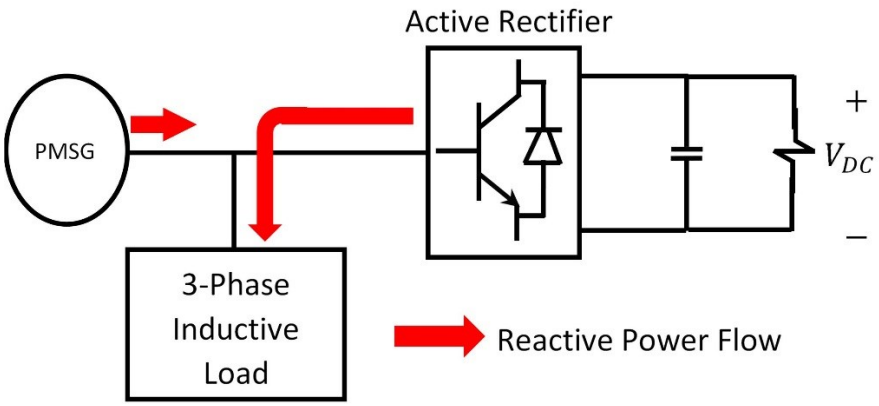

Fig. 4. 24: Schematic of the reactive power flow in the system when i_d = -5A.

4.6 Conclusion

This chapter discussed the capability of PMG flux controller in reactive power compensation for a variable consumer load in a stand-alone WECS. The controller shows effective response during steady state and transient. The proposed WECS based active rectifier was used to inject several values of D-axis current components. By injecting such current components, the load voltage was regulated for a variable inductive load. In addition, the reactive power consumed by the load was compensated using the flux control operation of the system. Without using the flux controller, the PMG consumes reactive power. Once the flux controller of the PMG was used, the reactive power consumption by the PMG was compensated and reduced gradually. Then, the PMG starts generating reactive power to the load.

CHAPTER 5: VARIABLE FLUX MACHINE (VFM) OPERATION and CONTROL

5.1 Introduction

Controlling the flux of the PMG is required for wind generators applications in order to protect the WECS from high voltages at high wind speed. Different types of VFM are proposed in the literature which mainly can be classified into two major categories. The first category is based on modifying the construction of the PMG by installing additional excitation coils in the stator or in the rotor to control the airgap flux of the machine [71-74]. However, such configurations lead to an additional cost and extra size of the machine and might not be appropriate for small industrial applications. The second category is based on using several alternatives of low coercive permanent magnets. The authors in [75] present a variable flux machine of Samarium-Cobalt PMs. However, the large magnetizing current of these magnets leads to increase the rating of the coupled converter. In order to overcome this problem, the authors in [76] proposed another configuration of variable flux machine using AlNiCo PMs which reduce the magnetizing current of magnet. Therefore, the rating of the coupled converter is also reduced compared to the previous type. Another advantage of using the AlNiCo PMs is the high efficiency of the machine itself [76], since the magnetizing and the demagnetizing process of this machine can be done using a small period pulses with negligible losses.

This chapter is organized as follows: section 5.2 describes the characteristics of the AlNico PM and its properties. Section 5.3 discusses the variable flux machine and its operation.

Section 5.4 presents the controller of the variable flux machine and finally experimental setup and its results in sections 5.5 and 5.6 prior to concluding these results in section 5.7.

5.2 AlNiCo PM Operation and Characteristics

When the PM-VFM is running at no-load, the magnet operating point occurs at the intersection between the airgap line and the demagnetization curve of the magnet in the 2nd quadrant of the AlNiCo magnet hysteresis loop which is at point (A) in Fig. 5.1. It is clear from Fig. 5.2 that the AlNiCo magnet can retain the intrinsic flux density (B_r) up to a certain limit when it is exposed to an external demagnetization field (H_a).

In Fig. 5.1, the initial operating point of the AlNiCo magnet is point (A). When an external demagnetization field is applied, the operating point of the AlNiCo magnet is moving from point (A) to point (B) which lies below the demagnetization curve knee of the hysteresis loop. Once the magnet operating point shits beyond the knee point, the intrinsic magnetic flux density will be reduced by ΔB_i as shown in Fig. 5.2. When the demagnetizing field is released, the magnet operating point moves along a line parallel to the original demagnetization curve to an operating point of a lower flux density point (C). At this point, the new remnant flux density will be B_r-ΔB_i as shown in Fig. 5.2. When the external demagnetization field reached a specific value of (H_d), the AlNiCo magnet will be completely demagnetized.

In order to re-magnetize the magnet, a magnetizing field (H_m) has to be applied to move the operating point of the magnet beyond the knee point in the first quadrant of the hysteresis loop until the saturation flux density (B_s) is reached as shown in Fig. 5.1.

When the magnetization field is released, the magnet recoils along the demagnetization curve to the airgap line and the flux density of the magnet will be (B_r). It is also clear from Fig. 5.1 that the field require to magnetize the field (H_m) is greater than the demagnetizing field (H_d).

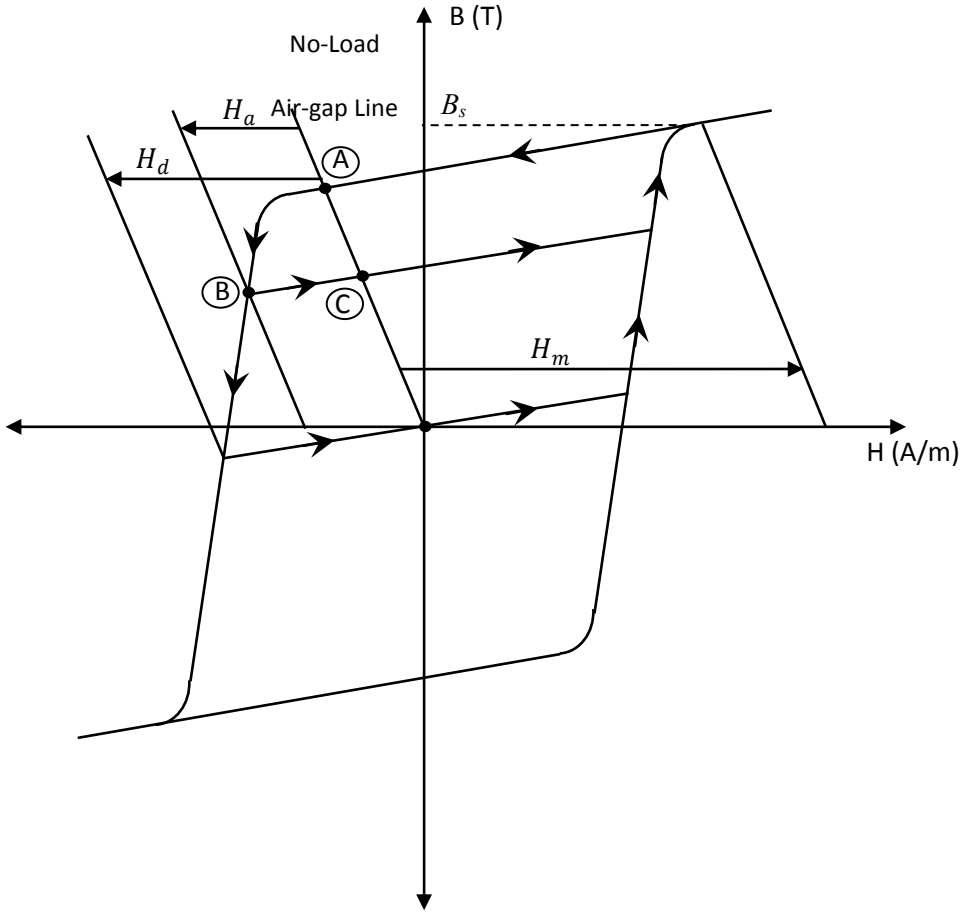

Fig. 5. 1: Illustration of the Operation of Low Coercive Field Magnets under Magnetizing and Demagnetizing Fields.

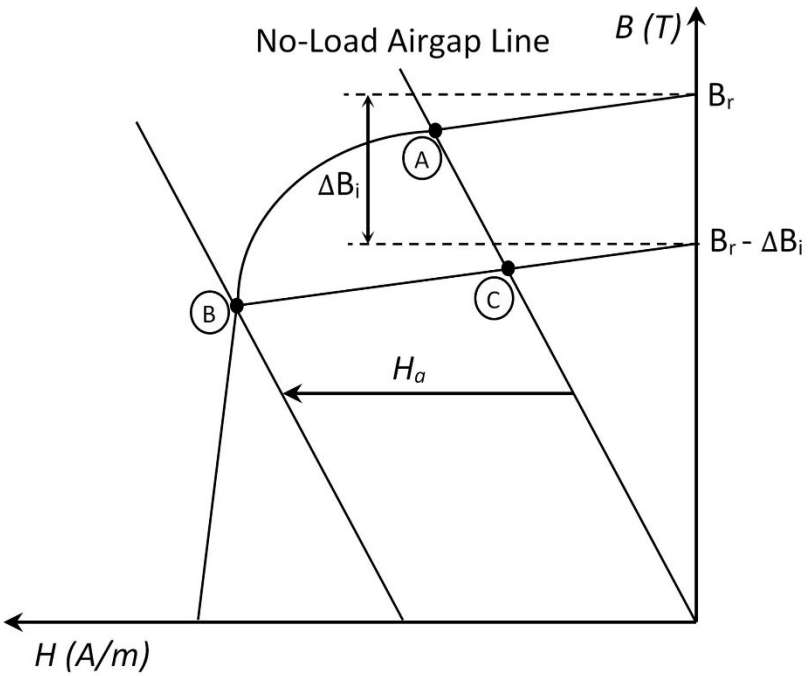

Fig. 5. 2: AlNiCo Magnets under Demagnetization Field.

5.3 Properties of the Variable Flux Machine (VFM)

There are several advantages of using the low coercive force of PM, such as the AlNiCo, which can be summarized as follows:

1. By using the AlNiCo PMs the converter size will be smaller as compared to a machine that uses rare earth PMs since the current requirements for magnetization are lower [77].
2. The AlNiCo PMs have high thermal resistivity and have good mechanical features.

Fig. 5.3 shows the rotor geometry design and the prototyped rotor of the variable flux machine with AlNiCo magnets. Parameters of the PM-VFM are shown in the appendix.

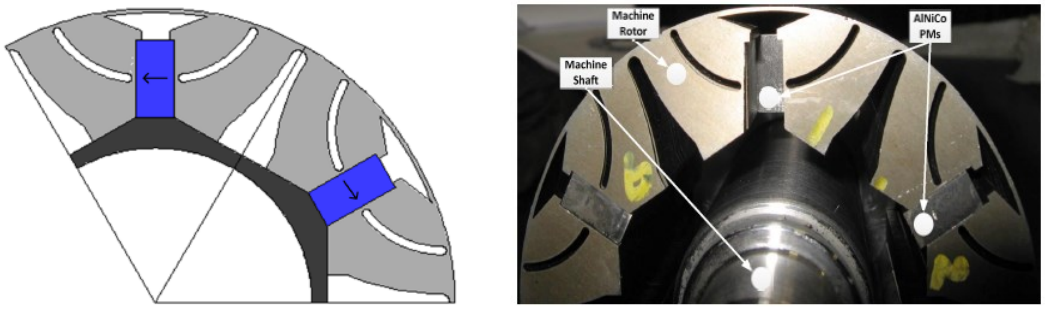

(a) (b)

Fig. 5. 3: (a) Rotor Geometry of Variable Flux Machine [77]. (b) Prototyped Rotor [77].

5.4 Vector Control of the VFM

Fig. 5.4 shows the schematic diagram for the controller used to control the VFM. It can be seen that there is two current loops (q-axis and d-axis current loops). Selection of i_q^* and i_d^* is done based on the knowledge that the q-axis current is responsible for producing the torque of the machine, while d-axis current is responsible for producing the flux. Therefore, $i^*_{q\text{-}min}$ should be able to deliver the required power to the load and $i^*_{q\text{-}max}$ should not exceed the machine rating. In addition, the i_d^* current pulse should be selected to keep the total d and q axes stator currents within the machine rating $i_q^2 + i_d^2 = i_{PMSG}^2$. A current limiter is also placed at the output of each current loop to keep the current within the machine ratings.

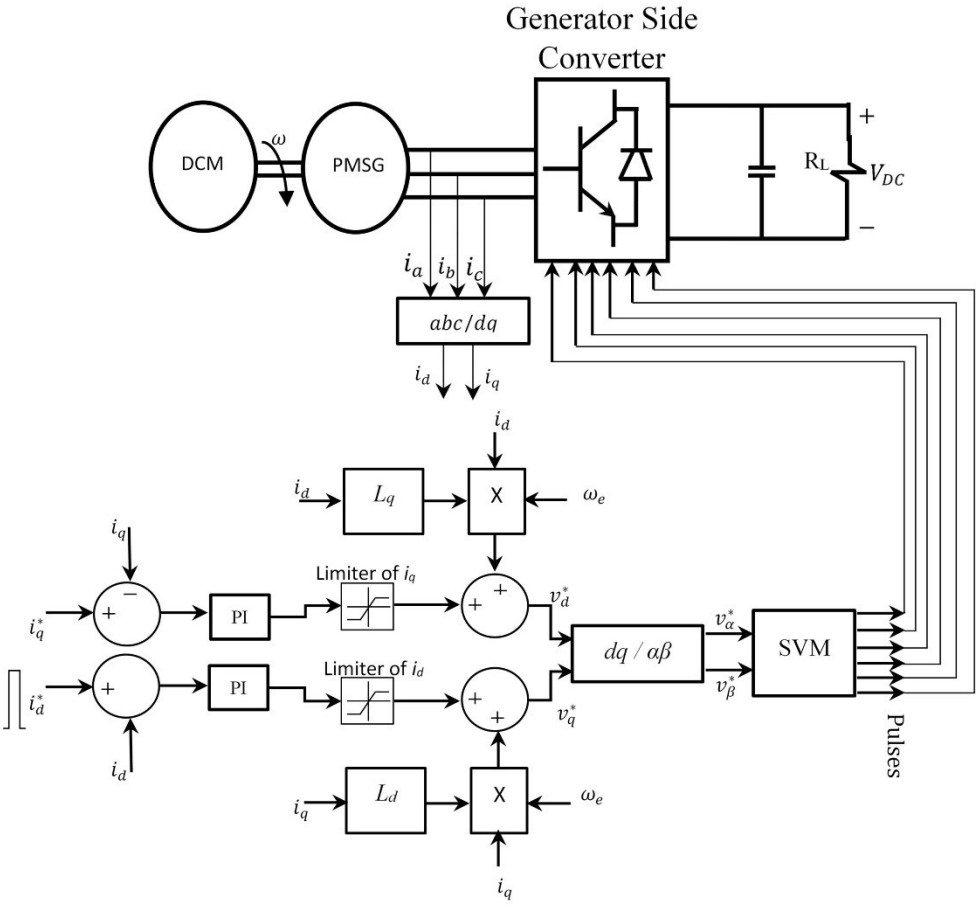

Fig. 5. 4: Controller of the Variable Flux Machine.

5.5 Experimental Setup

The flux controller of the VFM has been tested experimentally for voltage regulation purposes. The dc machine, which drives the VFM, was controlled using a buck converter. The torque of the dc machine was controlled by controlling its armature current using a PI controller. The control logic of the dc machine and the VFM were implemented and interfaced in real time using Opal-RT simulation. The simulation type for the controller in the Simulink file is set as a discrete-type with a sampling time of 50μsec. A SVM was used for the flux controller of the VFM to achieve fast response of the voltage loops. Fig. 5.5 shows a photo of the experimental setup of the VFM.

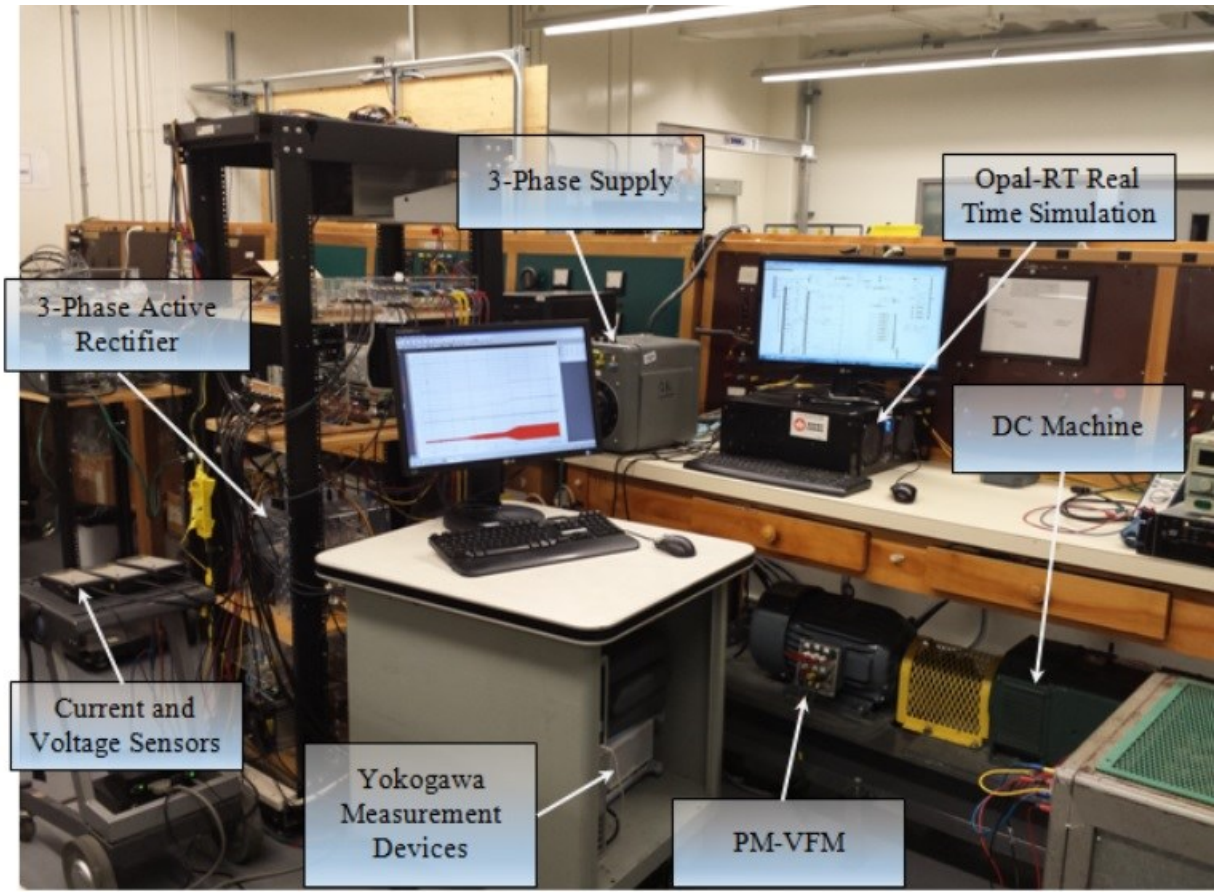

Fig. 5. 5: A Photo of the Experimental Setup of the VFM

5.6 Case Study and Results

In order to indicate the effectiveness of the flux control, for the VFM using the d-axis current pulses, in the voltage regulation purposes, two scenarios will be discussed as follows:

1. The injected i_d current pulse is zero, while the rotor speed is increased by a ramp function.
2. The injected i_d current pulse is negative, while the rotor speed is increased by a ramp function.

In both scenarios, the AlNiCO magnet of the VFM is initially fully magnetized at a flux linkage of 0.5 volt.sec. Fig. 5.6 shows the current limits for each magnetization state of the Alnico PM.

In the first scenario, the amplitude of the 1st harmonic of the terminal line voltage of the VFM increased when the rotor speed increased by a ramp function from (500-800) rpm as shown in Fig. 5.7 (B). In this scenario, no d-axis current pulse is injected to demagnetize the magnet.

In the second scenario, several cases of injecting d-axis current pulses have been studied to investigate its effect on the voltage regulation when the rotor speed increased by a ramp function from (500-800) rpm. These cases are shown in Figs. 5.8-5.10. D-axis current pulses (1% of the period) have been injected when the rotor speed is around 600 rpm. For the first case when the d-axis current pulse is -3A, it can be seen from Fig. 5.8 (B) that the increase of the 1st harmonic of the line voltage is reduced compared to the previous scenario when the d-axis current pulse is zero.

For the second case when the d-axis current pulse is -4A, the regulation of the 1st harmonic of the line voltage has been improved compared to the previous case when the d-axis current pulse is -3A as shown in Fig. 5.9 (B). However, the line voltage is still not completely regulated which can be observed from the third case when the d-axis current pulse is -5A as shown in Fig. 5.10 (B).

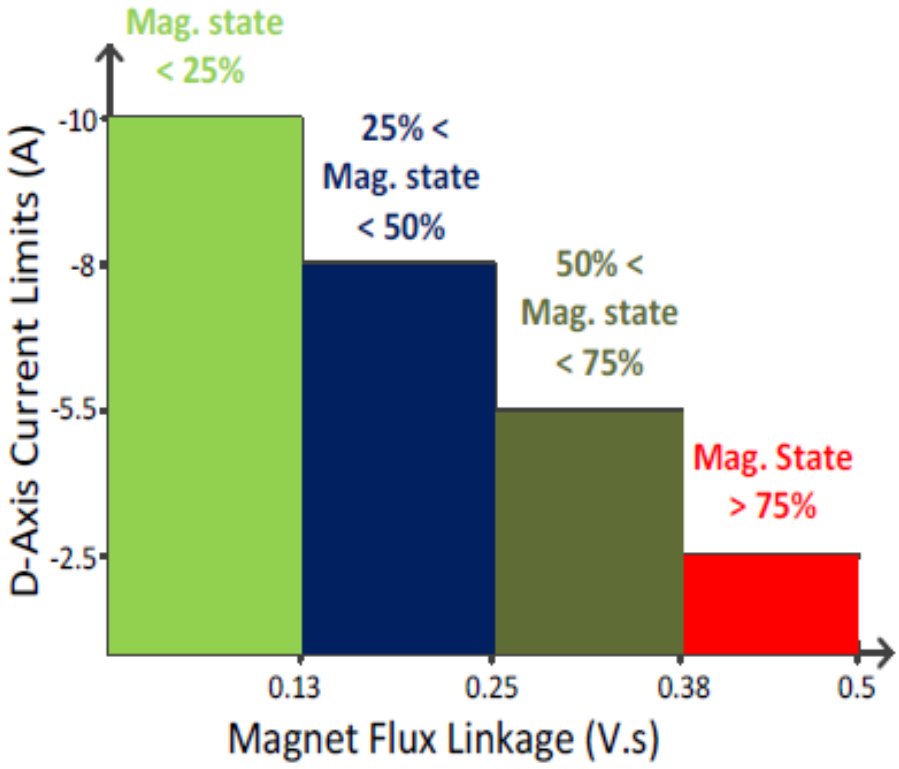

Fig. 5. 6: D-axis Current Limits Depending on the Magnetization States [77].

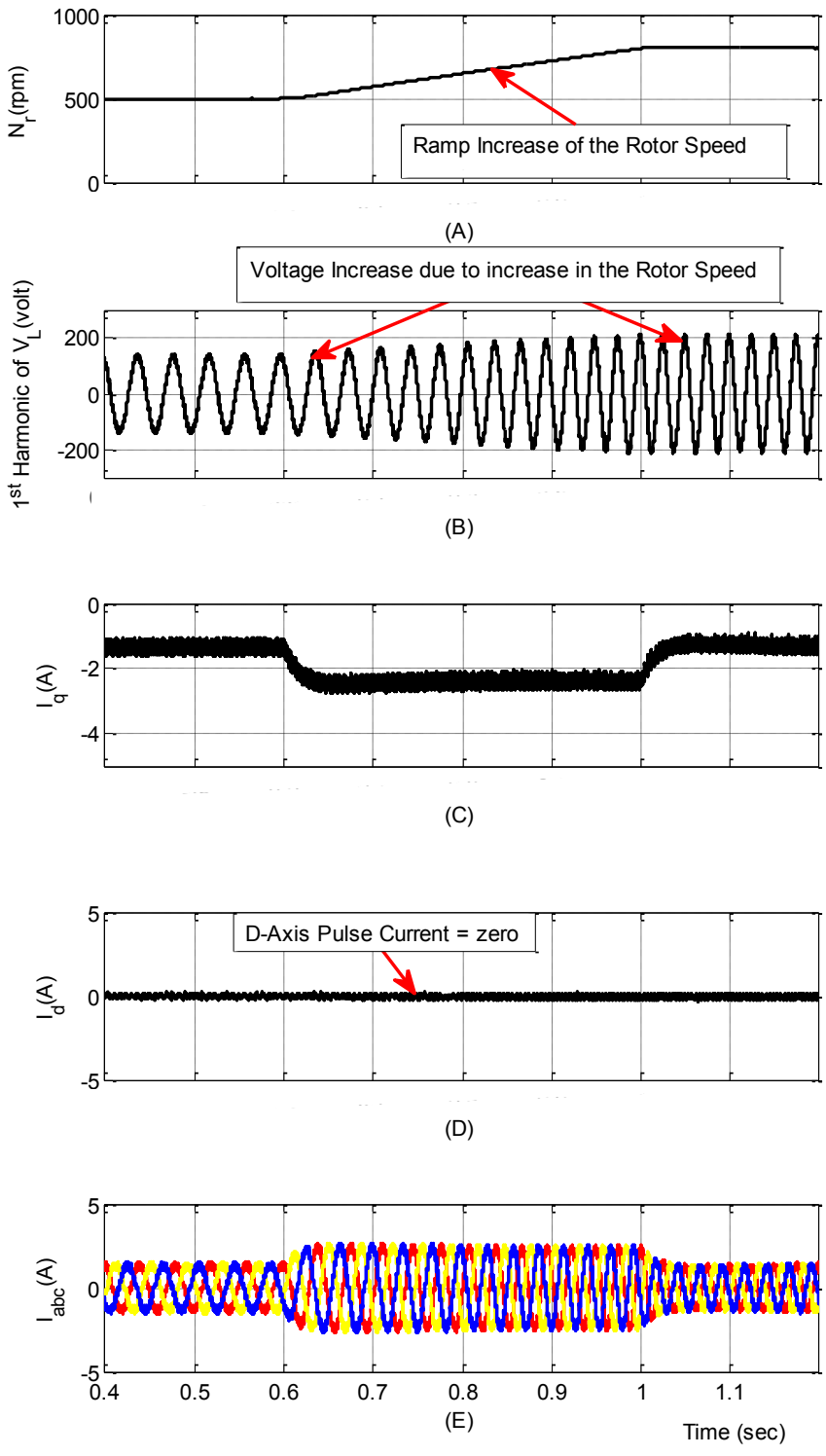

Fig. 5. 7: VFM Response to a Ramp Change in the Rotor Speed (500-800 rpm), without flux control (d-axis current pulse =0): (A) Rotor Speed. (B) 1st Harmonic of V_L. (C) q-Axis Current Component. (D) d-Axis Current Component. (E) 3-Ph Current.

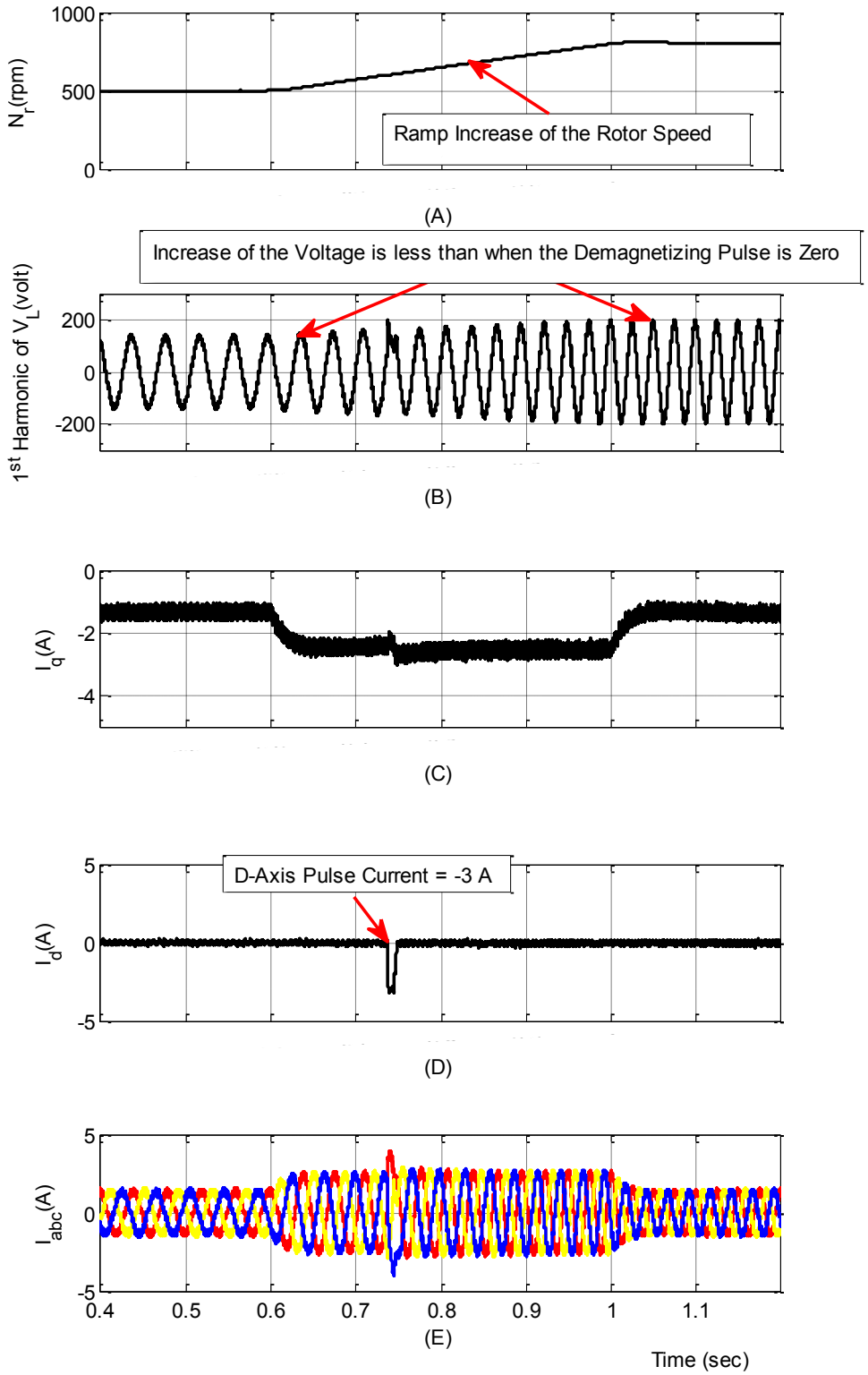

Fig. 5. 8: VFM Response to a Ramp Change in the Rotor Speed (500-800 rpm) when the d-Axis Current Pulse = -3 A: (A) Rotor Speed. (B) 1st Harmonic of V_L. (C) q-Axis Current Component. (D) d-Axis Current Component. (E) 3-Ph Current.

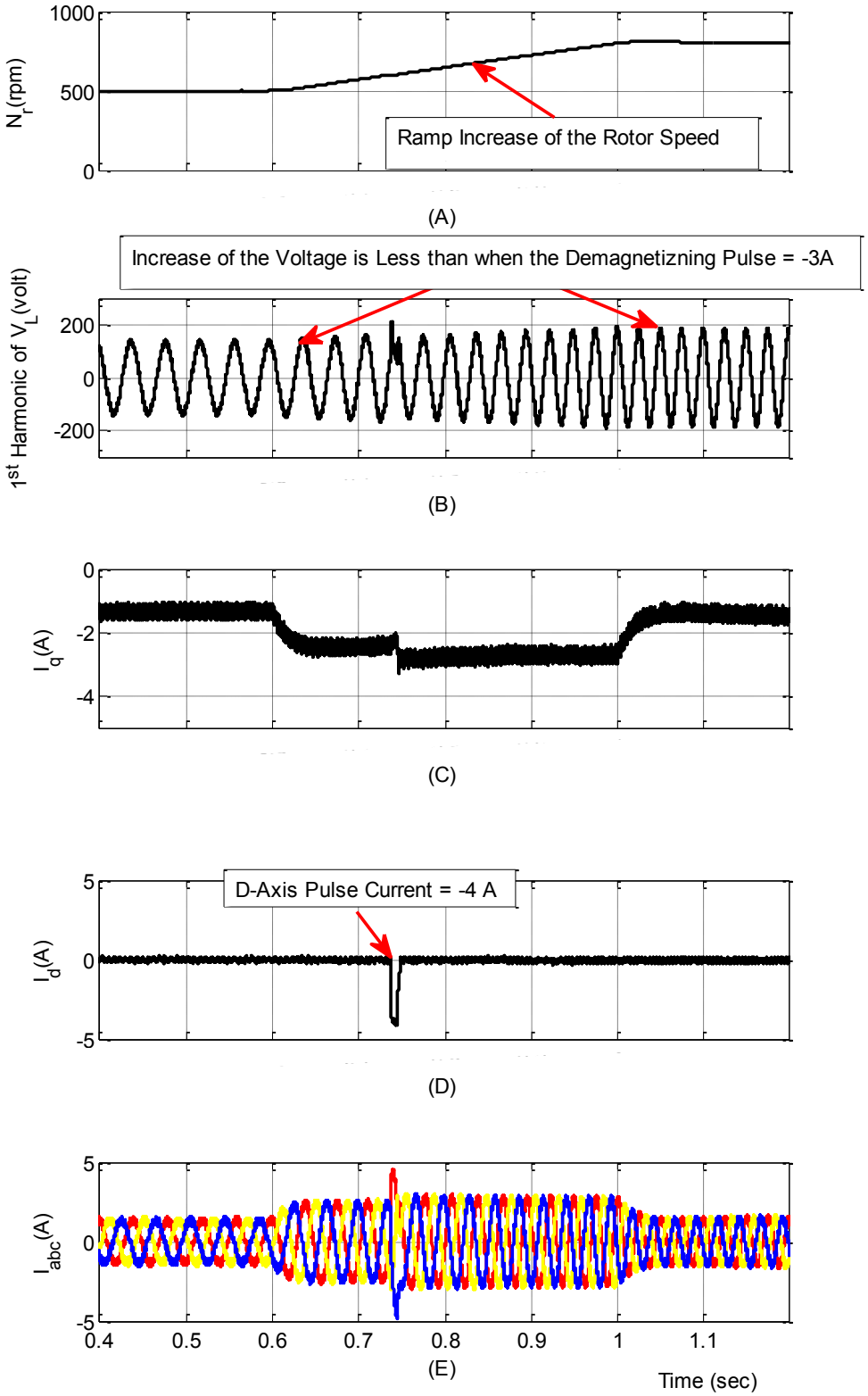

Fig. 5. 9: VFM Response to a Ramp Change in the Rotor Speed (500-800 rpm) when the d-Axis Current Pulse = -4 A: (A) Rotor Speed. (B) 1st Harmonic of V_L. (C) q-Axis Current Component. (D) d-Axis Current Component. (E) 3-Ph Current.

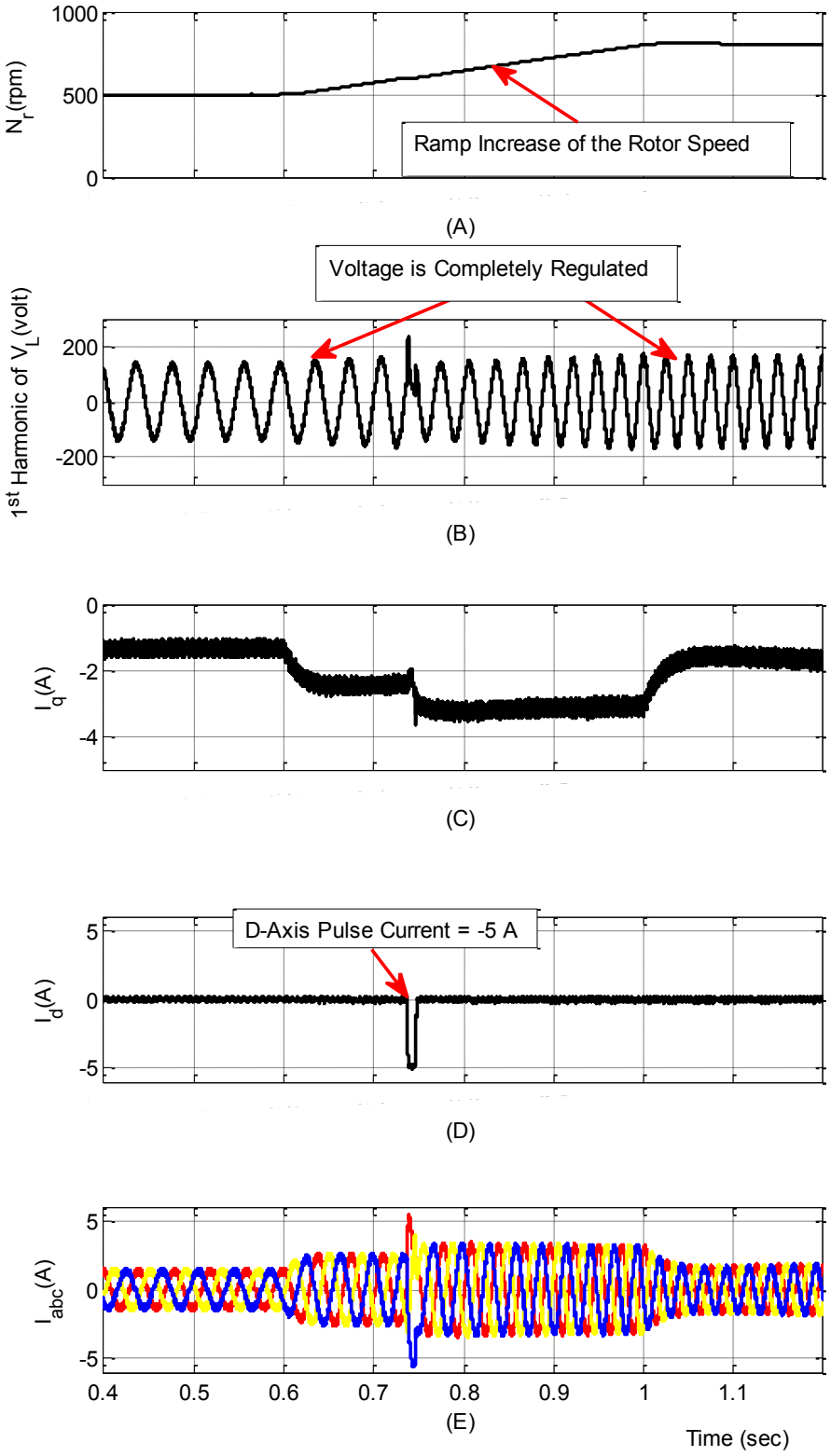

Fig. 5. 10: VFM Response to a Ramp Change in the Rotor Speed (500-800 rpm) when the d-Axis Current Pulse = -5 A: (A) Rotor Speed. (B) 1st Harmonic of V_L. (C) q-Axis Current Component. (D) d-Axis Current Component. (E) 3-Ph Current.

5.7 Conclusion

This chapter provides a demonstration for a proposed flux controller on the operation of the VFM, which uses the AlNiCo PM, for voltage regulation purposes. The AlNiCo magnet is considered a low coercive PM which can be magnetized or demagnetized using d-axis current pulses provided by flux controller.

Several values of d-axis current pulses have been injected for short duration to test the controller operation on the system under study and the behavior of the AlNiCo magnet before and after injecting d-axis current pulses while the rotor speed of the VFM increased by a ramp function. Without de-magnetizing the AlNiCo magnets of the VFM, the voltage of the machine cannot be regulated. However, by injecting different values of d-axis current pulses, the AlNiCo PM flux can be controlled and consequently the terminal voltage can be regulated, while these pulses have negligible losses compared to the q-axis current which improved the machine efficiency and performance.

CHAPTER 6: CONCLUSIONS, CONTRIBUTIONS AND RECOMMENDATIONS

6.1 Summary and Conclusions

Urban Wind Energy Modelling

- The prediction of the wind speed in the urban areas is difficult, due to the ground roughness and the frictional effects which reduce the wind speed close to the ground surface.
- The adjacent buildings significantly influence the wind regime around a specific building in the urban environment.
- Several techniques can be used for wind energy assessment in the urban environment which can be classified based on their accuracy as follows:
    - Field measurements, ideally at the position and the height of the proposed wind turbine.
    - Wind tunnel modeling with the aid of the meteorological or airport wind speed data.
    - Numerical methods including CFD analysis.
    - Wind atlases, which covers wide areas all over the world but it has a low resolution and accuracy.
- The wind atlases can only provide a general picture of the wind resource in certain areas. Moreover, it cannot take into account the local variations and their effect on the wind distribution.

- The wind speed at a specific position over the roof of the building can be estimated by using wind tunnel modeling and testing, which has to be combined with a meteorological or airport wind speed data at known locations. The wind tunnel tests are used to give a more accurate estimate of wind without actually undertaking a wind measurement campaign.
- A methodology for estimating the wind energy for all terrains in the urban environment using the wind tunnel testing is presented in this thesis.
- This methodology was tested using two case studies in Montreal with different terrains:
    - The first case was a homogeneous terrain (EV building case), the results show high correlation between the estimation of the wind energy using the proposed methodology and the field measurements calculated over the roof of the EV building.
    - The second case where the terrain is highly non-homogeneous (Equiterre building case), the discrepancy between the estimation using the wind tunnel testing and field measurement is higher.
- In general, the accuracy of this methodology depends on the complexity of the upstream terrain. Therefore, it can be used for estimating the wind energy especially for homogeneous upstream terrains.
- Such a method of estimating the wind speed in the urban environment is very useful for the early stages of the wind power development.

Voltage Regulation Using Flux Control of the PMG

- A new technique for controlling the flux of a PMG in a small wind turbine connected to a remote load was discussed in this thesis.
- The technique was based on injecting a negative or positive d-axis current to the stator coils of the PMG which controls the flux of the machine either by weakening or strengthening the flux to regulate the output voltage of PMG.
- This technique was used to control the flux of the PMG without any auxiliary coils or any special mechanical arrangements of the machine.
- The disadvantage of using this control strategy is that injecting a d-axis current in the stator coils leads to higher losses and a reduction of the machine efficiency.
- A case study was applied for small WECS and the results show how injecting several values of d-axis current can regulate the output voltage for variable speed operation.
- Flux weakening control for speed range extension purposes was also analyzed in the thesis.
- By applying a flux weakening d-axis current ($-i_d$), the PMG can provide lower V_{dc} for a given rotor speed. This means that the PMG system can provide a given V_{dc} at higher rotor speed. Thus, the flux weakening extends the operational speed of the PMG.
- It was verified through simulation analysis that flux weakening control is workable for the variable speed PMG system and significantly extends the operation speed range.

Reactive Power Compensation of the Flux Control of the PMG

- The flux control of the PMG has the capability to compensate the reactive power demanded by the 3-ph variable inductive load and it has been applied for this purpose in the thesis.
- The proposed WECS based active rectifier was used to inject several values of d-axis current components to control its flux. By injecting such current components, the reactive power consumed by the PMG was decreased gradually, then the PMG started generating reactive power to share the active rectifier in supplying the load. In this case, the load voltage was regulated for a variable inductive load.
- The flux controller shows high effective response during steady and transient states.
- Simulation results have been obtained for the proposed case study and experimental work was done to validate the simulation results.

Control of PM-VFM

- A flux controller for a PM-VFM for voltage regulation purposes has been developed.
- The PM-VFM uses AlNiCo magnet which is considered as a low coercive PM that can be magnetized or demagnetized using d-axis current pulses applied for a short period of time.
- The injected d-axis current pulses have negligible losses compared to the q-axis current which improve the machine efficiency.

6.2 Contributions

Urban Wind Energy Modelling

- A new method for estimating wind speed and energy over the roof of the buildings in the urban environments has been developed by means of wind tunnel experiments. The methodology was validated using two field case studies, one homogeneous the other non-homogeneous.

Voltage Regulation Using Flux Control of the PMG

- A new flux control technique for a PMG based WECS for voltage regulation purposes was developed for variable speed operation. This technique was based on injecting constant negative or positive d-axis current to the stator coils of the PMG to control the flux of the machine. Consequently, the output voltage will be regulated at variable speed operation.

Reactive Power Compensation of the Flux Control of the PMG

- The reactive power compensating capability of the flux controller was studied and investigated for the PMG for a variable inductive load. Using the flux controller, the reactive power consumed by the PMG is reduced and compensated gradually. At some point, the PMG starts generating reactive power instead of absorbing it. Such independent source of reactive power is necessary to compensate the reactive power especially in the emergency case when the electrical grid is completely shut down.

Control of PM-VFM

- Develop a new flux controller for a PM-VFM, which uses the AlNiCo PM, for voltage regulation purposes. The controller is implemented based on injecting d-

axis current pulses applied for short period of time, with negligible losses. This will reduce the losses of the machine and improve its efficiency.

6.3 Recommendations and Proposed Future Work

- Develop a new method to estimate the extracted wind energy by particular roof wind turbine in the building environments using the power-speed characteristics of the turbine with the aid of the wind tunnel tests.
- Develop a new controller for automatically control the flux of the PMG using the d-axis current of the machine at variable WECS conditions.
- Carry out additional research work on the reactive power flow of the system at the PCC when the dc link is connected to a grid side converter.
- Develop a new flux control based on a continuous estimation of the magnet flux for the AlNiCo PM.

References

[1] G. Van Bussel , "Electricity Generation with Small Wind Turbines", Springer Encyclopedia of Sustainability Science and Technology, pp. 3396-3413.

[2] R. Mittal, K. S. Sandhu and D. K. Jain, "An Overview of Some Important Issues Related to Wind Energy Conversion System (WECS)", In Proceedings of International Journal of Environmental Science and Development, Vol. 1, no. 4, pp. 351-363, October 2010.

[3] J. A. Baroudi, V. Dinavahi, A. M. Knight,"A Review of Power Converter Topologies for Wind Generators", IEEE International Conference on Electric Machines and Drives, pp. 458 – 465, May 2005.

[4] Kadam D.P1, Dr. Kushare B.E, "Overview of Different Wind Generator Systems and Their Comparison", International Journal of Engineering Science and Advanced Technology, Vol. 2, Issue 4, pp. 1076 – 1081, 2012. [Available Online]: http://www.ijesat.org 1076 [Access: 18 March 2016].

[5] H. S. Kim, D. D. C. Lu, "Review on Wind Turbine Generators and Power Electronic Converters with the Grid Connection", IEEE 20th Australasian Universities Power Engineering Conference (AUPEC), pp. 1-6, 2010.

[6] X. Bracke, J. De Kooning, J. Vyver and L. Vandevelde "Effective Capture of Wind Gusts in Small Wind Turbines by Using a Full Active Rectifier", Proceedings of the 3rd IEEE Conference on Renewable Power Generation (RPG 2014), Naples, pp. 1-6, Sept. 2014.

[7] D. Miao, and J. Shen, "Simulation and Analysis of a Variable Speed Permanent Magnet Synchronous Generator with Flux Weakening Control", Proceedings of IEEE International Conference on Renewable Energy Research and Applications (ICRERA), pp.1-6, Nagasaki, Nov. 2012.

[8] European Commission, 2007, "Urban Wind Resource Assessment in the UK", Report about the Wind Resource Assessment in the Urban Environment.

[9] L. Arriago, "Wind Energy in the Built Environment: A Design, Analysis Using CFD and Tunnel Modelling Approach". PhD Thesis Submitted to the University of Nottingham, 2009.

[10] https://en.wikipedia.org/wiki/Strata_SE1 (Access 21 March 2016).

[11] http://beforeitsnews.com/environment/2010/11/urban-rooftop-wind-turbines-254292.html (Access 21 March 2016).

[12] http://inhabitat.com/venger-wind-unveils-worlds-largest-rooftop-wind-farm-in-oklahoma-city/ (Access 21 March 2016).

[13] http://www.cundall.com/Cundall/fckeditor/editor/images/UserFilesUpload/file/WCIYB/IP-27%20-%20Wind%20turbine%20performance.pdf (Access 21 March 2016).

[14] J. Cheng, D. Lubitz and B. White, "Wind Tunnel Prediction of Wind Power Production in Complex Terrain", In Proceedings of 42nd Aerospace Sciences Meeting and Exhibit. Reno, Nevada, 2004.

[15] N. Vasan, T. Stathopoulos, "Wind Tunnel Assessment of the Wind Velocity Distribution on Vertical Façades", In Proceedings of Canadian Conference on Building Simulation, 2012.

[16] J. Villar, G. Simioni and J. Filho, "Procedures Laboratory for Small Wind Turbines Testing", In Proceedings of European Wind Energy Conference, 2010.

[17] Kalmikov, G. Dupont, K. Dykes, C. Chan, "Wind Power Resource Assessment in Complex Urban Environments: MIT Campus Case-Study Using CFD Analysis", In Proceedings of AWEA 2010 Wind Power Conference, May 2010.

[18] M. Popovac , "Analytical Method for Estimating Energy Output of Small Wind Turbines Integrated in Urban Areas", In Proceedings of 2nd European Energy Conference, 2012.

[19] Davenport, A. G., 1960. Rationale for determining design wind velocities. J. of Structural Engineering, ASCE, Vol. 86, pp. 39-68.

[20] T. Stathopoulos, "Introduction to Wind Engineering, Wind Structure, Wind-Building Interaction", Springer Wien New York, 2007.

[21] N. Vasan, T. Stathopoulos , "Experimental Study of Wind Effects of Unglazed Transpired Collectors," Solar Energy, Vol. 101, pp. 138-149, 2014.

[22] T. Stathopoulos, "Design and Fabrication of Wind Tunnel for Building Aerodynamics," Journal of Wind Engineering and Industrial Aerodynamics, Vol. 16, pp.361-376, 1984.

[23] A. Al-Quraan, P. Pillay, T. Stathopoulos, "Use of a Wind Tunnel for Urban Wind Power Estimation". In Proceedings of the IEEE Power and Energy Society General Meeting (PES), Washington, July, 2014.

[24] A. Al-Quraan, P. Pillay, T. Stathopoulos, "Estimation of Urban Wind Energy - Equiterre Building Case in Montreal", In Proceedings of the 14th Civil Engineering for Sustainability and Resilience (CESAR'14), Jordan, April 2014.

[25] http://www.windfinder.com/windstatistics/dorval_lake_saint_louis (Access 21 March 2016).

[26] http://www.bing.com/maps/ (Access 14 Feb. 2016).

[27] https://maps.google.ca (Access 21 March 2016).

[28] http://www.quartierdesspectacles.com/en/location/168/maison-du-developpement-durable/page-1 (Access 21 March 2016).

[29] http://www.climate.weatheroffice.gc.ca/prods_servs/glossary_e.html#elevation (Access 17 Sep. 2013).

[30] S. J. Huang and H. H. Wan, "Enhancement of Matching Turbine Generators with Wind Regime Using Capacity Factor Curves Strategy," IEEE Transaction on Energy Conversion, vol. 24, no. 2, pp. 551-553, Jun. 2009.

[31] S. H. Jangamshetti and V. G. Rau, "Normalized Power Curves as a Tool for Identification of Optimum Wind Turbine Generator Parameters," IEEE Transaction Energy Conversion, vol. 16, no. 3, pp. 283-288, Sep. 2001.

[32] A. Rotondo, A. Sayed, "Wind Tunnels: Practical Applications of Advanced Mathematics," Report about Wind Tunnels, July 2003.

[33] S. Mathew, K. P. Pandey and A. Kumar "Analysis of Wind Regimes for Energy Estimation", Elsevier Renewable Energy. 25(3), 381-399, Mar 2002.

[34] Renewable Energy Resources, Second edition, John Twidell and Tony Weir, Dec. 2005, London and New York.

[35] S. Mertens, "The Energy Yield of Roof Mounted Wind Turbines," Wind Engineering, vol. 27, no. 6, pp 507- 518, 2003.

[36] A.S. Bahaj, L. Myers and P.A.B James, "Urban Energy Generation: Influence of Micro-Wind Turbine Output on Electricity Consumption in Buildings," Energy and Buildings, Vol. 39, pp154-165, 2007.

[37] M. Heath, J.Walshe and S., "Estimating the Potential Yield of Small Building-Mounted Wind Turbines," Wind Energy, vol. 10, pp 271- 287, March 2007.

[38] K. Sunderland and M. Conlon, "Estimating the Yield of Micro Wind Turbines in an Urban Environment: A Methodology," Universities Power Engineering Conference (UPEC), pp 1- 6,Jan. 2010.

[39] N. Mithraratne, "Roof-Top Wind Turbines for Microgeneration in Urban houses in New Zealand," Energy and Buildings, Vol. 41, pp 1013-1018, 2009.

[40] GWEC, "Global Wind Report, Annual Market, Update 2013", Available online: http://www.gwec.net/wpcontent/uploads/2014/04/GWEC-Global-Wind-Report_9-April-2014.pdf (Access 7 Oct. 2015).

[41] X. Bracke, J. De Kooning, J. Vyver and L. Vandevelde "Effective Capture of Wind Gusts in Small Wind Turbines by Using a Full Active Rectifier", Proceedings of the 3rd IEEE Conference on Renewable Power Generation (RPG 2014), Naples, pp. 1-6, Sept. 2014.

[42] Y. Inoue, S. Morimoto, and M. Sanada, "Control Method for Direct Torque Controlled PMSG in Wind Power Generation System", Proceedings of IEEE International Conference on Electric Machines and Drives (IEMDC'2009), Miami, USA, pp. 1231-1238, May. 2009.

[43] M. Kesraoui, B. Bendaoui and A. Chaib, "Using a DFIG Based WECS for Voltage Regulation at PCC", Proceedings of 6th International IEEE Renewable Energy Congress (IREC), 2015.

[44] M. Singh; V. Khadkikar; A. Chandra, " Grid Synchronization with Harmonics and Reactive Power Compensation Capability of a Permanent Magnet Synchronous Generator-Based Variable Speed Wind Energy Conversion System", IET Power Electronics, Vol. 4, no. 1, pp. 122-130, 2011.

[45] J. Chen; C. Gong; X. Deng, "Energy Management and Power Control for a Stand-Alone Wind Energy Conversion System", Proceedings of 38th Annual Conference on IEEE Industrial Electronics Society (IECON), 2012.

[46] F. Louar; A. Ouari; A. Omeiri; F. Senani; A. Rahab, “Direct power control (DPC) of PMSG based wind energy conversion system”, Proceedings of the 4th International Conference on Electrical Engineering (ICEE), 2015.

[47] A. Rajaei; M. Mohamadian; A. Varjani, “Vienna-Rectifier-Based Direct Torque Control of PMSG for Wind Energy Application”, IEEE Transactions on Industrial Electronics, Vol. 60, no. 7, pp 2919-2929.

[48] F. Capponi, R. Terrigi, F. Caricchi, and L. Del Ferraro, “Active Output Voltage Regulation for an Ironless Axial-Flux PM Automotive Alternator with Electromechanical Flux Weakening”, IEEE Transactions on Industry Applications, Vol. 45, No. 5, pp. 1785-1793, Sept. 2009.

[49] S. Javadi, and M. Mirsalim, “A Coreless Axial Flux Permanent Magnet Generator for Automotive Applications”, IEEE Transactions on Magnetics, Vol. 44, No. 12, pp. 4591-4598, Dec. 2008.

[50] K. Chau, Y. Li, J. Jiang, and S. Niu, “Design and Control of a PM Brushless Hybrid Generator for Wind Power Application”, IEEE Transactions on Magnetics, Vol. 42, No. 10, pp. 3497-3499, Oct. 2006.

[51] S. Morimoto, Y. Takeda, T. Hirasa, and K. Taniguchi, “Expansion of Operating Limits for Permanent Magnet Motor by Current Vector Control Considering Inverter Capacity”, IEEE Transactions on Industry Applications, Vol. 26, No. 5, pp. 866-871, Sept. 1990.

[52] S. Subhoff, K. Corzine, and H. Hegner, “A Flux Weakening Strategy for Current-Regulated Surface-Mounted Permanent-Magnet Machine Drives”, IEEE Transactions on Energy Conversion, Vol. 10, No. 3, pp. 431-437, Sept. 1995.

[53] Z. Lubosny , “Wind Turbine Operation in Electric Power Systems”, Publisher: Springer , 2003.

[54] P. Pillay, R. Krishnan, “Modeling of Permanent Magnet Motor Drives”, IEEE Transaction in Industrial Electronics, Vol. 35, No. 4, 1988.

[55] D. Mehrzad, J. Luque, M. Cuenca “Vector Control of PMSG for Wind Turbine Applications”, Project Submitted to Alborg University (Institute of Energy Technology), 2008.

[56] D. Miao; J. Shen, "Simulation and Analysis of a Variable Speed Permanent Magnet Synchronous Generator with Flux Weakening Control", In Proceedings of IEEE International Conference on Renewable Energy Research and Applications (ICRERA), 2012.

[57] R. Nagaraj, "Renewable Energy Based Small Hybrid Power System for Desalination Applications in Remote Locations", Proceedings of IEEE 5th India International Conference on Power Electronics (IICPE), pp. 1-5, Dec. 2012.

[58] B. Singh, V Sheeja, R. Uma, P. Jayaprakash, "Voltage- Frequency Controller for Stand Alone WECS Employing Permanent Magnet Synchronous Generator", Proceedings of IEEE Third International Conference on Power Systems, pp. 1-6, December 2009.

[59] R. Teodorescu, M. Lissere, and P. Rodriguez, "Grid Converter for Photovoltaic and Wind Power Systems", New York: Wiley, 2011.

[60] E. Monmasson, L. Idkhajine, M. Cirstea, I. Bahri, A. Tisan, and M. Naouar, "FPGAs in industrial control applications" *IEEE Transaction Industrial Informatics*, Vol. 7, No. 2, pp. 224–243, 2011.

[61] L. S Yang and T. J. Liang, "Analysis and implementation of a novel bidirectional DC–DC converter," *IEEE Transaction in Industrial Electronics*, Vol. 59, No. 1, pp. 422–434, 2012.

[62] L. Barote, C. Marinescu and M. Cirstea, "Control Structure for Single-Phase Stand-Alone Wind-Based Energy Sources", *IEEE Trans. on Industrial Electronics*, Vol. 60, No. 2, pp. 764-772, 2013.

[63] M. Singh, V. Khadkikar, A. Chandra, "Grid Synchronization with Harmonics and Reactive Power Compensation Capability of a Permanent Magnet Synchronous Generator-Based Variable Speed Wind Energy Conversion System", IET Power Electronics, vol. 4, no. 1, pp. 122-130, 2011.

[64] T. Senjyu, T. Kinjo, H. Fujita, "Analysis of Terminal Voltage and Output Power Control of Wind Turbine Generator by Series and Parallel Compensation Using SMES'. In Proceedings of IEEE 35th Annual Power Electronics Specialists Conference, vol. 6, pp. 4278–4284, June 2004.

[65] N. Holtsmark, M. Molinas, "Reactive Power Compensation Using an Indirectly Space Vector-Modulated Matrix Converter", In Proceedings of IEEE International Symposium on Industrial Electronics, pp. 2455 – 2460, July 2010.

[66] Y. Lang, B. Wu and N. Zargari, "A Novel Reactive Power Control Scheme for CSC Based PMSG Wind Energy System", In Proceedings of IEEE Industry Applications Society Annual Meeting, pp. 1-8, Oct. 2008.

[67] N. Rajan, R.Subramanian, L. Priya , "PMSG Based Stand Alone Wind Power System with Sensorless MPPT", International Journal of Innovative Research in Science, Engineering and Technology, Vol. 3, Special Issue 1, pp. 1144-1150, February 2014.

[68] Z. Zhang, Y. Zhao, J. Zeng, W. Qiao, "A Flux Vector-Based Discrete-Time Direct Torque Control for Salient-Pole Permanent-Magnet Synchronous Generators", Proceedings of IEEE Energy Conversion Congress and Exposition (ECCE), pp. 1515-1521, Sept. 2014.

[69] Y. Errami, M. Hilal, M. Benchagra, M. Maaroufi, M. Ouassaid, "Nonlinear control of MPPT and grid connected for wind power generation systems based on the PMSG", IEEE International Conference on Multimedia Computing and Systems (ICMCS), pp. 1055-1060, May 2012.

[70] Y. Errami, M. Maaroufi, M. Ouassaid, "Modelling and control strategy of PMSG based variable speed wind energy conversion system", IEEE International Conference on Multimedia Computing and Systems (ICMCS), pp. 1-6, April 2011.

[71] E. Sulaiman, T. Kosaka, N. Matsui and M. Z. Ahmad,"Design Improvement and Performance Analysis of 12 Slot-10 Pole Permanent Magnet Flux Switching Machine with Field Excitation Coils", In Proceedings of the IEEE 5th International Power Engineering and Optimization Conference (PEOCO2011), Shah Alam, Selangor, Malaysia, June 2011.

[72] E. Sulaiman, T. Kosaka, and N. Matsui, "Design Optimization of 12 Slot–10 Pole Hybrid Excitation Flux Switching Synchronous Machine with 0.4kg Permanent Magnet for Hybrid Electric Vehicles", In Proceedings of the IEEE 8th International Conference on Power Electronics, Shilla Jeju, Korea, 2011.

[73] M. Ahmad; E. Sulaiman; T. Kosaka, "Optimization of Outer-Rotor Hybrid Excitation FSM for in-Wheel Direct Drive Electric Vehicle", In Proceedings of the IEEE International Conference on Mechatronics, pp. 691-696, 2015.

[74] H. Ali, E. bin Sulaiman, M. Jenal, M. Omar, "Three Phase Segmental Rotor Hybrid Excitation Flux Switching Motors for Various Applications", In Proceedings of the IEEE Student Conference on Research and Development (SCOReD), pp. 373-377, 2015.

[75] N. Limsuwan, T. Kato, K. Akatsu, and R. Lorenz, "Design and evaluation of a variable-flux flux-intensifying interior permanent-magnet machine," IEEE Transactions on Industry Applications, Vol. 50, no. 2, pp. 1015–1024, March 2014.

[76] M. Ibrahim, L. Masisi and P. Pillay, “Design of Variable-Flux Permanent-Magnet Machines Using Alnico Magnets”, IEEE Transactions on Industry Applications, Vol. 51, no. 6, pp. 4482-4491, 2015.

[77] L. Masisi, “Design and Development of Novel Electric Drives for Synchronous Reluctance and PM Synchronous Machines”, A Thesis submitted to Concordia University, 2015.

Appendix

Values of PM-VFM Parameters

VFM Parameters	**Values**
Number of Poles	6 poles
Armature Resistance (r_a)	1.3 ohm
d-Axis Inductance (L_d)	0.0575 H
q-Axis Inductance (L_q)	0.036 H
Moment of Inertia (J)	0.03 kg.m^2
Friction Coefficient (B)	5e-6
Iron Loss	410 watt
Full Magnetization Flux Linkage	0.52 volt.sec